MODELING OF CATALYTIC PLATE REACTORS FOR FUEL PROCESSOR SYSTEMS

by

Rafet Murat Kırçın

B.S., Chemical Engineering, Boğaziçi University, 2005

Submitted to the Institute for Graduate Studies in
Science and Engineering in partial fulfillment of
the requirements for the degree of
Master of Science

Graduate Program in Chemical Engineering

Boğaziçi University

2009

to my family

ACKNOWLEDGEMENTS

I would like to express my sincere gratitude to my supervisor Professor Zeynep İlsen Önsan. Over the long course of two years of this project, her patience and understanding, but most of all, her faith and trust in me always surprised me. Yet here I am, just as she said I would be. It is difficult to find the proper words to describe how arduous it has been to complete this task. I believe she is one of the very few who would not need to hear any.

I would also like to thank cordially my co-advisor Professor Ahmet Erhan Aksoylu and Assistant Professor Ahmet Kerim Avcı. Their professional help and expertise added greatly to the improvement of anything I grappled with. Especially Ahmet Kerim Avcı has devoted his time and contributed to my work a lot, I am happy to get to know him better.

I owe thanks to many people from work; MKEK Kırıkkale Mühimmat Fabrikası, Ar-Ge. Mehmet Şeref Tanıt and İdris Aydoğdu have done what they would for their own son. I can sincerely say that each has become more of a friend and a mentor than a supervisor. My friends there helped me with hardware and CAD; some sought academic advice, some made useful intuitions and many shared my work load. I thank Ahmet N. Demir, Serkan Kızıl, Abdullah Şener, Onur Güngör, Dilek Durak and Turgut Ecevit.

I am greatly indebted to a colleague of mine, whom I have come to know better in the past few months. He never even hesitated to help when I was in need. In fact, if it weren't for his help, none of this could have been made. He is one of the kindest spirits I've met, Mustafa Karakaya, and I consider myself to be lucky to have met and worked with him.

My family has been a continuous support throughout my graduate study. I believe that I could not have made it this far without their ever ending prayers.

Financial support provided by TÜBİTAK-104M163, DPT-07K120630 and BAP-06A503 and 08A503 are greatly appreciated.

ABSTRACT

MODELING OF CATALYTIC PLATE REACTORS FOR FUEL PROCESSOR SYSTEMS

The mathematical model of a catalytic plate reactor (CPR) in which hydrogen is produced by two different reaction pairs, namely, exothermic methane total oxidation coupled with either ethanol steam reforming or ethane dehydrogenation (both of which are endothermic) is constructed and the steady state and dynamic behaviors are investigated. A two-dimensional heterogeneous model including conservation of momentum, mass and energy is used to describe reactor performance in steady-state operation as a function of various operational and dimensional parameters such as feed composition on different sides of the plate including water/hydrocarbon and oxygen/hydrocarbon ratios, plate material and wall thickness. Simulations using stoichiometric ratios of reactants and standard materials of construction result in small transverse and axial temperature gradients and realistic reactor performance in terms of reactant conversions for both reaction pairs. Parametric investigations conducted by variation of plate material and wall thickness lead to minor changes only in thermal patterns and indicate no significant effects on reactor performance. On the other hand, variations in operational parameters such as the water/hydrocarbon and oxygen/hydrocarbon ratios result in notable changes in the reactor output. In ethanol steam reforming, water-deficient feed in the reforming channel reduces ethanol conversion and hydrogen production dramatically. In both ethanol reforming and ethane dehydrogenation cases, reduction in the oxygen content of the oxidation channel causes the methane conversion values to be significantly lower, leading to lower heat production/consumption rates. The start-up behavior of the reactor is also analyzed via dynamic simulations, which show that in both reaction pairs, the temporal and spatial evolutions of transients converge to the steady state solution.

ÖZET

YAKIT İŞLEMCİ SİSTEMLERİ İÇİN KATALİTİK PLAKA REAKTÖRLERİ MODELLEMESİ

Ekzotermik metan toplam oksidasyonu ile eşlenmiş etanol buharlı reformlaması, veya etan dehidrojenasyonu, olmak üzere iki farklı reaksiyon çifti ile hidrojen üretebilen bir katalitik plaka reaktörünün matematiksel modeli oluşturularak, reaktörün yatışkın durum ve dinamik davranışı incelenmiştir. Momentum, kütle ve enerji denkliklerini içeren iki boyutlu heterojen bir model çerçevesinde, reaktörün yatışkın durumdaki performansı su/hidrokarbon ve oksijen/hidrokarbon oranları dahil olmak üzere plakanın iki yüzeyindeki besleme bileşimleri, plaka malzemesi ve plaka duvar kalınlığı gibi çeşitli operasyonel ve boyutsal parametrelerin fonksiyonu olarak incelenmiştir. Beslemesinde stokiyometrik girdi oranları ve yapısında standart malzemeler kullanılan modellerin benzetimleri girdi dönüşümleri açısından bakıldığında gerçeğe uygun sonuçlar vermekte ve hem enine hem de boyuna olmak üzere reaktör boyunca küçük sıcaklık farkları göstermektedir. Plakanın yapısal ve boyutsal özelliklerinin değiştirilmesi ile yürütülen parametrik incelemeler sonucunda bu türden değişikliklerin reaktör performansı üzerinde önemli bir etkisi olmadığı gözlenmiştir. Su/hidrokarbon veya oksijen/hidrokarbon oranları gibi operasyon parametrelerinin değiştirilmesi ise reaktör çıktısında kayda değer değişimlere neden olmaktadır. Etanol buharlı reformlamasında, reformlama kanalına yeterli su içermeyen girdi karışımı beslenmesi etanol dönüşmesini ve hidrojen üretimini önemli ölçüde azaltmaktadır. Etanol reformlama ve etan dehidrojenasyonu işlemlerinin her ikisinde de oksidasyon kanalının oksijen içeriğindeki bir azalma metanın dönüşmesini önemli ölçüde azaltmakta ve sistemin ısı üretim/tüketim hızını düşürmektedir. Reaktörün çalışmaya başlamasından itibaren yatışkın duruma kadar oluşan geçici/yatışkın olmayan durumu da dinamik benzetimler ile ayrıca incelenmiştir. Bu benzetimler her iki reaksiyon çiftinde de belirli zaman aralıklarında alınan çözümlerin hem zamansal hem de uzaysal olarak gittikçe yatışkın durum çözümüne yakınsadığını göstermiştir.

TABLE OF CONTENTS

LIST OF FIGURES

LIST OF TABLES

LIST OF SYMBOLS/ABBREVIATIONS

A	Cross–sectional area of reactor	m^2
A_k	Arrhenius constant for reaction k	Pa^{-1}
c^0_{ij}	Inlet concentration of species i in channel j	mol m^{-3}
c_{ij}	Concentration of species i in channel j	mol m^{-3}
C_{pi}	Heat capacity of species i	J mol^{-1} K^{-1}
D	Diffusivity	m^2 s^{-1}
D_{eff}	Effective diffusivity	m^2 s^{-1}
E_k	Activation energy of reaction k	kJ $kmol^{-1}$
F^n_{0ij}	Initial molar flowrate of species i in channel j	mol s^{-1}
F^n_{ij}	Molar flowrate of species i in channel j	mol s^{-1}
F^v_{ij}	Volumetric flowrate of species i in channel j	m^3 s^{-1}
H	Reactor height	mm
i	Species index	–
j	Channel index	–
k	Thermal conductivity	W $m^{-1}K^{-1}$
k_{eff}	Effective thermal conductivity in catalyst layer	W $m^{-1}K^{-1}$
k_k	Rate coefficient for reaction k	mol $kgcat^{-1}$ h^{-1}
K_k	Equilibrium constant for reaction k	Pa^{-1}
K_P	Equilibrium constant	Pa
k_s	Thermal conductiviy of wall	W $m^{-1}K^{-1}$
L	Reactor length	m
n	Normal vector	–
P	Pressure	Pa
Q	Heat generation/consumption rate	W m^{-3}
R_g	Universal gas constant	m^3Pa $K^{-1}mol^{-1}$
R_{ij}	Reaction rate of species i in channel j	kmol $m^{-3}s^{-1}$
r_k	Rate of reaction k	kmol $m^{-3}s^{-1}$
S	Entropy	J K^{-1}
T	Temperature	K

T^0_j	Inlet gas temperature in channel j	K
w	Reactor width	m
x	Axial coordinate	m
X_{eq}	Equilibrium conversion	–
X_{ij}	Conversion of species i in channel j	–
z	Transverse coordinate	mm
α_j	Constant in the heat capacity equation	J mol^{-1} K^{-1}
β_j	Constant in the heat capacity equation	J mol^{-1} K^{-2}
γ_j	Constant in the heat capacity equation	J mol^{-1} K^{-3}
δ_c	Catalyst layer thickness	mm
δ_j	Constant in the heat capacity equation	J mol^{-1} K^{-4}
δ_s	Plate thickness	mm
ε_p	Catalyst bed porosity	–
κ	Catalyst bed permeability	m^2
κ_i	Adsorption constant for species i	Pa^{-1}
μ or η	Viscosity	Pa.s
ρ	Density	kg m^{-3}
υ^0_j	Inlet gas velocity in channel j	m s^{-1}
υ_j	Gas velocity in channel j	m s^{-1}
υ_x	Velocity in x direction	m s^{-1}
υ_z	Velocity in z direction	m s^{-1}
$\Delta H^0_{f,298}$	Standard heat of formation	kJ mol^{-1}
ΔH^0_{298}	Standard heat of reaction	kJ mol^{-1}
ΔH_R	Heat of reaction R	kJ mol^{-1}
$\Delta T_{adiabatic}$	Adiabatic temperature drop	K
CPR	Catalytic plate reactor	
DEHYD	Dehyrogenation	
FEM	Finite element method	
HEX	Heat exchanger	

IPOX	Indirect partial oxidation
LHHW	Langmuir-Hinshelwood-Hougen-Watson
LPG	Liquefied petroleum gas
OSR	Oxidative steam reforming
PDE	Partial differential equation
PEM	Proton exchange membrane fuel cell
SR	Steam reforming
TOX	Total oxidation
WGS	Water–gas shift

1. INTRODUCTİON

Fuel cell technology is an innovative method designed for meeting the strict requirements of recent legislation on air pollution control regarding CO and NO_x emissions. The proton exchange or polymer electrolyte membrane (PEM) fuel cell fueled by H_2 has future for small-scale stationary applications in the short run and for mobile applications in the long run (Barbir, 2005; O'Hayre *et al*., 2005). At present, the infrastructure for the distribution and/or storage of H_2 is not adequate**;** hence, *in situ* H_2 production by processing of fossil fuels with a distribution network (methane, LPG and gasoline) or of renewable resources (ethanol) is a realistic alternative. PEM fuel cells use a pure supply of H_2 which necessitates highly selective catalytic fuel processing involving various combinations of steam reforming, water-gas shift and total or selective oxidation reactions (Trimm and Önsan, 2001; Önsan, 2007).

The total catalyst loading required by auto-thermal reforming, low temperature water-gas shift and selective CO oxidation units of a methane processor feeding a 1.5 kW PEM fuel cell is roughly 1.5 kg (Tan *et al*., 2008), and an integrated gasoline processor with a design scale of 1 kW entails a volume of 1.2 L corresponding to about 1 kg of catalysts (Qi *et al*., 2006). The catalyst amounts and reactor volumes influence the technical feasibility of fuel processors, because the power quoted for small-scale stationary units or for automotive applications like passenger cars is around 50 kW (Zalc and Löffler, 2002). The need for careful temperature control and energy integration as well as the cost of valuable metal catalysts and elimination of pore diffusion effects has compelled research toward process intensification, i.e. reduction of unit sizes, through design of structured reactors and use of alternative catalysts (Qi *et al.,* 2007).

The catalytic plate reactor (CPR) constitutes an example of structured reactors whereby conventional packed-bed reactors are sized down due to intensification of heat and mass transfer (Zanfir and Gavriilidis, 2001). The CPR itself is a cascade of closely spaced plates coated with catalyst on both faces. If the catalyst coating on each face of the plate is different, it is possible to achieve significant heat transfer intensification by running an endothermic reaction such as steam reforming on one surface and an

exothermic reaction such as total oxidation on the other surface of the plate for supplying the energy required by the endothermic reaction (Zanfir and Gavriilidis, 2003; Ramaswamy *et al.,* 2006).

The aim of the present thesis is the mathematical modeling and steady-state and dynamic simulation of a catalytic plate reactor (CPR) in which hydrogen is produced by two different reaction pairs, namely, exothermic methane total oxidation coupled with either ethanol steam reforming or ethane dehydrogenation both of which are endothermic. A two-dimensional heterogeneous model including conservation of momentum, mass and energy is used to describe reactor performance as a function of various operational and dimensional parameters such as feed composition on different sides of the plate including steam/hydrocarbon and oxygen/hydrocarbon ratios, plate material and wall thickness.

Chapter 2 contains a brief survey of the literature on catalytic plate reactors and on H_2 production from hydrocarbons by ethanol steam reforming and ethane dehydrogenation. Mathematical model of the catalytic plate reactor (CPR) is presented in Chapter 3 along with rate expressions taken from the literature for methane total oxidation, ethanol steam reforming and ethane dehydrogenation. The steady-state and dynamic simulation results for ethanol steam reforming combined with methane total oxidation are presented and discussed in Chapter 4, while the steady-state and dynamic simulation results for ethane dehydrogenation coupled with methane total oxidation are presented and discussed in Chapter 5. Finally, the conclusions that can be drawn from this computational study and the recommendations for future work are summarized in Chapter 6.

2. LITERATURE SURVEY

2.1. Catalytic Plate Reactors

Process intensification is an engineering design approach which can reduce the size of process equipments dramatically; i.e. replace large, expensive, energy intensive equipment or processes with ones that are smaller, less costly and more efficient; or it can combine multiple operations into fewer devices, even into a single apparatus (Tsouris and Porcelli, 2003) and therefore miniaturize process plants, leading to improvement of processes with respect to energy demands and plant size. It provides important savings in capital cost by intensifying reactor equipment and reduces operating costs by improving the system thermal recovery (Lee *et al*., 2007). Also among its advantages are the improvements in inherent and added-on safety of equipments, processes and facilities along with reductions in environmental impact (Zanfir and Gavriilidis, 2001). Some applications of process intensification are shown in Figure 2.1.

The first case of process intensification was the introduction of HiGee technology. A conventional contacting column has limited output due to the slow descent of the liquid phase down the column, which is caused by the gravitational force only. In order to overcome this limitation, HiGee technology utilizes a rotating packed bed (Figure 2.1(d)), which can induce centrifugal forces much greater than gravitational force. The increased driving force allows for increased throughput in the unit and greatly improves mass transfer efficiency. Thus, employing rotating equipments becomes preferential over installing large separation systems. This system was developed by ICI™ back in the 1970s; however, the first commercial application took place in 1997, where 30 m high vacuum towers in an oil plant were replaced with 1.5 m diameter centrifugal strippers (Tsouris and Porcelli, 2003).

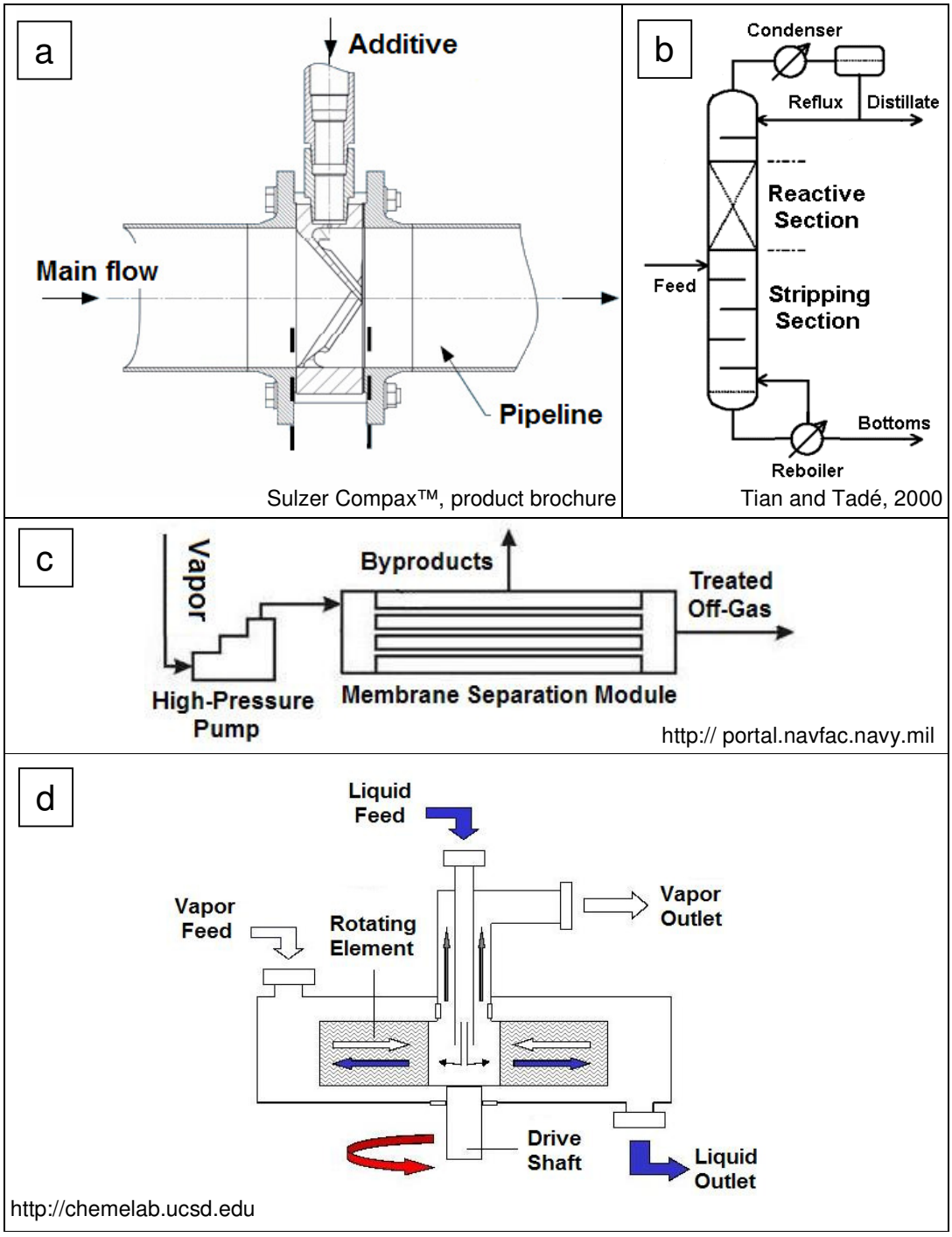

Figure 2.1. Some applications of process intensification; (a) static mixer, (b) reactive distillation, (c) pervaporation and (d) centrifugal contactor ((a) Sulzer Chemtech, 2009; (b) Tian and Tadè, 2000; (c) NAVFAC; (d) Barber *et al.*, 2009)

Similar to the spinning strippers, reactive distillations with liquid phase catalysts (Siirola, 1996), static mixers (Sutherland, 1874; Thakur, 2003; Paglianti, 2008), in-line monolithic reactors, HEX (compact heat exchanger/reactor) systems are all examples of intensification applications of processes, unit operations and process equipments (Tsouris and Porcelli, 2003). Although only some are commercialized, these implementations are early examples of process intensification, even earlier than the process intensification (or dynamic enhancement) concept itself (Thakur, 2003).

Among current popular research topics on process intensification, microreactors, microscale pervaporation (separation by partial vaporization via membranes, (Figure 2.1(c)), distillation, reactive distillation, reactive evaporation, spinning disk reactors, and various types of plate reactors (Tsouris and Porcelli, 2003) can be counted.

In processes dealing with endothermic reactions, it is necessary to supply the required amount of heat at specific and controlled rates in order to attain fair levels of conversion of raw materials and avoid impurities, i.e. byproducts of side reactions, unreacted matter, and resulting high separation costs. Likewise in exothermic processes, the excess heat must be removed from the system in order to avoid thermal run away or suppressed endothermic byproducts. Hence, fast endothermic (or exothermic) reactions need fast heat supply (or heat removal), which can be compensated by matching the suitable reactor type exhibiting proper fluid dynamics with the thermodynamic requirements of the desired chemical reaction(s) (Nilsson and Sveider, 2000).

The conventional heat exchanger can be considered to have an appropriate design for such purpose, since it is utilized for a similar task of heating (or cooling) the reaction media or a process stream indirectly via a duty stream. Therefore it is suggestible that a heat exchanger unit with regular design characteristics could be used to provide the thermodynamic necessities of a reaction system via direct application, the reaction and heat transfer can both be accomplished inside the exchanger. This idea presents the concept of HEX reactors (Ismagilov *et al.*, 2001).

Nilsson and Svedier (2000) conducted a study based on the idea described in which they used a commercially available plate heat exchanger unit from Alfa Laval Thermal™.

Two sets of experiments were conducted on a non-catalytic reaction system called the Walker scheme to investigate the effects of micromixing and cooling. Mixing at molecular level was ensured by high Reynolds numbers of the reacting stream, and reactor performance was measured in terms of byproduct formation. It was reported that both parameters are beneficial for effective reactor performance.

In the light of this and other similar studies (Bayer *et al*., 2005; Anxionnaz *et al.*, 2008) it can be said that HEX reactors exhibit higher yields and selectivities, better energy savings; they result in fewer unit operations and thus cheaper processes, are more compact and provide safer operating conditions and better control of the reaction(s). Therefore, it can be suggested that HEX type reactors like plate reactors and microchannel reactors can also show reasonable performance due to diminished mass and heat transfer resistances provided by small channel sizes and smaller distances between channels.

Instead of the heating medium employed in HEX reactors, an exothermic reaction can also supply the heat requirement of an endothermic reaction at high temperatures. A system similar to HEX type reactors coupling an endothermic reaction with an exothermic reaction can be considered as multifunctional since the concept of multifunctional reactors describes reaction equipments in which several process functions like mass, energy and momentum transport or separate reactions are integrated (Zanfir and Gavriilidis, 2003). Multifunctional reactors make the process more efficient and compact and result in large reductions in the operational and capital costs (Dautzenberg and Mukherjee, 2001; Freide *et al.*, 2003; Ramaswamy *et al*., 2006).

Two types of methods are used for combining the heat absorbing endothermic reaction with the heat generating exothermic reaction. The first one is a direct method which comprises in situ and chronologically segregated heat generation (Zanfir and Gavriilidis, 2003). In situ heat generation runs both the endothermic and exothermic reactions in parallel, in the same mixture (Figure 2.2(a)). Examples of such a set up include in situ hydrogen combustion in oxidative dehydrogenations where performances of several catalysts are compared (Grasselli *et al.*, 1999a; b) and the roles of oxidative and non-oxidative chemistry as well as the roles of heterogeneous and homogeneous chemistry on ethane dehydrogenation are investigated (Henning and Schmidt, 2002). Another example is

the coupling of methane steam reforming with catalytic oxidation of methane (Ma and Trimm, 1996; Avcı *et al*., 2001).

There are two time cycles in chronological segregation (Figure 2.2(b)) which utilizes heat storage in the fixed bed. The bed is heated in the exothermic cycle and the heat thus stored is consumed in the endothermic cycle by the reaction mixture in reverse flow (van Sint Annaland and Nijssen, 2002). Mathematical simulation results for several types of reactors for methane conversion to synthesis gas via catalytic partial oxidation of methane coupled with simultaneous steam reforming were compared by Gosiewski (2001). The reactor models used in these simulations utilized heat generated via chronological segregation.

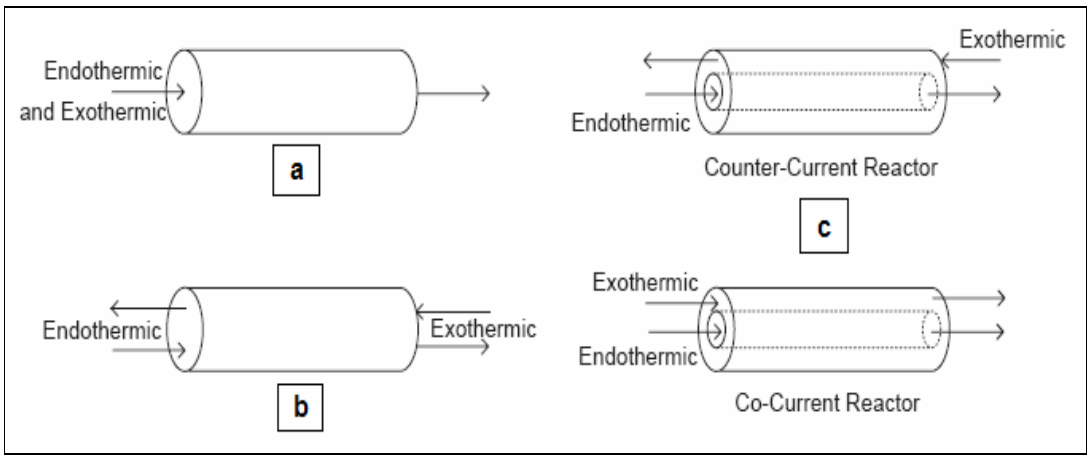

Figure 2.2. Various reactor configurations for coupling exothermic and endothermic reactions; (a) in situ heat generation, (b) chronologically segregated, (c) spatially segregated (Ramaswamy *et al.*, 2006)

One of the major concerns in directly coupled in situ reactors is that the catalyst used should preferably favor both exothermic and endothermic reactions or, in any case, should not get damaged by the exothermic reaction. If a physical mixture of two different catalysts is used, heat transfer between the two may limit conversion (Ma and Trimm, 1996). For the chronological reactor, on the other hand, hot spots that can damage the catalyst and the reactor material can occur (Kulkarni and Duduković, 1998; Gosiewski, 2001). Another limitation in these reactors is that the exothermic and endothermic reactions must be carefully selected so that the separation and purification of the products are minimized or

avoided since both the reactant mixture and product mixtures run through the same channel, and simultaneously in directly coupled adiabatic reactors, i.e. the type with in situ heat generation mechanism (Ramaswamy *et al*., 2006).

The second method for heat generation is the indirect transfer method in which the endothermic and exothermic processes are spatially segregated like heat exchanger reactors in Figure 2.2(c). Here, the products of the endothermic reaction are always separated from the combustion products. Since the exothermic side is spatially separated from the endothermic side, air can also be used for combustion instead of oxygen and the problem of nitrogen separation from the product mixture does not exist, which in turn reduces the capital cost resulting from the installation of an oxygen separation unit and/or the operational cost caused by compressing the air (along with nitrogen) to the process pressure. Heat exchanger reactors offer other operational flexibilities since operating parameters of exothermic and endothermic streams, such as the inlet velocity, feed concentration, etc. can be adjusted separately without affecting each other (Zanfir and Gavriilidis, 2003; Ramaswamy *et al.*, 2006).

The use of catalytic combustion for providing the heat required has various advantages (Hayes and Kolaczkowski, 1997). First, the reaction proceeds at lower temperatures than in homogeneous combustion, thus reducing NO_x formation. Lower operating temperature poses fewer constraints for materials of construction. The operating window in terms of inlet fuel concentration is expanded. Since it is a flameless process, long radiation paths needed in conventional furnaces are replaced by channel dimensions of a few mm in the plate matrices, with an observable impact on reactor size. Therefore, it can be said that catalytic operation enhances the intensification of the reactor.

Reay (1993) has explained the benefits of catalytic combustion in spatially segregated heat producing reactor systems, mentioning the growing interest in process intensification and developments in compact heat exchanger technology, opportunities coming up for exploitation of catalyst technology in combustion systems, namely compact reactors. Catalytic plate reactors (CPR) are presented as exemplary units where advantages of catalytic combustion and intensified compact heat exchangers and reactors can be combined.

Coupling an endothermic reaction with an exothermic reaction, both catalytic, in a spatially segregated fashion in a plate heat exchanger having both sides of the plates covered with appropriate catalysts results in a compact and intensified unit called catalytic plate reactor (CPR) (Zanfir and Gavriilidis, 2001). In such a configuration, the exothermic and endothermic streams flow in adjacent but separate channels which form when the plates are assembled on top of each other in a cascade like fashion. The interior walls of the channels are covered with the same type of catalyst, so that only one kind of reaction takes place inside the channel, which is a main advantage of the spatial segregation. The heat generated by the exothermic reaction is used by the endothermic reaction. As a result, heat removal is facilitated for the former while heat supply is facilitated for the latter. The flow arrangement can either be co-current or counter-current.

Examples of earlier studies that reveal the operational principles of the system (Branch and Tomlinson, 1995) and advantages of CPR over conventional systems (Charlesworth *et al.*, 1995) include theoretical investigation of the feasibility of coupling methane reforming with catalytic combustion in a CPR. It was shown that such a reactor would be two orders of magnitude smaller than a conventional steam reformer but catalyst deactivation can have serious consequences on the operation and stability of the reactor.

More recent work on the subject makes use of better mathematical models; catalytic ethane dehydrogenation taking place in a CPR having catalytic methane total oxidation as heat source was modeled utilizing a two-dimensional model (Zanfir and Gavriilidis, 2001). The influences of parameters like catalyst loading, flowrates and wall thermal conductivity on reactor behavior were investigated. It was shown that the ratio of catalyst loadings for the two reactions must be carefully adjusted in order to avoid hot spots or insufficient reactant conversion. It was reported that utilization of a metallic wall makes possible efficient heat transfer between endothermic/exothermic reaction locations for small temperature differences; however, lower plate thermal conductivity can lead not only to significant radial but also to axial temperature gradients.

In another study performed by the same authors (Zanfir and Gavriilidis, 2002a; b), the influence of a number of design parameters like channel size, wall thickness and thermal conductivity, inlet temperature, composition and velocities, and kinetic parameters

on the thermal behavior and performance of a two-dimensional CPR model was investigated by parametric sensitivity analysis. It was found that the strongest influence on reactor sensitivity comes from the intrinsic kinetics of both exothermic and endothermic reactions and different catalysts can show similar thermal behavior and performance but exhibit different sensitivity behavior.

Later, two articles were published by the same group as a sequel to their previous work on modeling of the CPR. The first study described a theoretical study of methane steam reforming coupled with methane catalytic combustion in a CPR. The temperature profiles and reactor sizes were compared with those of the conventional reformer (Zanfir and Gavriilidis, 2003). The second article investigated the effects of flow arrangement on reactor thermal behavior. It was determined that although co-current operation was better in terms of safety and thermal balancing, counter-current operation yielded better conversions but caused very high transverse temperature gradients (Zanfir and Gavriilidis, 2004).

2.2. Endothermic Conversion of Hydrocarbons

2.2.1. Ethanol Steam Reforming for Hydrogen Production

Catalytic conversion of hydrocarbons to hydrogen with a purity level high enough for fuel cell operation requires the design of new selective catalysts, novel catalytic reactors and processes. Among oxygenated fuels, ethanol as a hydrogen source has the advantage of being producible by fermentation from renewable resources, is much less toxic, safer to handle and easier to transport (Önsan, 2007). Hydrogen production from bio-ethanol is an attractive route with an almost closed carbon loop since the CO_2 produced can be used for biomass growth (Comas *et al.*, 2004; Aupretre *et al.*, 2002). In the steam reforming of ethanol, reactant conversion and H_2 production levels can vary significantly with the type of catalyst and operational conditions; therefore, process engineering determines economic viability.

Steam reforming (SR) of hydrocarbons is a highly endothermic process and involves high reaction temperatures, generally >600 K for oxygenated and >1000 K for saturated

hydrocarbons. It can be shown by thermodynamic calculations that the reforming of oxygenated hydrocarbons requires much less energy per mol of H_2 produced than that of saturated hydrocarbons (Önsan, 2007). Nevertheless, the adiabatic temperature drops are fairly large, e.g. for methanol steam reforming, $\Delta T_{adiabatic}$ is > 400 K (Semelsberger *et al.*, 2004). Hence, external energy has to be provided for maintaining steam reforming reactions. Steam reforming of alcohols (except methanol) is described by the equation:

$$C_nH_{2n+2}O + (2n - 1)\ H_2O \rightarrow n\ CO_2 + 3n\ H_2 \qquad \Delta H_R < 0 \qquad (2.1)$$

Steam reforming of oxygenated hydrocarbons (methanol and ethanol) produces mostly CO_2, some of which is later converted to CO via the rapid reverse water-gas shift reaction that occurs in the reformer with hydrogen present. Catalyst deactivation by coke formation at higher temperatures can be minimized by proper selection of catalyst composition and addition of an adequate amount of water into the feed stream (Trimm and Önsan, 2001). The stoichiometric water to ethanol feed ratio is 3.0 for the CO_2 producing ethanol SR reaction; typically, a higher feed ratio is essential in order to obtain hydrogen without carbon formation (Garcia and Laborde, 1991; Mas *et al.*, 2006).

$$C_2H_5OH + 3\ H_2O \leftrightarrow 6\ H_2 + 2\ CO_2 \qquad \Delta H^0_{298} = +173.5\ \text{kJ mol}^{-1} \qquad (2.2)$$

The consideration of ethanol as a hydrogen source is new compared to methanol. Higher temperatures (600-1200 K) are required for ethanol steam reforming (SR) because of its C-C bond. A review of the catalysts used for hydrogen production by ethanol SR shows that ***(a)*** ethanol conversions and hydrogen yields depend on the type of catalyst, method of catalyst preparation and reaction conditions, and ***(b)*** among the catalysts reported, Co/ZnO, ZnO, Rh/Al_2O_3, Rh/CeO_2 and Ni/La_2O_3-Al_2O_3 exhibit better performance (Haryanto *et al.*, 2005). A more recent survey of ethanol SR discusses the influence of catalyst composition and process conditions on the distribution of products (Vaidya and Rodrigues, 2006a). Hydrogen production by ethanol SR takes place at atmospheric pressure, but necessitates high temperatures and high water-to-ethanol ratios. In addition to the supported nickel, cobalt, nickel-copper mentioned above, precious metals such as platinum, palladium and rhodium are also promising. The major drawbacks mentioned are formation of side products and carbon deposition (Barroso *et al.*, 2006).

Since ethanol steam reforming is endothermic, heat must be supplied to the system in order to keep it at a constant reaction temperature. Heat can be supplied either internally by co-feeding oxygen or air and oxidizing a portion of the ethanol at the expense of hydrogen production or externally by the total oxidation of ethanol or another fuel such as methane (Liguras *et al.*, 2004; Salge *et al.*, 2005).

$$C_2H_5OH + 3\ O_2 \rightarrow 2\ CO_2 + 3\ H_2O \qquad \Delta H^0_{298} = -1277\ \text{kJ mol}^{-1} \qquad (2.3)$$

$$CH_4 + 2\ O_2 \rightarrow CO_2 + 2\ H_2O \qquad \Delta H^0_{298} = -802\ \text{kJ mol}^{-1} \qquad (2.4)$$

When total oxidation and steam reforming occur on the same catalyst, the process is usually termed oxidative steam reforming (OSR) or indirect partial oxidation (IPOX). It is reported that feeding ethanol, water, and oxygen in a molar ratio of 1/1.8/0.6 causes the overall reaction to be thermally neutral, and under such conditions, the hydrogen concentration approaches ca. 70 per cent in the reactor exit stream (Cai *et al.*, 2007):

$$C_2H_5OH + 0.61\ O_2 + 1.78\ H_2O \leftrightarrow 2\ CO_2 + 4.78\ H_2 \qquad \Delta H^0_{298} = 0\ \text{kJ mol}^{-1} \qquad (2.5)$$

Reports on intrinsic kinetic studies of ethanol steam reforming proposing power-law rate equations over Ru/Al_2O_3 (Vaidya and Rodrigues, 2006b) and Pt-Ni/δ-Al_2O_3 (Örücü *et al.* 2008; Soyal-Baltacıoğlu *et al.*, 2008) show that ethanol conversion is directly proportional to ethanol partial pressure, and is either independent of or mildly inhibited by steam partial pressure; these reaction orders agree with previous results on ethanol steam reforming on Ni-based catalysts (Vaidya and Rodrigues, 2006a; Sun *et al.*, 2005). More recently, ethanol steam reforming over Co/Al_2O_3 at 673-973 K was also described by LHHW type kinetic models that also accounted for water-gas shift and ethanol decomposition reactions (Sahoo *et al.*, 2007).

The effects of active metal and support material on indirect partial oxidation (IPOX) of ethanol (i.e. total oxidation and steam reforming on the same catalyst) has recently been studied over various supported metal catalysts including Ni, Ni-Cu, Rh, Ni-Rh and Ir

(Fierro *et al.*, 2005; Kugai *et al.*, 2006; Biswas and Kunzru, 2007; Akdim *et al.*, 2008). The kinetics of IPOX is described by the simultaneous implementation of separate rate equations developed for the total oxidation and steam reforming of the hydrocarbon fuel considered as well as the rate equation for the water-gas shift reaction taking place concurrently in the IPOX reactor. One-dimensional reactor models formulated for the simulation of methane and methanol IPOX have been reported in the literature (Avcı *et al.*, 2001; Lattner and Harold, 2007).

2.2.2. Catalytic Ethane Dehydrogenation

Dehydrogenation of alkanes is an endothermic and equilibrium-limited process; hence ethane dehydrogenation, which is the primary source of the ethylene used industrially, requires high temperature, low hydrocarbon partial pressure and short residence times.

$$C_2H_6 \leftrightarrow C_2H_4 + H_2 \qquad \Delta H^o_{f,\,298} = 137 \text{ kJ/mol} \qquad (2.6)$$

Thermodynamic and kinetic factors indicate that temperatures as high as 750-1000^{o}C are required for sufficient reactant conversion. Low pressures are favorable in accordance with the rough estimate of equilibrium conversion calculated from

$$X_{eq} = \{K_P / (K_P + P)\}^{1/2} \qquad (2.7)$$

where P is the total pressure and K_P is the equilibrium constant for the dehydrogenation reaction. A standard pressure range of 1-5 atm is used in the industry where ethylene production is dominated by noncatalytic thermal cracking (van Goethem *et al.*, 2006).

New processes for the selective catalytic dehydrogenation of alkanes have been adopted more recently (Virnovskaia *et al.*, 2008). The alkanes used in commercial processes are generally propane and isobutane for production of propene and isobutene, respectively, and dehydrogenation is carried out over precious metal (e.g. Pt) or heavy metal (e.g. Cr) catalysts (van Goethem *et al*., 2007). Generally, steam, O_2 or CO_2 can be used as diluent to shift the equilibrium to the product side by removing the H_2 from the

reaction mixture (Henning and Schmidt, 2002; Shen *et al*., 2009). It has been illustrated that ethylene selectivites higher than 70 per cent can be achieved by oxidative dehydrogenation with approximately 70 per cent ethane conversion in microchannels coated with Pt, while the yields and selectivities reached over some other catalysts (Pt/Sn) can be as high as 80 and 84 per cent, respectively (Vincent *et al*., 2008).

Ethane dehydrogenation has been studied in a catalytic Pd-Ag membrane reactor with the aim of obtaining the rate expressions describing the intrinsic kinetics of the reaction (Gobina *et al*., 1995). Since the reaction is equilibrium-limited, removal of the hydrogen product by the Pd-Ag membrane shifted the thermodynamic equilibrium towards the product side; and the use of a reactive sweep gas on the other side of the membrane further shifted the reaction equilibrium. A study of ethane oxidative dehydrogenation to ethylene over a highly active and selective Ni-Nb-O mixed oxide catalyst has indicated that a dual-bed multi-tubular reactor with intermediate air injection is better than a single-bed design with higher ethylene production rates because of the higher ethylene selectivity obtained under low oxygen partial pressures (Lopez *et al*., 2008).

3. MATHEMATICAL MODEL OF THE CATALYTIC PLATE REACTOR

3.1. Catalytic Plate Reactor (CPR) Model Configuration

In processes with a potential, designs based on compact heat exchangers having one of the streams replaced with an ongoing chemical reaction are used to intensify the heat transfer in conventional non-adiabatic reactors. The advantages of such an approach were explained by Reay (1993) within the framework of catalytic plate reactors (Zanfir and Gavriilidis, 2001).

A catalytic plate reactor is essentially a plate heat exchanger having both sides of its closely spaced plates covered with appropriate catalysts and coupling an endothermic and an exothermic reaction in an efficient way, resulting in a compact and intensified unit. The heat needed by an endothermic reaction can be supplied by an exothermic reaction taking place on the other side of the plate, i.e. in the successive channel. Since the main idea is to have these plates and channels as thin as possible, the close linking of the heat source and the heat sink reduces the overall heat transfer resistance.

Figures 3.1 and 3.2 depict a representative configuration of the closely spaced plates of a CPR and the channels formed in between. The two sides of the steel plates are covered with two different types of catalysts, one side with the catalyst for the exothermic reaction, and the other side with the catalyst for the endothermic reaction. These coated plates are stacked up in the fashion shown in Figure 3.1 to ensure that a channel has the same type of catalyst on its interior walls, resulting in a configuration where endothermic and exothermic channels are located successively on top of each other.

In a co-current operation, the reactants of both the endothermic and exothermic reactions enter their corresponding channels from the same side, carry out the reaction on the catalyst layer while flowing through the channel, and leave the reactor from the other side as a mixture of products and remaining unreacted components. In Figure 3.1 the flow arrangement of the ethanol steam reforming-methane total oxidation coupled system is

displayed. Catalytic ethane dehydrogenation combined with methane total oxidation has a similar set up.

A single repetitive unit composed of the co-current flow of exothermic (methane oxidation) and endothermic reaction (ethanol steam reforming or ethane dehydrogenation) streams through two parallel channels with a solid wall in between across which heat is transferred is clearly noticeable in the CPR configuration. This unit forms a basis for the calculations (Figure 3.3).

Due to the symmetry at the channel centerlines, and under the assumption that the whole system is adiabatic, the entire reactor can be modeled based on this single unit. Therefore, the representation of a basic unit as shown in Figure 3.3 will suffice, instead of the total system in Figures 3.1 and 3.2.

The dimensions of the basic unit as applied in the model and in the simulations are also given in Figure 3.3. The channel height is 2 mm for each and due to symmetry at the centerlines, only half of the channel height is incorporated in the model. The thicknesses of the catalytic layers are taken as 0.1 mm. For the base case, the wall thickness is taken to be the same as the channel height, 2 mm. The length and width of the wall, and therefore of the entire reactor are 0.5 m and 1 m, respectively. Since this is a two-dimensional model, the width is used only for calculating the cross-sectional area of the channels, which is incorporated into the volumetric flowrate calculation from inlet average velocities.

In order to obtain desired ethanol SR and ethane dehydrogenation conversion levels (>80% and >60%, respectively), high temperatures in excess of 1100 K are needed (Avcı *et al.*, 2009). Early simulations have shown that when the average inlet velocity and inlet concentration parameters were not adjusted in the manner shown in Tables 4.1. and 5.1, the endothermic reactions absorbed the exothermal heat generated by methane TOX immediately at the entrance of the channels, hence, the exothermic reaction could not actually kick-in and the temperatures along the reactor dropped from the set inlet values down to ca. 890 K which were insufficient to obtain the desired conversions. In order to overcome this effect, low inlet velocities in the exothermic channel and low reactant concentrations with higher inlet velocities in endothermic channel were utilized.

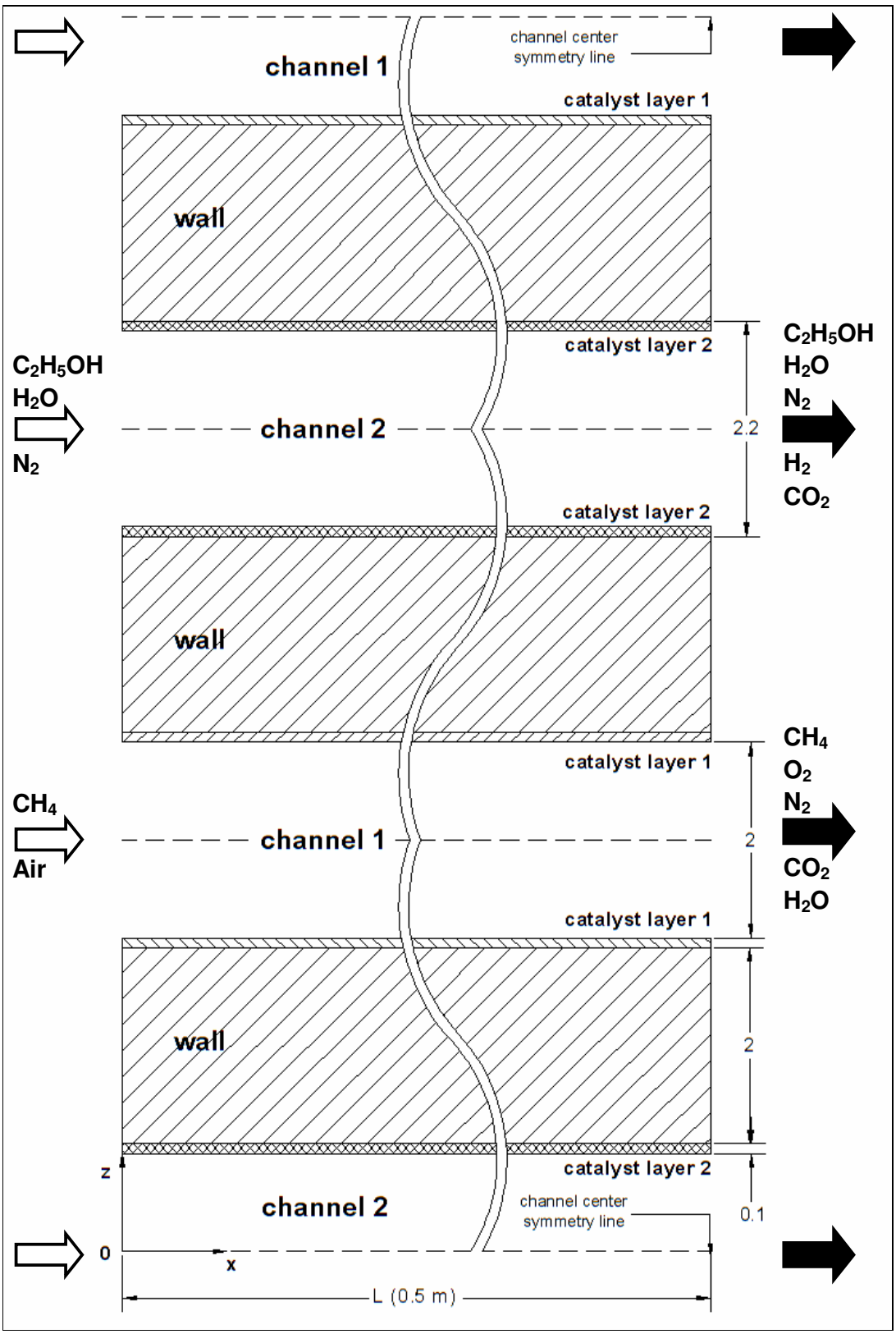

Figure 3.1. CPR configuration for ethanol steam reforming-methane oxidation coupling

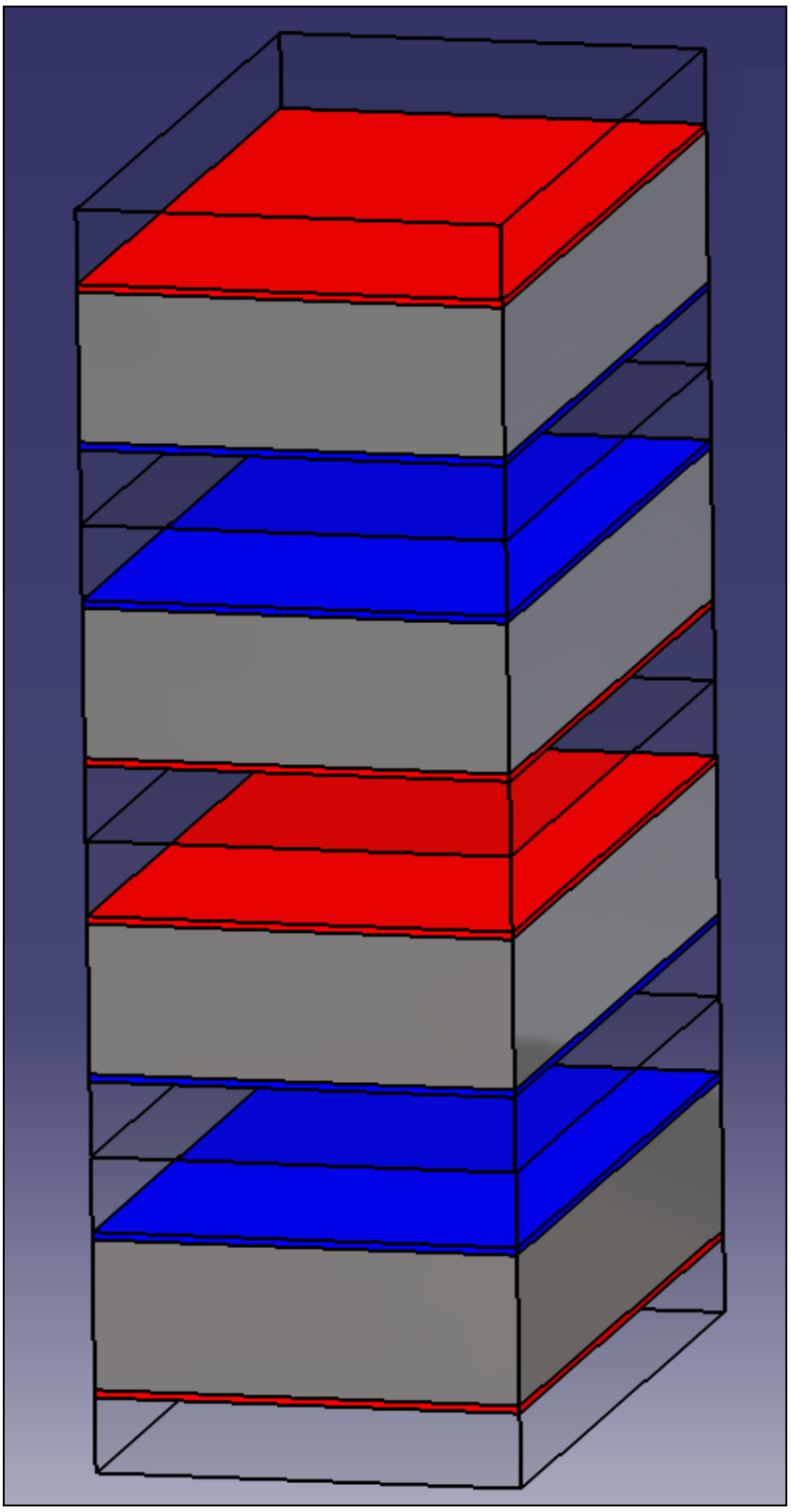

Figure 3.2. A representative three-dimensional view of CPR configuration, red plates: exothermic catalyst layers; blue plates: endothermic catalyst layers

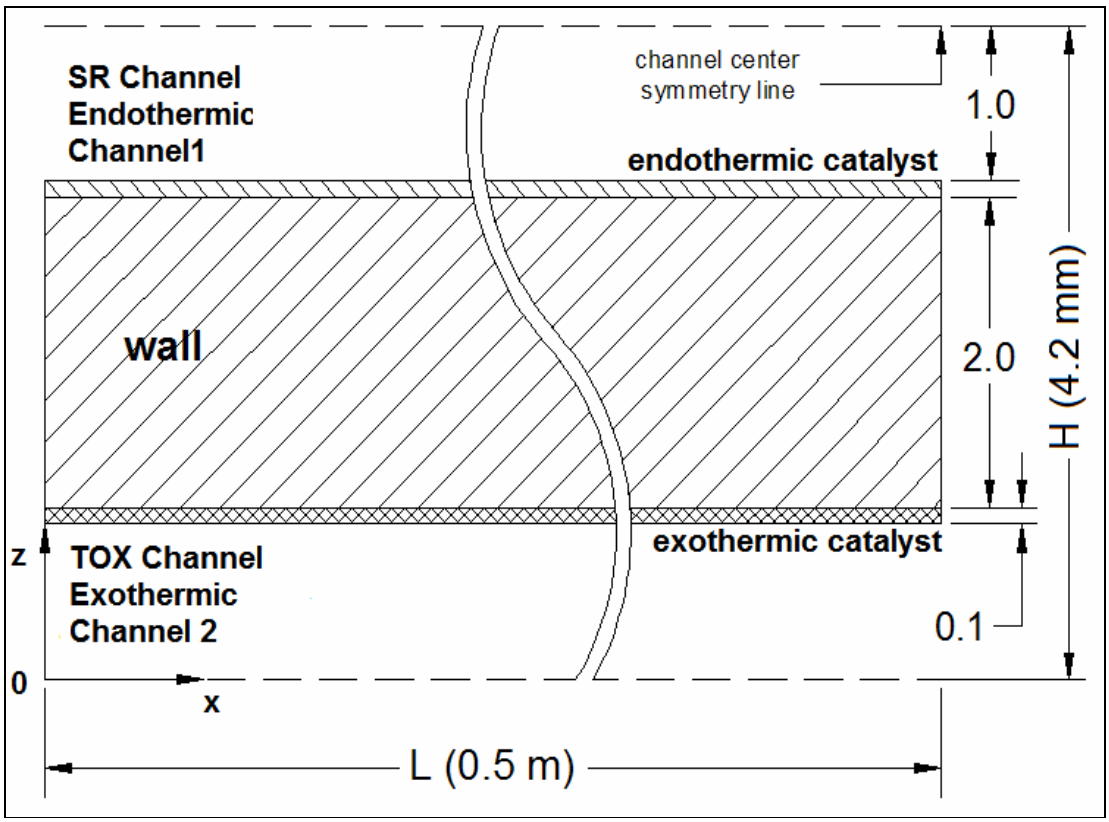

Figure 3.3. Basic unit of a CPR

Calculations are first carried out under the assumption of steady state conditions; the dynamic model is then solved via transient solvers. The model was constructed under the general assumptions that the gas mixtures are ideal and incompressible Newtonian fluids; therefore the ideal gas law is applicable; fully developed laminar flow prevails in the channels (as a matter of fact, this assumption is verified after the calculations since the Reynolds number turned out to be smaller than 345 for both channels everywhere in the reactor); homogenous reactions and possible side reactions are neglected (i.e. the chemical reactions are assumed to take place only in the catalyst layer); heat transfer by radiation is negligible, diffusive mass fluxes and conductive heat fluxes at channel outlets are assumed to be zero. The velocity distribution in the reactor is solved regardless of the influences of temperature and composition changes.

The conversion values of the reactants are calculated at the exit boundaries of the channels via the following equations which make use of the initial and final molar flowrates.

$$X_{ij} = \frac{F_{0ij}^{n} - \left\langle F_{ij}^{n} \right\rangle\Big|_{x=L}}{F_{0ij}^{n}} \tag{3.1}$$

where; X_{ij} is the conversion of species *i* in channel *j* at the exit,

F_{0ij}^{n} is the initial molar flowrate of species *i* in channel *j*, and

$\left\langle F_{ij}^{n} \right\rangle\Big|_{x=L}$ is the mean molar flowrate of species *i* in channel *j* at the exit.

The mean molar flowrate at any axial location is calculated by the equation:

$$\left\langle F_{ij}^{n} \right\rangle\Big|_{x} = \frac{\int_{0}^{z=H} F_{ij}^{n} \upsilon_j dz\Big|_{x}}{\int_{0}^{z=H} \upsilon_j dz\Big|_{x}} \tag{3.2}$$

The point molar flowrate ($F_{ij}^{n}\big|_{x}$) in Equation 3.2 can be expressed in terms of concentration ($c_{ij}\big|_{x}$) and volumetric flowrate ($F_{ij}^{v}\big|_{x}$) at that location,

$$F_{ij}^{n}\left[mol/s\right] = c_{ij}\left[mol/m^3\right] \times \underbrace{F_{ij}^{v}\left[m^3/s\right]}_{\upsilon_j\left[m/s\right] \times A\left[m^2\right]} \tag{3.3}$$

As a result,

$$F_{ij}^{n}\left[mol/s\right] = c_{ij}\left[mol/m^3\right] \times \upsilon_j\left[m/s\right] \times A\left[m^2\right] \tag{3.4}$$

This is then incorporated into Equation 3.2 as follows:

$$\left\langle F_{ij}^{n} \right\rangle\Big|_{x} = \frac{\int_{0}^{z=H} F_{ij}^{n} \times \upsilon_j dz\Big|_{x}}{\int_{0}^{z=H} \upsilon_j dz\Big|_{x}} = \frac{\int_{0}^{z=H} c_{ij} \times F_{ij}^{v} \times \upsilon_j dz\Big|_{x}}{\int_{0}^{z=H} \upsilon_j dz\Big|_{x}} = \frac{\int_{0}^{z=H} c_{ij} \times \upsilon_j \times A \times \upsilon_j dz\Big|_{x}}{\int_{0}^{z=H} \upsilon_j dz\Big|_{x}} \tag{3.5}$$

After solving the model, the temperature and concentration profiles are obtained along axial and radial directions. The influence of dimensional parameters such as wall thickness, wall material, and the operational parameter ratio of the reactants are investigated.

3.2. Model Equations and Boundary Conditions

A two-dimensional model has been developed for the CPR in order to determine the exit reactant conversions as well as the temperature distributions inside the reactor. The geometry of the representative CPR model is presented in Fig. 3.3 with the necessary dimensions, and Figure 3.2 displays a three-dimensional view for better comprehension.

Five different subdomains can be identified in Figure 3.3, namely, reforming channel, catalyst layer for reforming, solid wall (plate itself), catalyst layer for catalytic total oxidation and oxidation channel. Thus, a total of three different types of subdomains are present and each must be modeled accordingly.

The mathematical model developed includes momentum, heat and mass balances for gas and solid phases. The transport mechanisms considered are convection and conduction for heat transfer, convection and diffusion for mass transfer, all occurring in both axial and transverse directions.

The catalyst layer thickness is one tenth of a millimeter (Figure 3.3), meaning that the layers have a height over length ratio (δ_c / L) of 2×10^{-4}. In a situation like this, the layers could be modeled by using a one-dimensional approach (Zanfir and Gavriilidis, 2003). However, since the gas stream flows through and reactions take place inside the porous catalyst layer subdomains, the temperature and concentration variations in both axial and transverse directions are taken into account in the present work.

The mathematical model constructed consists of a system of partial differential equations (PDEs) that describe mass balances of ethanol, water, carbon dioxide and hydrogen in the steam reforming channel and the catalyst layer (or of ethane, ethylene and hydrogen in the ethane dehydrogenation channel and the catalyst layer), mass balances of

methane, oxygen, carbon dioxide and water in the methane total oxidation channel and the catalyst layer, and heat balances in each subdomain. The equations are given for the steady state model first; and the dynamic model versions are listed later in the text.

The momentum balances in the channel domains are modeled using the Navier-Stokes equations of motion, which include both convective and diffusive terms, for incompressible Newtonian fluids with constant density, ρ, and viscosity, μ. In the porous catalyst layer domains, Brinkman equations are used. Porosity and permeability of the catalyst layers are taken to be 0.4 and 10^{-8}, respectively (Avcı *et al.*, 2009). The model equations are listed below according to the subdomains in which they apply.

For the gas phase flowing through the channels the equation of continuity (incompressible fluid) is:

$$\frac{\partial \upsilon_{xj}}{\partial x_j} + \frac{\partial \upsilon_{zj}}{\partial z_j} = 0 \tag{3.6}$$

Equations of motion for the same subdomain in axial and transverse directions are:

$$\rho_j \left(\upsilon_{xj} \frac{\partial \upsilon_{xj}}{\partial x_j} + \upsilon_{zj} \frac{\partial \upsilon_{xj}}{\partial z_j} \right) = -\frac{\partial P_j}{\partial x_j} + \mu_j \left[\frac{\partial^2 \upsilon_{xj}}{\partial {x_j}^2} + \frac{\partial^2 \upsilon_{xj}}{\partial {z_j}^2} \right] \tag{3.7}$$

$$\rho_j \left(\upsilon_{xj} \frac{\partial \upsilon_{zj}}{\partial x_j} + \upsilon_{zj} \frac{\partial \upsilon_{zj}}{\partial z_j} \right) = -\frac{\partial P_j}{\partial z_j} + \mu_j \left[\frac{\partial^2 \upsilon_{zj}}{\partial {x_j}^2} + \frac{\partial^2 \upsilon_{zj}}{\partial {z_j}^2} \right] \tag{3.8}$$

For the gas phase flowing through the porous catalyst layers Brinkman equations (for flow thorough porous media) in axial and transverse directions are used:

$$\left(\frac{\mu_j}{\kappa} \right) \upsilon_{xj} = -\frac{\partial P_j}{\partial x_j} + \left(\frac{\mu_j}{\varepsilon_p} \right) \left[\frac{\partial^2 \upsilon_{xj}}{\partial {x_j}^2} + \frac{\partial^2 \upsilon_{xj}}{\partial {z_j}^2} \right] \tag{3.9}$$

$$\left(\frac{\mu_j}{\kappa}\right)v_{zj} = -\frac{\partial P_j}{\partial z_j} + \left(\frac{\mu_j}{\varepsilon_p}\right)\left[\frac{\partial^2 v_{zj}}{\partial x_j{}^2} + \frac{\partial^2 v_{zj}}{\partial z_j{}^2}\right] \tag{3.10}$$

The energy balances are represented by two-dimensional equations of energy for Newtonian fluids with constant density, heat capacity and thermal conductivity (ρ, C_p and k); and for solids with temperature dependent ρ, C_p and k. Conduction and convection in both axial and transverse directions for the gas phase and gas flowing through catalyst layer domains; and only conduction in both directions for the solid wall domain are considered. The equation considering the catalyst layer also contains the heat generation/consumption terms.

For the gas phase flowing through the channels the equation of energy is:

$$\rho_j C_{pj}\left(v_{xj}\frac{\partial T}{\partial x_j} + v_{zj}\frac{\partial T}{\partial z_j}\right) = k_j\left[\frac{\partial^2 T}{\partial x_j{}^2} + \frac{\partial^2 T}{\partial z_j{}^2}\right] \tag{3.11}$$

The equation of energy for the gas phase flowing through the porous catalyst layers where heat generation/consumption takes place is:

$$\rho_j C_{pj}\left(v_{xj}\frac{\partial T}{\partial x_j} + v_{zj}\frac{\partial T}{\partial z_j}\right) = Q + k_{j-eff}\left[\frac{\partial^2 T}{\partial x_j{}^2} + \frac{\partial^2 T}{\partial z_j{}^2}\right] \tag{3.12}$$

The equation of energy for the solid reactor wall contains only conduction terms:

$$k_s\left[\frac{\partial^2 T_s}{\partial x_s{}^2} + \frac{\partial^2 T_s}{\partial z_s{}^2}\right] = 0 \tag{3.13}$$

The convective and diffusive terms in both axial and transverse directions are accounted for in the species mass balance equations. The equations considering the catalyst layer also contain the rates of the chemical reactions as the generation/consumption terms.

The mass transfer equations are formulated for fluids with constant ρ and D. The equation of continuity, i.e. the mass balance equation, for the gas phase flowing through the channels is:

$$\upsilon_{xj}\frac{\partial c_{ij}}{\partial x_j}+\upsilon_{zj}\frac{\partial c_{ij}}{\partial z_j}=D_{AB}\left[\frac{\partial^2 c_{ij}}{\partial x_j^{\,2}}+\frac{\partial^2 c_{ij}}{\partial z_j^{\,2}}\right] \tag{3.14}$$

The gas flowing through the catalyst layers have a mass balance equation as:

$$\upsilon_{xj}\frac{\partial c_{ij}}{\partial x_j}+\upsilon_{zj}\frac{\partial c_{ij}}{\partial z_j}=D_{AB,eff}\left[\frac{\partial^2 c_{ij}}{\partial x_j^{\,2}}+\frac{\partial^2 c_{ij}}{\partial z_j^{\,2}}\right]+R_{ij} \tag{3.15}$$

The boundary conditions in the flow domains, i.e. the channels and catalyst layers, imposed on the momentum transport process can be listed as follows:

Plug-flow velocities are assumed and definite inlet values are assigned for each channel at channel inlets, atmospheric pressure (10^5 Pa) is specified at the channel outlets, the impermeable wall-catalyst layer interfaces and the boundaries of the catalyst layers located at:

- for endothermic reaction catalyst-catalyst layer 1:
  $x = 0$, $z = [3.1, 3.2]$ and $x = 0.5$, $z = [3.1, 3.2]$;

- for exothermic reaction catalyst-catalyst layer 2:
  $x = 0$, $z = [1, 1.1]$ and $x = 0.5$, $z = [1, 1.1]$; have no-slip conditions,

and the channel centerlines have symmetry conditions.

For the boundary conditions for the mass transfer process: initial concentration values are set for each chemical species, diffusive flux is assumed to be zero at the exit of the channels, the boundaries of the catalyst layer and the wall-catalyst layer interface defined above have insulation, and the channel centerlines are assumed to have symmetry.

And the energy transfer process has the following boundary conditions and assumptions: the gas streams at the channel entrances are assumed to be preheated and initial temperature values are set for each channel, zero conductive heat flux condition is applied for channel outlets, the previously defined boundaries of the catalyst layers and the lateral sides of the wall at $x = 0$ and $x = 0.5$ have thermal insulation and symmetry boundary condition is applied on channel centerlines.

The model equations are solved with these boundary conditions, and the coordinates are defined in Figure 3.3.

The boundary conditions described above in words are grouped according to their locations in the reactor and given in the form of mathematical expressions in the following equations;

- boundary conditions for momentum, mass and energy balances, respectively, on channel centerlines; $z_1 = H$ and $z_2 = 0$, $\forall x$; (symmetry conditions):

$$\mathbf{n} \cdot \upsilon_j = 0 \tag{3.16}$$

$$\mathbf{n} \cdot \left(- D \nabla c_{ij} + c_{ij} \upsilon_j \right) = 0 \tag{3.17}$$

$$\mathbf{n} \cdot \left(- k_j \nabla T_j + \rho_j C_{pj} T_j \upsilon_j \right) = 0 \tag{3.18}$$

- boundary conditions for momentum, mass and energy balances, respectively, on channel inlets; $x = 0$, $z_1 = [3.1, H]$ and $z_2 = [0, 1]$:

$$\upsilon_j = \upsilon_j^0 \tag{3.19}$$

$$c_{ij} = c_{ij}^{0} \tag{3.20}$$

$$T_j = T_j^{0} \tag{3.21}$$

- boundary conditions for momentum, mass and energy balances, respectively, on channel outlets; $x = L$, $z_1 = [3.1, H]$ and $z_2 = [0, 1]$:

$$P_j = P_{out} \tag{3.22}$$

$$\mathbf{n} \cdot \left(- D \nabla c_{ij} \right) = 0 \tag{3.23}$$

$$\mathbf{n} \cdot \left(- k_j \nabla T_j \right) = 0 \tag{3.24}$$

- boundary conditions for energy balance on wall boundaries; $x = 0$ and $x = L$, $z = [1.1, 3.1]$:

$$\mathbf{n} \cdot \left(- k_s \nabla T_s \right) = 0 \tag{3.25}$$

The density, thermal conductivity, viscosity and heat capacity of nitrogen are used for the corresponding parameters of all gas mixtures since the flow in the channels consists mostly of nitrogen. The mentioned parameters of the streams are assumed to stay constant regardless of the temperature changes but the values used are calculated at the average operating temperature of the systems.

The density value is estimated by the ideal gas equation of state for the average value of the operating temperature range. The thermal conductivity and viscosity given as functions of temperature are calculated for the average operating temperature using the correlations existing in the literature (Lemmon and Jacobsen, 2004). The effective thermal conductivity and effective diffusivity for the catalyst layers are assumed to be the same as those of the gas mixture. The mass diffusivities of the chemical species are taken to be identical and constant. Typical value of the gas phase effective diffusivity obtained from

Cao *et al.* (2005), 1.8×10^{-5} $m^2.s^{-1}$ is used in the model. The heat capacity value is calculated for the average operating temperature by using the temperature dependent correlations provided by Sinnot (2000). The thermal conductivity of the solid wall is represented as a piecewise polynomials function of temperature in COMSOL™ software, and thus can vary with changing temperature axially and transversely along the reactor.

3.3. Kinetic Expressions

The kinetic expressions related to the rate of methane combustion (catalytic total oxidation) are obtained from the literature (Ma and Trimm, 1996), where intrinsic kinetics of methane oxidation on a Pt/Al_2O_3 catalyst are described by the equations given below.

$$r_{CH_4} = \frac{-\mathrm{d}CH_4}{\mathrm{d}t} = \frac{k_1 \kappa_{CH_4} P_{CH_4} \sqrt{\kappa_{O_2} P_{O_2}}}{\left(1 + \kappa_{CH_4} P_{CH_4} + \sqrt{\kappa_{O_2} P_{O_2}}\right)^2} \tag{3.26}$$

$$k_1 = A_1 \exp\left\{-\frac{E_1}{R_g T}\right\} \tag{3.27}$$

$$\kappa_{CH_4} = 4324.038 \exp\left\{-\frac{46553.71}{R_g T}\right\} \tag{3.28}$$

$$\kappa_{O_2} = 4.41\times10^{-3} \exp\left\{-\frac{61939.2}{R_g T}\right\} \tag{3.29}$$

The kinetic expressions for catalytic dehydrogenation of ethane to ethylene on a Pd based, alumina supported catalyst obtained in the presence of nitrogen as sweep gas were employed in the model (Gobina *et al*., 1995). The rate equation used and related data are as follows:

$$r_{C_2H_6} = k_1^0 \left[P_{C_2H_6} - \frac{P_{C_2H_4} P_{H_2}}{K_e} \right] \tag{3.30}$$

$$k_1^0 = A_1 \exp\left\{-\frac{E_1}{R_g T}\right\} \tag{3.31}$$

where E_1 = 75580 J / mol,

A_1 = 4.39 mol / (g_{cat}.s.atm).

The equilibrium constant is given by:

$$K_e(T) = A_e \exp\left\{-\frac{E_e}{R_g T}\right\}(atm) \tag{3.32}$$

where E_e = 143410 J / mol,

$A_e = 1.096 \times 10^7$ atm.

Ethanol steam reforming kinetics over Ni based and Al_2O_3 supported catalysts used in this work was proposed by Akpan *et al.* (2007) and obtained from Karakaya and Avcı (2009). The authors constructed several mechanistic kinetic models and conducted experiments for verification. The reaction rate has a first order dependency on ethanol concentration, as can be seen in Equation 3.33.

$$r_A = \frac{k_0 \exp\left(-\frac{E}{R_g T}\right)\left[C_A - \frac{C_C^2 C_D^6}{K_p C_B^3}\right]}{\left[1 + K_3 C_C + K_5 \frac{C_C C_D^{0.5}}{C_B}\right]} \tag{3.33}$$

where A: C_2H_5OH, B: H_2O, C: CO_2, D: H_2

$$K_p = \frac{S}{R_g} - \frac{(H / R_g)}{T} \tag{3.34}$$

and $K_3 = 4.48\times10^{10}$,

$K_5 = 7.28\times10^{6}$,

$k_0 = 3.26\times10^{13}$,

$E = 5.54\times10^{4}$ J/mol

The time-dependent versions of the model equations (Equations 3.7 to 3.15) to be used in the dynamic modeling of the CPR are given below.

The time dependent equations of motion are:

$$\frac{\partial v_{xj}}{\partial x_j} + \frac{\partial v_{zj}}{\partial z_j} = 0 \tag{3.6}$$

$$\rho_j\left(\frac{\partial v_x}{\partial t} + v_{xj}\frac{\partial v_{xj}}{\partial x_j} + v_{zj}\frac{\partial v_{xj}}{\partial z_j}\right) = -\frac{\partial P_j}{\partial x_j} + \mu_j\left[\frac{\partial^2 v_{xj}}{\partial x_j^{\,2}} + \frac{\partial^2 v_{xj}}{\partial z_j^{\,2}}\right] \tag{3.35}$$

$$\rho_j\left(\frac{\partial v_z}{\partial t} + v_{xj}\frac{\partial v_{zj}}{\partial x_j} + v_{zj}\frac{\partial v_{zj}}{\partial z_j}\right) = -\frac{\partial P_j}{\partial z_j} + \mu_j\left[\frac{\partial^2 v_{zj}}{\partial x_j^{\,2}} + \frac{\partial^2 v_{zj}}{\partial z_j^{\,2}}\right] \tag{3.36}$$

Time dependent Brinkman equations for flow through porous layers are:

$$\left(\frac{\rho}{\varepsilon_p}\right)\frac{\partial v_{xj}}{\partial t} + \left(\frac{\mu_j}{\kappa}\right)v_{xj} = -\frac{\partial P_j}{\partial x_j} + \left(\frac{\mu_j}{\varepsilon_p}\right)\left[\frac{\partial^2 v_{xj}}{\partial x_j^{\,2}} + \frac{\partial^2 v_{xj}}{\partial z_j^{\,2}}\right] \tag{3.37}$$

$$\left(\frac{\rho}{\varepsilon_p}\right)\frac{\partial v_{zj}}{\partial t} + \left(\frac{\mu_j}{\kappa}\right)v_{zj} = -\frac{\partial P_j}{\partial z_j} + \left(\frac{\mu_j}{\varepsilon_p}\right)\left[\frac{\partial^2 v_{zj}}{\partial x_j^{\,2}} + \frac{\partial^2 v_{zj}}{\partial z_j^{\,2}}\right] \tag{3.38}$$

The equations of energy for the dynamic model for gas flowing through channels is,

$$\rho_j C_{pj}\left(\frac{\partial T}{\partial t}+\upsilon_{xj}\frac{\partial T}{\partial x_j}+\upsilon_{zj}\frac{\partial T}{\partial z_j}\right)=k_j\left[\frac{\partial^2 T}{\partial {x_j}^2}+\frac{\partial^2 T}{\partial {z_j}^2}\right] \tag{3.39}$$

and for gas flowing through catalyst layers with heat generation/consumption is;

$$\rho_j C_{pj}\left(\frac{\partial T}{\partial t}+\upsilon_{xj}\frac{\partial T}{\partial x_j}+\upsilon_{zj}\frac{\partial T}{\partial z_j}\right)=Q+k_{j-eff}\left[\frac{\partial^2 T}{\partial {x_j}^2}+\frac{\partial^2 T}{\partial {z_j}^2}\right] \tag{3.40}$$

The conduction equation for the solid reactor wall is:

$$\rho_s C_{ps}\frac{\partial T}{\partial t}+k_s\left[\frac{\partial^2 T_s}{\partial {x_s}^2}+\frac{\partial^2 T_s}{\partial {z_s}^2}\right]=0 \tag{3.41}$$

The time dependent mass balance equation for the channels is,

$$\frac{\partial c_{ij}}{\partial t}+\upsilon_{xj}\frac{\partial c_{ij}}{\partial x_j}+\upsilon_{zj}\frac{\partial c_{ij}}{\partial z_j}=D_{AB}\left[\frac{\partial^2 c_{ij}}{\partial {x_j}^2}+\frac{\partial^2 c_{ij}}{\partial {z_j}^2}\right] \tag{3.42}$$

and for the catalyst layers with reaction is;

$$\frac{\partial c_{ij}}{\partial t}+\upsilon_{xj}\frac{\partial c_{ij}}{\partial x_j}+\upsilon_{zj}\frac{\partial c_{ij}}{\partial z_j}=D_{AB,eff}\left[\frac{\partial^2 c_{ij}}{\partial {x_j}^2}+\frac{\partial^2 c_{ij}}{\partial {z_j}^2}\right]+R_{ij} \tag{3.43}$$

3.4. Numerical Solution Method

In this section, the basic ideas behind the operating principles of the FEM (finite element method) analysis software utilized to solve the reactor model are described briefly, without venturing forth into complex mathematics. The coupled, two-dimensional steady

state/transient model equations (Bird *et al.*, 2002), are solved using the finite element method through the COMSOL Multiphysics™ CFD package.

The heat generation/consumption and reaction terms in the model equations are imported into the CFD software from the COMSOL™ Reaction Engineering Lab. These chemical reaction kinetics (Arrhenius parameters, kinetic expressions) and reaction thermodynamics properties (enthalpy, entropy and heat source of reaction) are introduced to the CFD software by the COMSOL™ Reaction Engineering Lab. The Reaction Engineering Lab™ solves mass and energy balances of the reaction for a type of reactor geometry chosen among the few standards and given initial conditions. After solution, the reaction system is exported to the Multiphysics package which contains the model equations for mass, momentum and energy balances for the CPR and the model geometry providing boundary conditions for these balances.

FEM is a numerical technique for obtaining approximate solutions to PDEs (partial differential equations) and systems of PDEs with boundary conditions (i.e. boundary value problems). The solution can be achieved by either eliminating the PDE completely, as in steady state problems, or transforming the PDE into an approximating system of ordinary differential equations, which can be solved by numerical integration techniques like the Runge-Kutta or the Euler method etc (COMSOL AB., 2007).

The general procedure of FEM is summarized in seven steps as follows (Kwon, 2005):

i. Model setup: Identification of the governing model equations (system of PDEs) of the system,

ii. FEM formulation: Introduction of integral form equations. This could be done by three methods;

    - Direct approach,
    - Variational approach,

- Method of Weighted Residuals approach.

The last two approaches which FEM utilizes are termed as “weak formulation” and result in “weak form equations” that are no longer required to hold absolutely and has approximate “weak solutions” that hold only with respect to certain trial functions.

iii. Discretization (Meshing): Conversion of the continuous domain into elements.

A mesh is a partition of the geometry model into small units of simple shapes. In this work, for the two-dimensional geometry of the model, a free (unstructured) meshing consisting of triangular elements is employed and the mesh is refined in the entrance region and the regions where high reaction rates are expected, i.e. the catalyst layers. The regular refinement method of COMSOL™ divides each element into four triangular elements of the same shape in two dimensions (COMSOL AB., 2007).

iv. Interpolation: Introduction of an approximation of the field variable over a mesh element (Figure 3.4) via “shape functions”.

$$\phi(x) = N_1(x)\phi_1 + N_2(x)\phi_2 + N_3(x)\phi_3 \qquad (3.44)$$

where ϕ_i are nodal values of the field variable and $N_i(x)$ are shape functions.

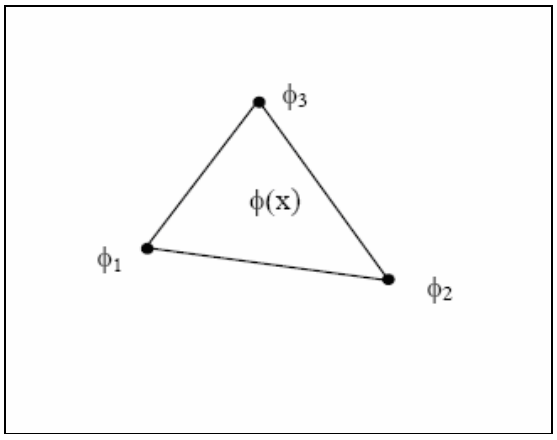

Figure 3.4. Interpolation on a mesh element via shape functions

v. Numerical integration: Evaluation of the integral form equations (the equation set for a single element, element matrix) over each element via numerical integration.

vi. Assembling: Assembling of the global matrix equation from element matrix equations, obtaining the sparse “stiffness” and “mass” matrices.

vii. Solution: Solution of the matrix to obtain the unknowns.

Considering the computational power of an available system, two issues are important for efficiency:

- storage techniques of the matrices, like frontal wave technique, bandwidth, skyline etc.
- solution techniques of the matrices, like Gauss elimination, Cholesky factorization, Gauss-Seidel iteration method, conjugate gradient method etc.

COMSOL™ Multiphysics includes a number of different solvers for PDE-based problems. The stationary and time-dependent solvers are used in the calculations carried out in this thesis. These solvers work on linear and nonlinear PDE problems. If a model is nonlinear, the software approximates it with a linear model, and solves the corresponding linearized version. Since the number of unknowns in these systems is usually very large, the most important solver parameter setting concerns the choice of the linear solver (COMSOL AB., 2007).

The direct solvers (UMFPACK, SPOOLES, PARDISO and TAUCS Cholesky) are preferable for one-dimensional and two-dimensional models; they solve a linear system by Gaussian elimination, a stable and reliable process well suited for ill-conditioned systems. Among the available four solvers, UMFPACK and PARDISO were utilized in the calculations. UMFPACK is a set of routines for solving unsymmetric sparse linear systems, using the Unsymmetric MultiFrontal method (Davis, 2009). The package PARDISO (parallel sparse direct solver) is software for solving large sparse symmetric and unsymmetric linear systems on shared memory multiprocessors (Schenk, 2007).

4. ETHANOL STEAM REFORMING - METHANE TOTAL OXIDATION

4.1. Steady-State Two-Dimensional Modeling of the CPR

4.1.1. The Base Case

In order to study and evaluate the influence of various parameters on CPR performance in coupling endothermic ethanol steam reforming with exothermic methane total oxidation, calculations are first carried out for a "base case", for which conditions are given in Table 4.1.

Table 4.1. Data used for base case ethanol steam reforming calculations

Operating Conditions		
Channel	Ethanol SR side	Methane TOX side
Inlet temperature (K)	900	900
Pressure (Pa)	10^5	10^5
Inlet composition (vol. %)	C_2H_5OH-H_2O-N_2 mixture	CH_4-air mixture
	1% C_2H_5OH	9.6% CH_4
	3% H_2O	19.2% O_2
	96% N_2	71.2% N_2
Inlet average velocities (m/s)	9	0.4
Reactor Geometry		
Catalyst layer thickness	0.1 mm	
Distance between plates	2 mm	
Plate Dimensions (L x w x δ_s)	0.5 m ×1 m × 2 mm	
Plate material	UNS G10060 (6% Carbon Steel)	
Channel cross sectional area	0.001 m^2	

One of the first issues to examine is the temperature distribution of the system. In the context of Chapters 4 and 5, the x and z coordinates shown in Figure 3.3, are termed as "axial" and "transverse" coordinates, respectively, in order to be consistent with Cartesian coordinates. Likewise, the endothermic channel, where ethanol steam reforming reaction takes place (ethane dehydrogenation in Chapter 5) and the exothermic channel with

methane total oxidation are frequently termed as “channel 1” and “channel 2”, respectively for brevity.

Figure 4.1 shows transverse temperature profiles across channel centerlines at various axial locations according to the orientation and dimensions in Figure 3.3. These figures are useful for describing the transverse temperature distribution.

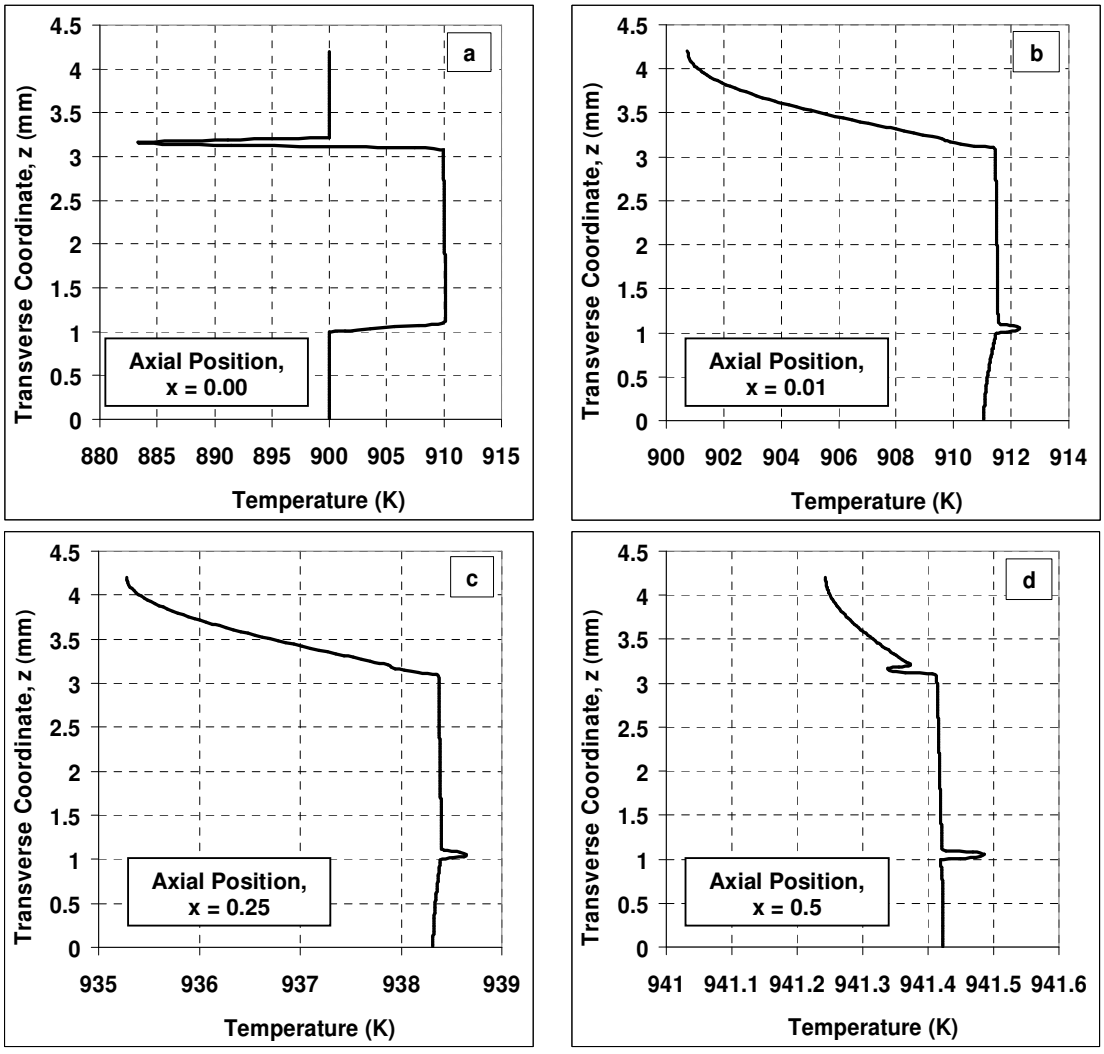

Figure 4.1. Transverse temperature profiles for base case at various axial locations

The gas mixtures at the inlet boundaries of both channels are at the inlet temperatures specified, 900 K, but temperature of the catalyst layer in the reforming channel entrance point; $x = 0$, $z = 3.15$; is 882.5 K, i.e. lower than the inlet temperatures (Figure 4.1(a)). This is due to the fact that the endothermic reforming reaction immediately starts consuming

heat in the reforming reaction mixture flowing through the porout layer, while the rate of the heat generating combustion reaction has yet to increase and the heat generated is yet to be transferred across the wall. Aside from heat generation, the high temperatures of the wall should have been able to prevent this cold spot. However, since the temperature value only 0.01 m downstream of the entrance (x = 0.01, z = 3.15) is above 911 K (Figure 4.1(b)), it can be said that the cold spot occurring at the entrance is a local and miniature-scale incident and disappears immediately due to the high temperatures of the metal wall.

Another noticeable feature in this figure is that despite the lack of sufficient heat generation by combustion reaction, the wall temperature is 10 K higher than the initial temperature because of the heat conducted axially from the downstream sections of the reactor. The analysis is done under steady state operation; therefore, the reactions are already proceeding at their maximum achievable rates. The downstream sections of the wall have higher temperatures, as can be seen from Figures 4.1(c) and (d), because the exothermic reaction gets faster and generates more heat further along the reactor axis. The difference between the temperatures of the exit and entrance sections of the reactor forms a driving force for heat transfer and the solid metal wall is a better medium than the gas stream flowing in the opposite direction. Therefore heat is transferred by conduction through the wall from the downstream sections to the entrance regions, contributing to increasing the temperatures along the reactor and causing the temperature of the wall at the entrance to be higher than the inlet temperatures of gas streams.

Figure 4.1(b) shows that the values of the temperatures are close to 900 K around the central region of the entrance of the reforming channel; $z \geq 4$, and are approximately 10 K lower than those of the catalyst layer and the wall. In other words, transverse temperature profile decreases from the wall to the channel center in the reforming channel. Such behavior is expected and is caused by the consumption of transferred heat by the catalyst layer, and in addition to this, the flowing mixture in the channel center has a higher linear velocity of approximately 12 m/s, as can be seen in Figure 4.2(a), which leaves less residence time for the gas mixture to absorb heat.

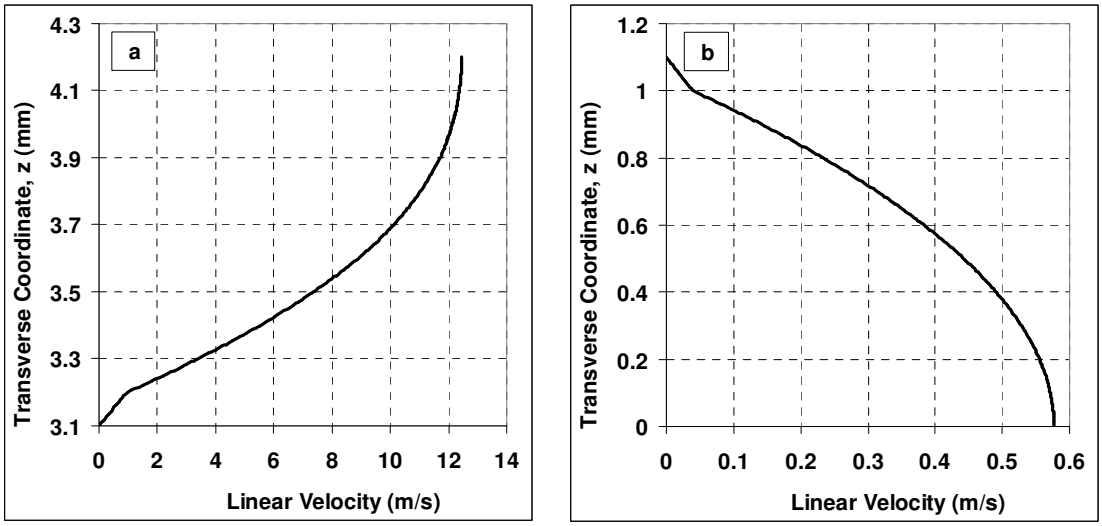

Figure 4.2. Linear velocity profiles across the channels for base case at axial position $x = 0.01$ for (a) channel 1-reforming and (b) channel 2-combustion

A similar situation is encountered in the combustion channel, but in a less significant manner, as would be expected. Temperature values in center of the entrance region of the channel ($x = 0.01$, $z = 0$) are only slightly (approximately 0.5 K) lower than those of the gas mixture-catalyst layer interface. The reason for this decrease is not quite the same as in the reforming channel; the heat is generated in the catalyst layer of this channel and then transferred across only the combustion channel to the channel center, having to overcome but a minor transfer resistance, instead of the additional transfer resistance of the wall. Also, the gas velocities in the combustion channel entrance are not greater than 0.6 m/s, which is 20 times less than that of reforming channel. Therefore, the central region and regions closer to the catalyst layer in the combustion channel have less linear velocity discrepancies (Figure 4.2(b)), and the gas in the channel center has a higher residence time than reforming channel, which facilitates heat transfer from the catalyst layer to the channel center.

Figures 4.1(c) and (d) representing narrower temperature ranges reveal that the wall becomes colder at its reforming end, and this is due to the heat consumption in the reforming catalyst layer. Sharp peaks in the plots are the temperature distributions of the catalyst layers, which are described in more detail in Figure 4.3. It is clear that these peaks become less significant further along the axis, if one is to notice that the abscissa of Figure 4.1(d) covers a temperature range of only 0.6 K.

The highest temperature is observed at the end of combustion channel catalyst layer, i.e. at $x = 0.5$, $z = 1.05$, as expected, since this is where exothermic reaction takes place and at the reactor exit the combustion reaction has the highest conversion value. Most of this heat is used to drive the endothermic reaction and the rest to heat the reaction mixtures in both channels. On the contrary, the lowest temperature, even lower than the initially set value, is observed at the beginning of reforming channel catalyst layer, 882.5 K, since this is where heat is consumed and at the reactor entrance the reaction has no heat supply other than the sensible heat of the gas mixture.

It is observed from Figures 4.1 and 4.3 that the combustion channel and the reactor wall have no significant temperature differences between each other along the axis and across the reactor. This statement is correct everywhere along the reactor except for a very small section of the entrance region where the rate of the exothermic reaction is not sufficient enough to supply the heat. The small temperature discrepancy between the centerline of the combustion channel, $z = 0$, and the reforming side of the wall, $z = 3.2$, is provided by the high thermal conductivity of the metal wall and the low heat transfer resistances due to the small channel size and wall thickness. However, the situation is different considering the reforming channel. The almost linear temperature distribution transversely across the reactor decreases once it reaches the reforming catalyst layer because this layer is where heat consumption takes place; also, the gas mixture flows much faster in this channel and through the porous catalyst layer. The transverse distribution becomes completely linear only towards the exit of the channels.

Towards the exit, i.e. as $x_4 = 0.5$ is reached, combustion becomes capable of sustaining the heat requirement of steam reforming, rendering the velocity difference ineffective, so the system reaches a thermo-neutral state, the transverse profiles become less symmetrical and eventually no sharp temperature gradients exist in the cross section, as depicted in Figure 4.3 which presents the plots in Figure 4.1 altogether for comparison.

A two dimensional temperature contour plot along the reactor is presented in Figure 4.4. Contours are isothermal lines and they help to describe the transverse temperature distribution. In addition, they show the temperature distribution inside the catalyst layers more clearly.

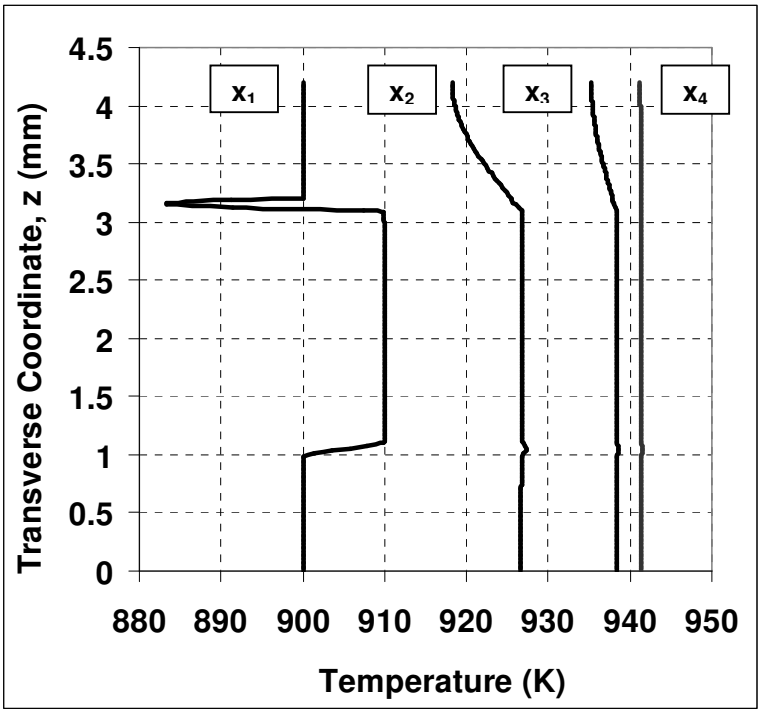

Figure 4.3. Transverse temperature profiles along the reactor for base case at various axial locations; $x_1 = 0.0$, $x_2 = 0.1$, $x_3 = 0.25$, $x_4 = 0.5$

The stacked up isothermal contour lines at the entrance of the combustion channel show that the temperature rises steeply in this region. Axially downstream the reactor, the contours are scattered, and get more widely apart towards the exit, which shows a slowdown of the steep heating up trend and a tendency towards a thermo-neutral state. This is due to the exothermic reaction balancing the heat consumption of the endothermic reaction.

Since the channel height is very small and the gas flow is slow in the combustion channel, the transverse isothermal lines are almost straight from the gas mixture-catalyst layer interface to the channel center.

The combustion catalyst layer shows an expected behavior. The combustion reaction, therefore the heat generation, takes place inside the catalyst layer, and the generated heat is transferred in both directions transversely, to the wall and to the gas mixture flowing in the channel via convection and conduction. This is why the center of the layer is hotter than the wall-layer interface and the gas mixture-layer interface.

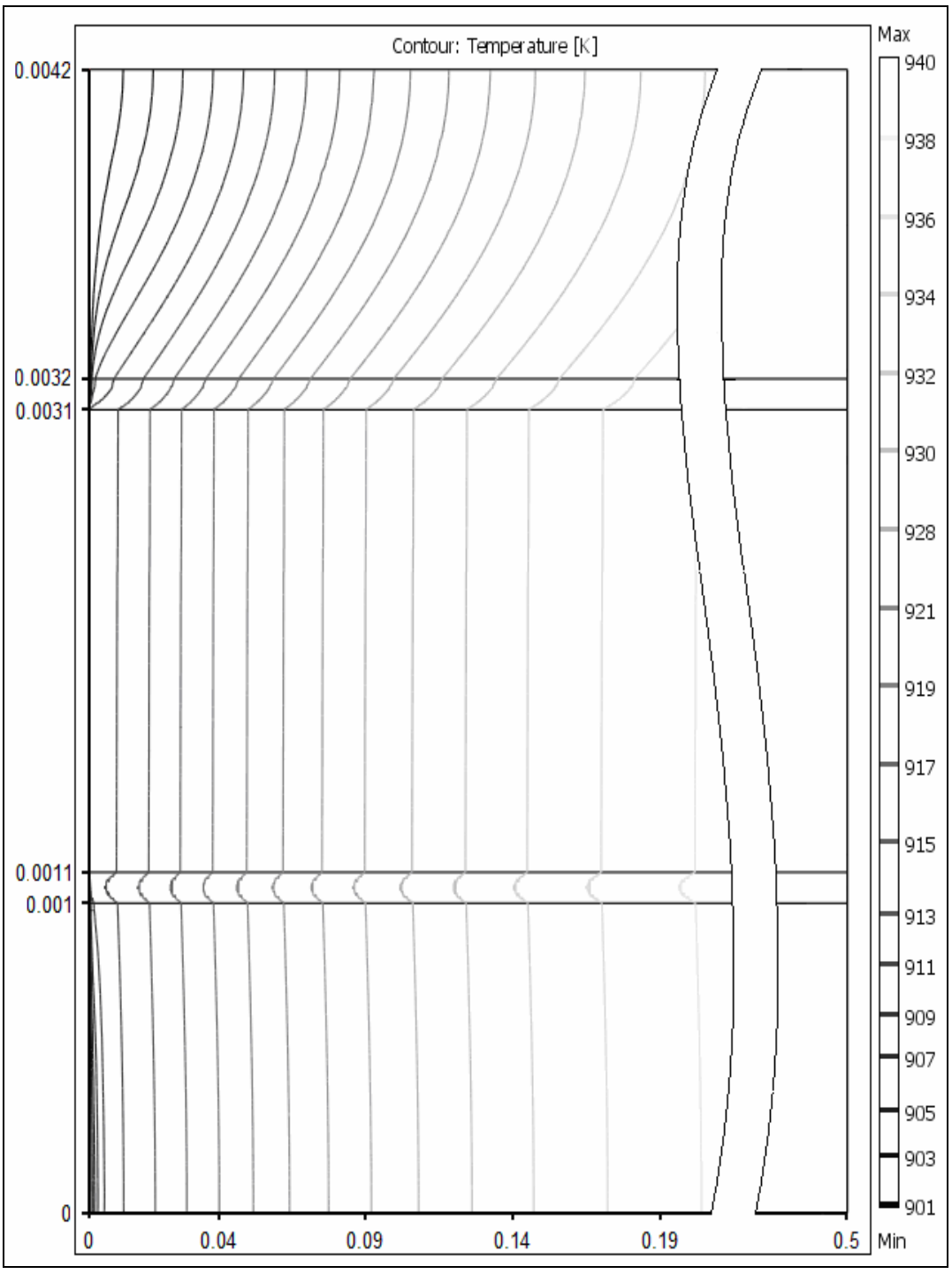

Figure 4.4. Isothermal contour lines for base case at reactor entrance (x_1 = 0.0)

Considering the reforming channel, the effects of the 22.5 times higher average inlet velocity is clearly visible in Figure 4.4. The isothermal contour lines in the reforming channel are distorted in the direction of the gas flow whereas in the combustion channel,

they are almost straight. In the reforming catalyst layer, a sudden decrease in the temperature due to the endothermic reaction taking place inside the layer is observed.

One of the main advantages of the CPR design can be observed when the metal wall is considered. The isothermal lines extending from heat source to the heat sink are straight. This means that heat is transferred across the wall with almost no resistance, and it is results from the small thickness and high thermal conductivity of the wall.

The axial temperature profiles in the channel centerlines given in Figure 4.5 indicate that the 10 K temperature difference observed between the two channels at the reactor entrance decreases gradually toward reactor exit. In addition, the temperature in the centerline of the reforming channel is always lower than that of the combustion channel, and this is due to higher flowrate of the former as compared to the latter with combustion channel being the heat generating side.

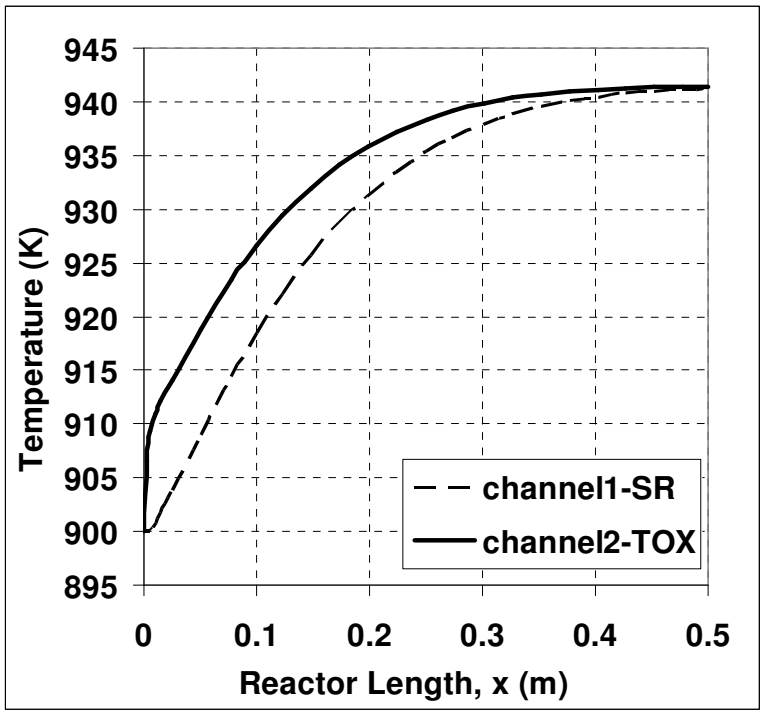

Figure 4.5. Axial temperature profiles of channel centerlines for base case

Temperature increases smoothly along the reactor length, except for the entrance of the combustion channel, and no hot spots develop. The exothermic reaction heats the

combustion channel first, causing the temperature to increase; when endothermic reaction begins to utilize the generated heat, heating up of the combustion channel slows down, the steep increase in the temperature stops and a balance is reached. The delay in the utilization of heat by the endothermic reaction is caused by the resistance of the wall against heat transfer, which can also be observed in Figure 4.4 where the isothermal contour lines in the combustion channel are packed closely at the entrance. In other words, the heat produced in the exothermic channel is trapped in the same channel. This is the reason why the temperature profile of the channel centerline of the exothermic side experiences a steep increase at the entrance of the reactor.

Figure 4.5 also shows that temperature values in the two channels are close to each other, especially towards the end of the reactor where they are almost the same. This demonstrates the efficient thermal communication between channels due to high solid wall conductivity and relatively small channel height. The gas mixtures in both channels leave the reactor at 941 K. Ethanol reaches 76.6% conversion and methane 86.7% conversion. It is worth noting that transverse temperature gradients are found to be insignificant, indicating efficient heat transfer across the reactor. Overall, the operating and design parameters chosen for the base case lead to efficient coupling of the two reactions, with a low temperature increase of 41 K axially and a low temperature difference of 10 K transversely along the reactor.

Soyal-Baltacıoğlu *et al.* (2008) studied ethanol steam reforming for H_2 production over Pt-Ni/δ-Al_2O_3 catalysts in a temperature interval of 673–823 K in order to explore the effects of metal contents of the catalysts and obtained a rate expression for the reaction. It was reported that at long times-on-stream (300 minutes) the best conversions with values close to 75% were obtained at 773 K which stayed constant until the system reached 823 K. Another study regarding ethanol steam reforming was performed by Örücü *et al.* (2008) over Pt-Ni with a different Pt content in a temperature range of 623–823 K. The highest conversion (ca. 100%) was achieved at 823 K in a long run of 400 minutes. It is reported that H_2 production increases dramatically with increasing temperature. The effect of water-to-ethanol ratio was also investigated, and it was found that a ratio twice the stoichiometric value gives a conversion value of 95% in short run times of 50 minutes, but in 400 minutes, conversion drops down to lower values (ca. 75%). In both experimental studies,

negative effects like coke deposition on catalysts and side reactions were negligible. Considering that the rate expression used for ethanol steam reforming in the present study was also obtained over a Ni-based catalyst (Akpan *et al.*, 2007), the ethanol conversion levels of ca. 75% calculated for the CPR at steady state seem reasonable.

4.1.2. Influence of Wall Thickness

The analysis in Section 4.1.1 clearly indicates that wall characteristics will have an effect on the heat transfer between channels and along the reactor, and wall thickness is expected to be important in this respect. The thicker the wall, the greater is the resistance to heat transfer, thus the temperature distributions are affected more significantly.

Calculations were based on a wall thickness of 2 mm up to this point. In order to demonstrate the effects of wall thickness, two cases were analyzed, keeping everything else constant. First is a "thin case" where the wall thickness is reduced to 1 mm, and second is a "thick case" with a wall having a thickness of 4 mm. Therefore a 4-fold overall difference in thickness is obtained between the two cases, making comparison easier. The temperatures in the channel centerlines along the reactor for the "thin case" (δ_s = 1 mm) and "thick case" (δ_s = 4 mm) are analyzed in Figures 4.6 and 4.7.

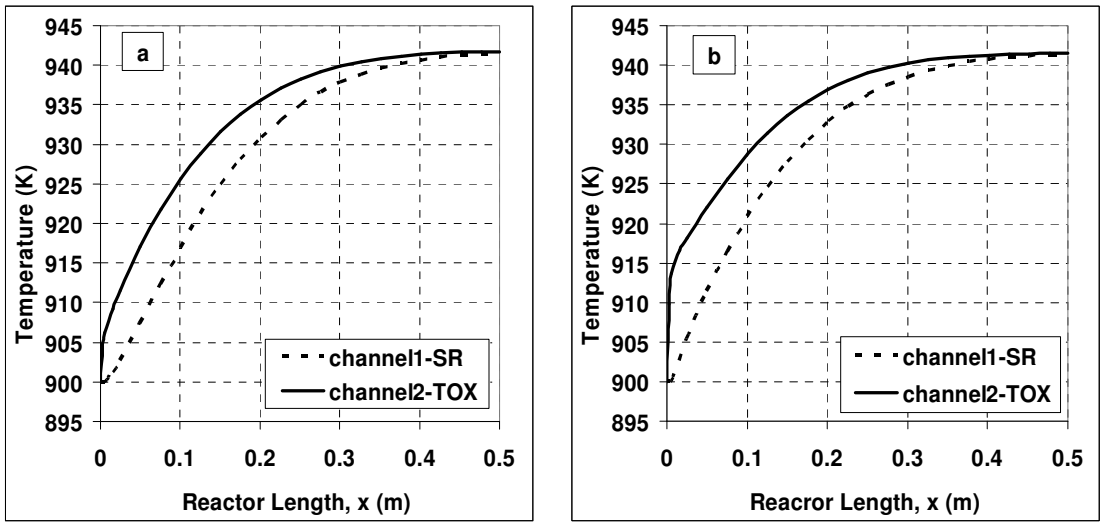

Figure 4.6. Axial temperature profiles of channel centerlines for (a) thin and (b) thick case

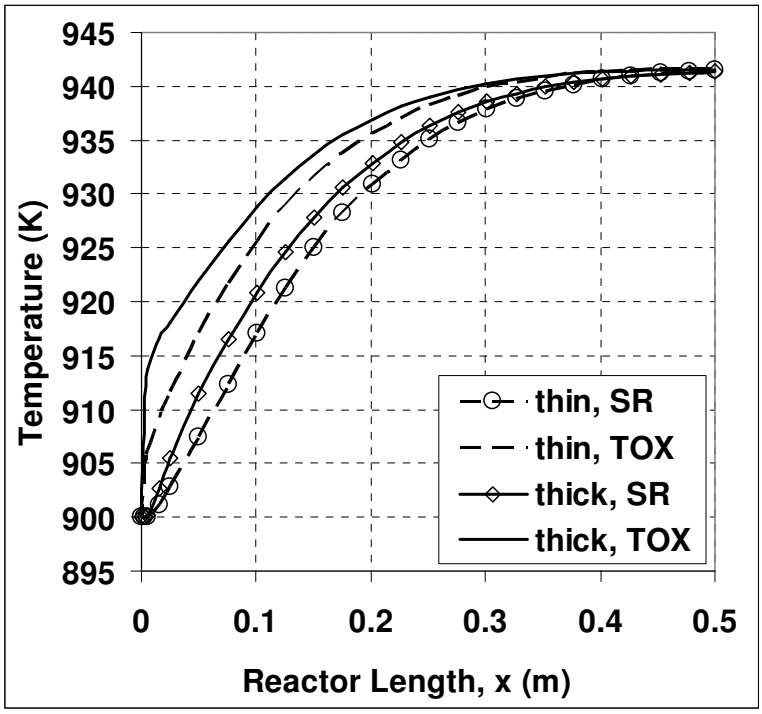

Figure 4.7. Axial temperature profiles of channel centerlines for both thickness cases

From Figures 4.6 and 4.7, it can be seen that the temperature profile of the combustion channel is smoother in the thin case, while in the thick case, the temperature rises up to 915 K steeply before starting to increase smoothly. The explanation of this was discussed when Figure 4.5 was considered. The reason why the jump is not only 10 K as in the base case but 15 K, i.e. greater than base case, is the increased heat transfer resistance of the wall. Increased resistance prevents easy transfer of generated heat both transversely and axially through the wall so more heat is trapped in the combustion channel, not carried transversely to the endothermic reaction location, resulting in higher temperatures in the channel. As a consequence, combustion rate becomes higher and gas temperature increases. This is also the reason why the channel centerline temperatures of thick case are higher than those of corresponding channels of the thin case everywhere along the reactor (Figure 4.7). In addition, the temperature in the centerline of the reforming channel is always lower than that of the combustion channel for both cases, which is due the fact that the combustion side is the exothermic side and the flow in the reforming channel is much faster.

The negative effect of the resistance accompanying increasing wall thickness can also be observed in Figure 4.8, which illustrates the temperature differences between channel centerlines for the base case and the two wall thicknesses. In the thick case, the difference reaches a maximum of 15 K, but this value is below 10 K in the thin case.

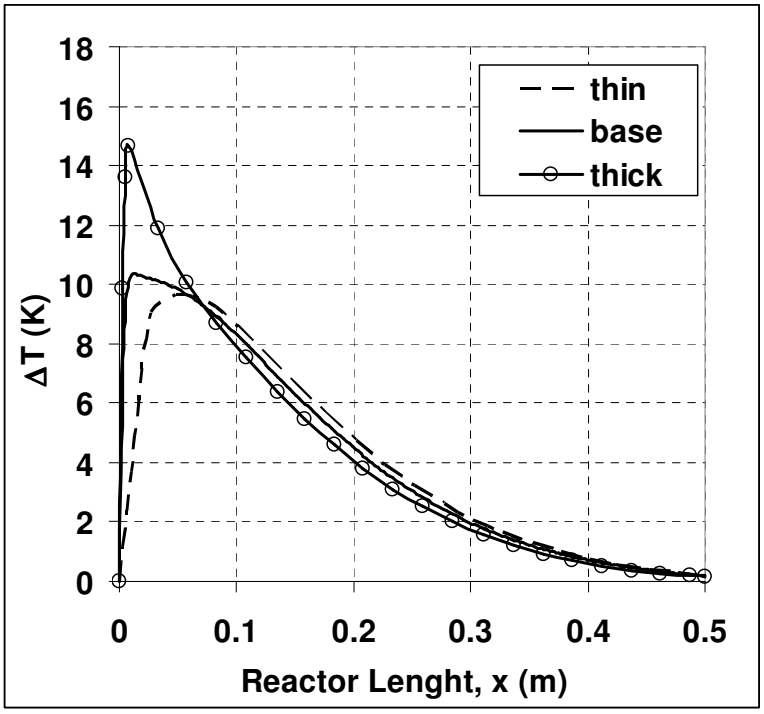

Figure 4.8. Axial temperature difference profiles between centerlines of combustion and reforming channels for base case and both thickness cases

The peak of 15 K of the thick case is also observable in Figure 4.6(b). The base case, which has a wall thickness between the two thickness cases, shows a trend that is in between the plots of the "thin" and "thick" cases.

It was expected that the temperature difference of the thicker cases would always be higher than that of thinner cases everywhere along the reactor. The difference is larger only at the entrance region of the reactor for the thick case. After 0.08 m axially downstream the reactor, the thin wall starts exhibiting higher temperature differences.

The gas streams of both channels exit the reactor at the same temperature, regardless of wall thickness. However, the temperature difference that must be overcome at the

beginning is 1.6 times greater in thick case. So it is only natural that the temperature difference between channel centerlines of the thick case diminishes faster than that of thin case. Therefore, moving downstream on the reactor axis, one would observe the difference being higher in thin case after x = 0.08, but not more than 0.5 K. At the entrance section, this value reaches a maximum of 4.34 K in favor of the thick case. The driving force that builds up across the channels with thicker wall is much greater than that of thinner walls because of reasons described for Figure 4.7. Similarly, the same argument holds for the transverse driving force in the case of thicker walls (Figure 4.9). Eventually, this built up force overcomes the negative effect of resistance; therefore transverse heat transfer in the thick case is easier at downstream sections of the reactor. This is why, after the entrance region, the temperature difference between channel centerlines is leveled out more easily in thick case and the temperature difference of the thin case is higher than thick case.

Temperature differences between the combustion and reforming sides of the wall along the reactor axis for both thick and thin cases are shown in Figure 4.9. A larger temperature difference between the two sides of the wall is observed in thick case everywhere along the reactor which reaches a maximum of 0.375 K. For the thin case though, the corresponding maximum does not exceed 0.08 K (Figure 4.9 (a) and (b)). This is expected and consistent with increased heat transport resistance across the wall.

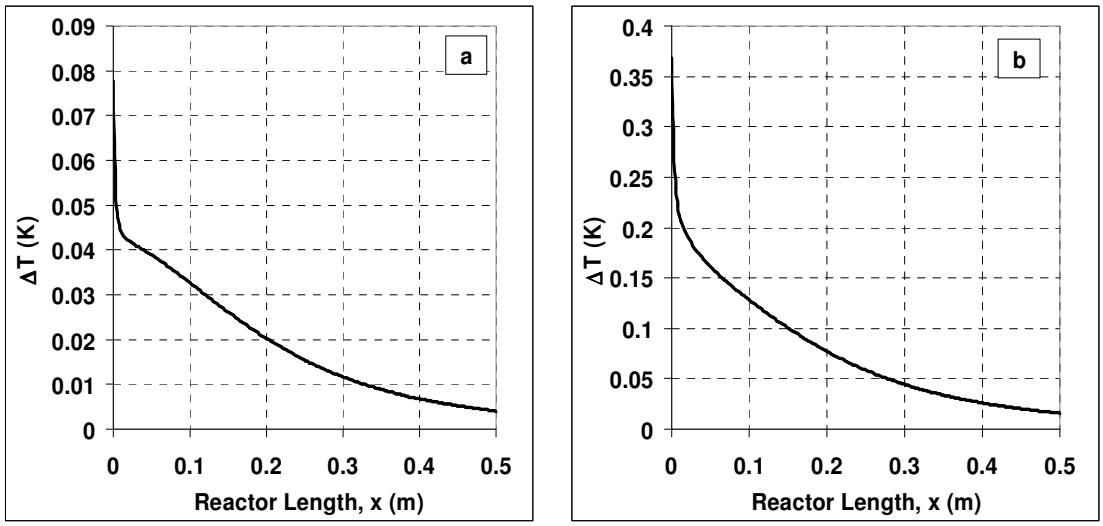

Figure 4.9. Axial temperature difference profiles between the combustion and reforming sides of the wall for (a) thin case, δ_s = 1 mm and (b) thick case, δ_s = 4 mm

In Figure 4.10, the wall center temperature along the axis of the reactor is plotted for the base case and the two thickness cases. The initial wall temperature is observed to be 906 K for thin case, while for the thick case, the wall temperature at the initial condition $x = 0$ is 915 K, and the base case fits in between the two with 910 K. Since there is no significant heat production in the reactor at $x = 0$, these temperatures being higher than the initially assigned gas temperature values is due to the axial heat conduction through the wall that transports heat from downstream sections. However, with a thicker wall not only transverse but also axial heat conduction would be more problematic. Therefore it was expected that the wall temperatures of the thin case would be higher than thick case. But as Figure 4.7 illustrates, temperatures of both the channels in thick wall case are higher than thin case, especially at reactor entrance. Higher channel temperatures compensate for low heat transfer rate of the thick wall and result in higher wall temperatures.

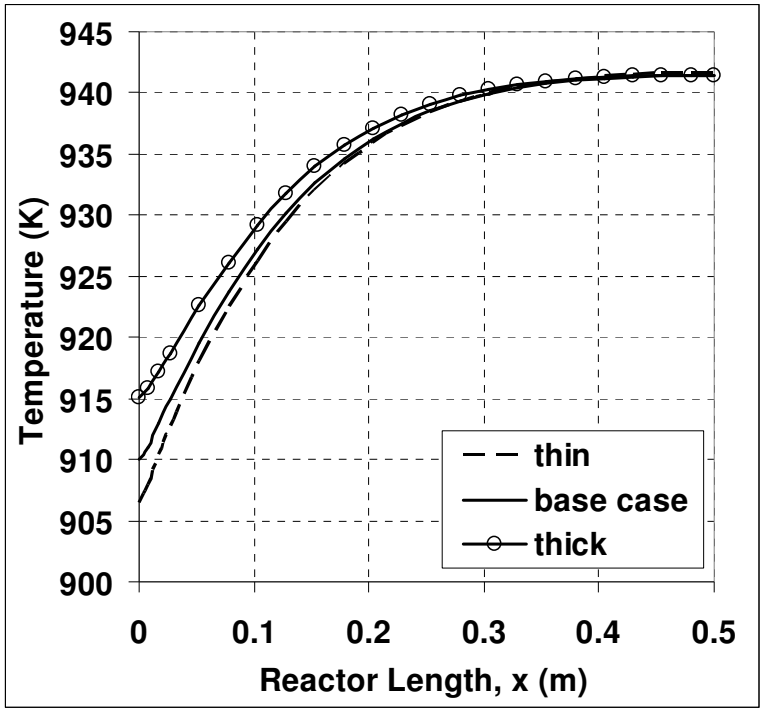

Figure 4.10. Axial temperature profiles of wall center for base case and both thicknesses

Although the highest temperature is 941 K in both cases, same as the base case, the lowest temperatures in thin and thick cases are 881 K and 884.5 K, respectively, which place 882.5 K of the base case in between, as expected. In all three cases, location of the lowest temperature recorded is the beginning of the reforming catalyst layer (Figure 4.11).

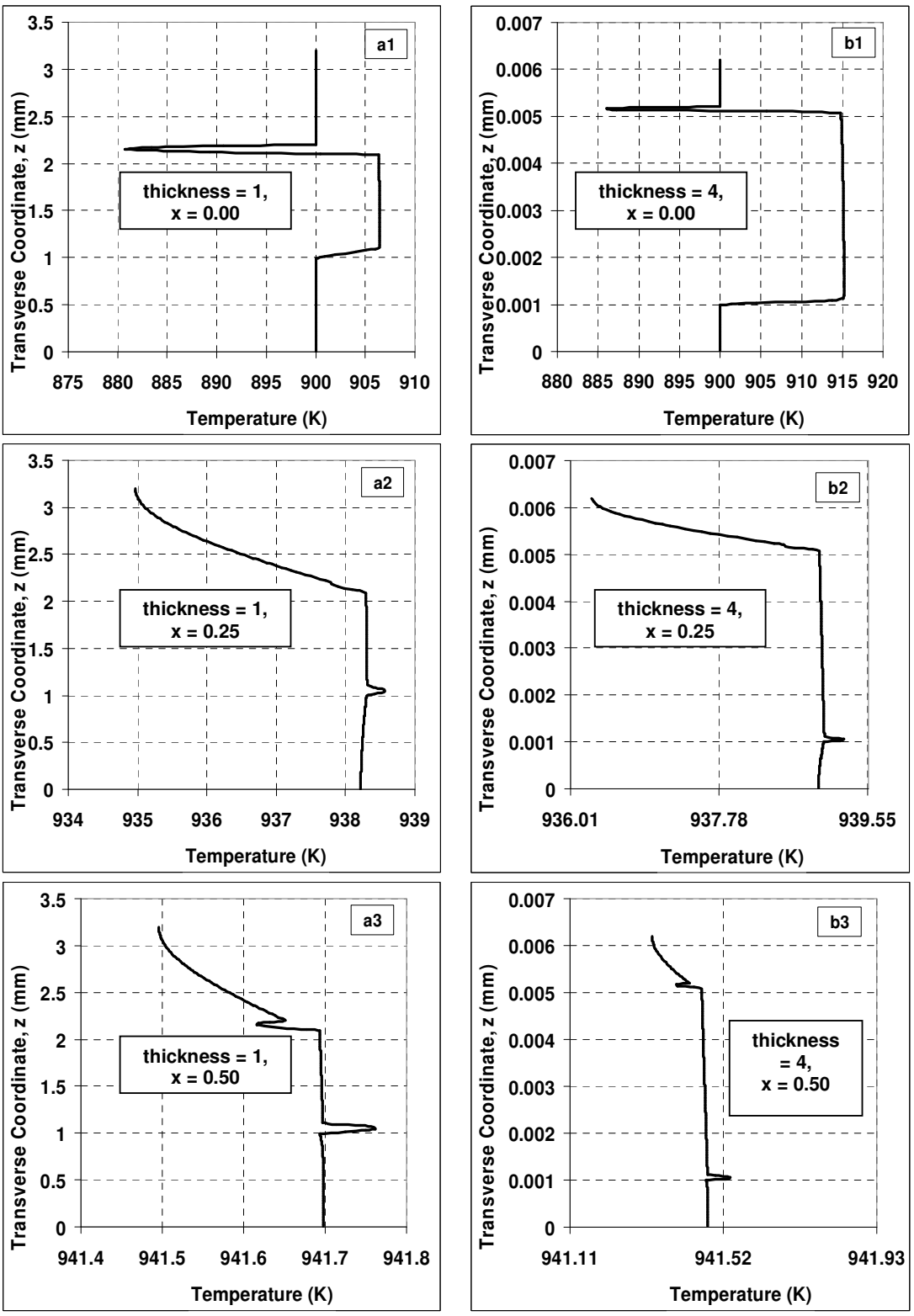

Figure 4.11. Transverse temperature profiles for thickness cases at various axial locations

Figure 4.11 presents transverse temperature profiles at the entrance, the middle and at the end of the reactor for the two thickness cases. It can be seen from Figures 4.11(a1) to (a3) for the thin case and from Figures 4.11(b1) to (b3) for the thick case that the transverse temperature discrepancies, which are 7.5 K and 15 K respectively, disappear towards the end of the reactor and a uniform transverse temperature profile is obtained. A similar trend was also observed for the base case. It can also be said that the temperature profiles at various axial locations of both cases behave just like their base case counterpart, which were discussed in detail with Figures 4.1 and 4.4. Furthermore, Figure 4.11 shows that the efficient performance of CPR in axial and transverse heat transfer is not affected significantly, even if the thickness of the wall is quadrupled.

The conversions of methane and ethanol in thin case are 86.6% and 76.6%, respectively. The corresponding conversions for the thick case are 86.9% and 76.6%. The only difference between the two cases and the base case is the slight increase in methane conversion in the thick case, which is due to increased channel temperatures.

4.1.3. Influence of Wall Material

The thermal conductivity of the wall is also an important design parameter, since it influences heat communication between channels as well as along the reactor. Calculations presented so far were based on a typical metallic wall thermal conductivity. Wall material was selected as steel containing 6% carbon, UNS G10060. The average thermal conductivity of this material in the temperature range of the base case is 38 W/m.K.

In this section, reactor behavior is studied for two cases where the wall thermal conductivity is 15 times lower than the base case or 8.4 times higher, keeping everything else constant. These two cases consider an overall difference of 120 folds between their thermal conductivities; therefore a comparative study between the highest and lowest will bring more insight into the analysis than comparing base case with any of the latter two.

Wall thermal conductivity is changed by changing the wall material. Fused silica, which has a commercial name of Corning 7940, was selected as the low thermal conductivity material with an average thermal conductivity of 2.62 W/m.K in the operating

temperature range. Fused quartz and fused silica are types of glass containing mainly silica in amorphous (non-crystalline) form.

For the material with high thermal conductivity, a copper alloy, UNS C11000, was chosen. This alloy consists of minimum 99% Cu and has an average thermal conductivity of 317 W/m.K in the operating temperature range.

For the sake of simplicity, from here on Corning 7940 and UNS C11000 will be referred to as "silica" and "alloy", respectively. Figure 4.12 presents channel centerline temperature profiles along the reactor for both sides for the silica, i.e. Corning 7940 used as wall material, and for the copper alloy, i.e. UNS C11000 used as wall material.

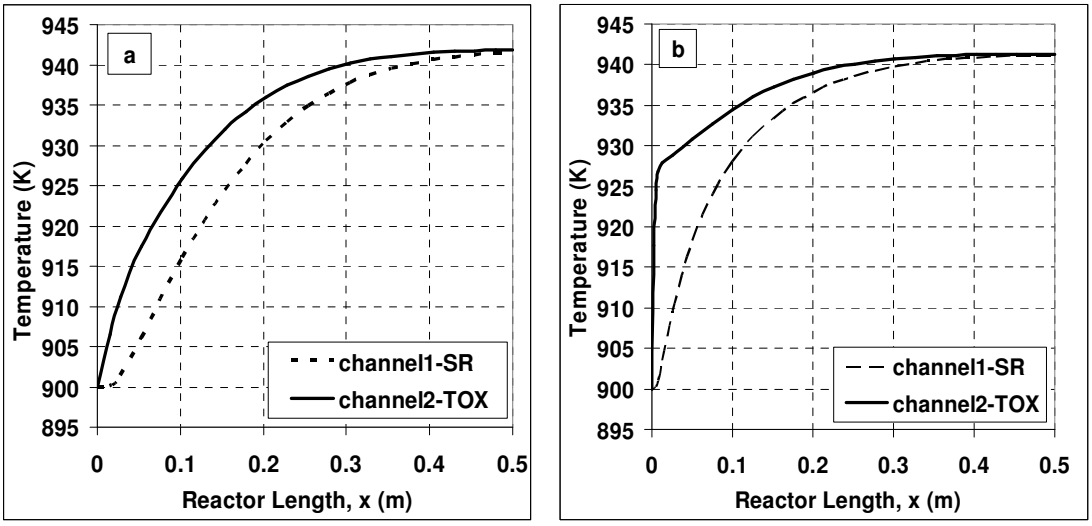

Figure 4.12. Axial temperature profiles of channel centerlines for (a) silica and (b) alloy

Significant transverse temperature differences were expected to appear in Figure 4.12(a), since the thermal conductivity of the wall would not be efficient enough to transport the heat generated by combustion transversely to the endothermic reaction location; thus, the generated heat would be trapped in the combustion channel increasing the temperature of its contents; as a consequence, combustion rate would be higher, increasing gas temperatures everywhere. However, the axial temperature distribution of its combustion channel turned out to be smoother than both the base case and the copper alloy wall (Figures 4.6 and 4.12(b)).

The two cases of low and high thermal conductivity are presented together in Figure 4.13 for easier comparison. The endothermic channel temperature plot for the alloy wall coincides with the exothermic channel plot for the silica wall, which clearly shows that there is a significant difference between the axial temperature profiles of the two cases.

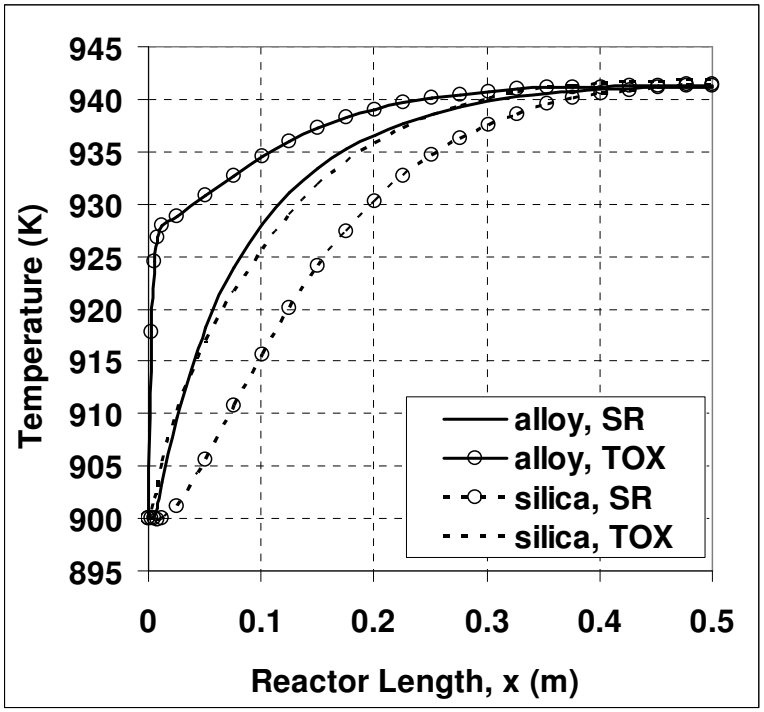

Figure 4.13. Axial temperature profiles of channel centerlines for silica and alloy walls

The axial temperature distribution of the combustion channel is much less smooth in Figure 4.12(b); the jump at the entrance is more prominent, and the linear temperature profile at the entrance of the reforming channel is now less distinct when compared with the base case and silica case (Figures 4.5 and 4.12(a)). In addition, the temperature in the centerline of the reforming channel is always lower than that of the combustion channel for both cases, which is logical since the combustion channel is the heat source and the flowrate in the reforming channel is higher compared to the combustion channel.

The expectations regarding the axial channel centerline temperature profiles of the wall material cases were not met, so previously analyzed cases are taken into consideration in the hopes that they will provide further insight to the situation. When the channel centerline temperature plots of silica and thin wall cases (Figures 4.12 (a) and 4.6 (b)) are

compared, one can observe that they essentially behave the same. A similar argument is also valid for the alloy and thick wall cases (Figures 4.12b and 4.6(a)). Normally, low thermal conductivity and thicker wall cases would be expected to behave similarly, as the resistance to heat transfer increases in both cases; but instead, the low conductivity wall gives results similar to the thin wall case and the same applies to high conductivity wall and thick wall cases.

It is apparent that something else other than the resistance to transverse heat conduction should be considered. In fact, examining the transverse temperature profiles at various axial locations, especially at $x = 0$ and $x = 0.01$, and the axial temperature profiles of wall centerlines for different cases sheds some light on the problem. Upon reconsideration of Figures 4.1(a), 4.3 and 4.10, and comparing them with Figures 4.16 and 4.18(b1); the importance of axial heat conduction through the wall can be noticed. In the base case, wall temperatures higher than the inlet gas streams at the reactor entrance are a result of axial heat conduction, as discussed with Figure 4.1. Here, under steady-state operation, it is logical to have the alloy wall at temperatures higher than the silica wall at the entrance of the reactor (Figure 4.16), because the alloy with its better thermal conductivity can transfer heat from downstream sections of the reactor more easily than silica. The heat transferred in this way heats the entrance sections of the channels, causing their temperatures to increase, as shown in Figure 4.13. Just like the results of increased resistance with increased thickness, the rise in the temperatures increases the rate of the exothermic reaction, causing more heat production and higher temperatures, like the snowball effect, which continues until a balance between heat generation and consumption is reached. This is how the initial peak in the temperature profile of the combustion channel centerline of the alloy is formed; the temperatures increase very steeply in a very short distance. In the two wall-thickness cases, the cause of the initial “heating up-increasing temperatures-increasing reaction rate-heating up” cycle was the heat trapped in the combustion channel due to increased resistance, now in the wall-material cases the cause is the heat brought from the exit of the reactor through the wall. Just like the thicker wall with greater resistance having a more significant influence, the material with greater thermal conductivity also has a greater effect. Two different parameters affect the system by two different mechanisms, but the observed results are essentially the same.

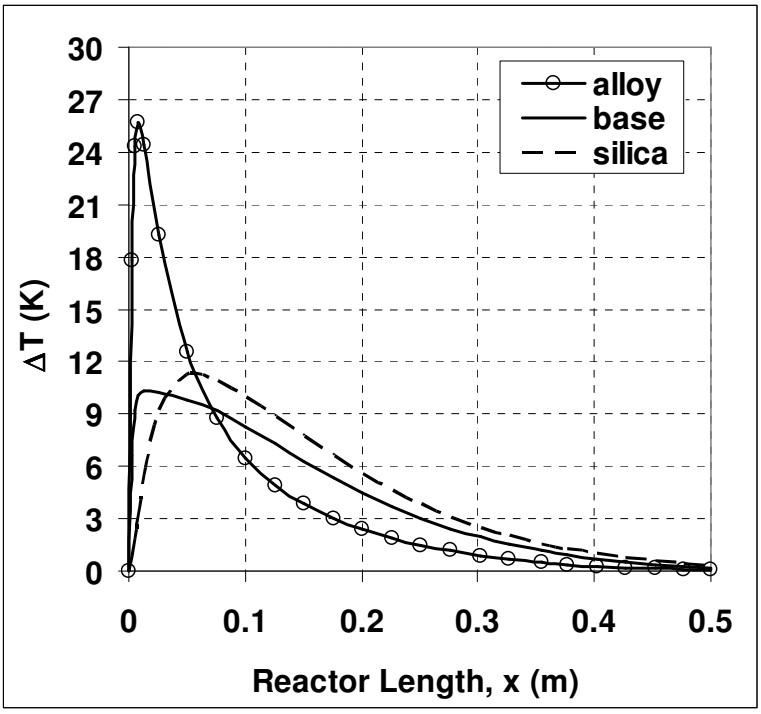

Figure 4.14. Axial temperature difference profiles between channel centerlines of combustion and reforming channels for base case and the two wall-material cases

Temperature differences between channel centerlines along the reactor axis for base, silica and alloy cases are shown in Figure 4.14. The smaller differences expected for the alloy case with its higher thermal conductivity were only observed at the entrance of the reactor.

The same phenomenon is experienced here again, i.e. the alloy shows the same trend as the thicker wall (Figure 4.8). What is observed in Figure 4.14 is explained by the sharp peak of the temperature difference at the entrance building up a driving force which then overcomes the resistance and facilitates transverse heat conduction at the downstream parts of the reactor. In the former case, the peak is generated by the heat trapped in the combustion channel due to greater resistance of the thicker wall; in the latter, it is caused by the heat brought by the conduction enhancing solid wall. The copper alloy with better thermal conductivity enables higher temperatures than silica at the entrance of the reactor, as explained before, yielding a higher temperature difference between the exothermic and endothermic channels due to the snowball effect on the former.

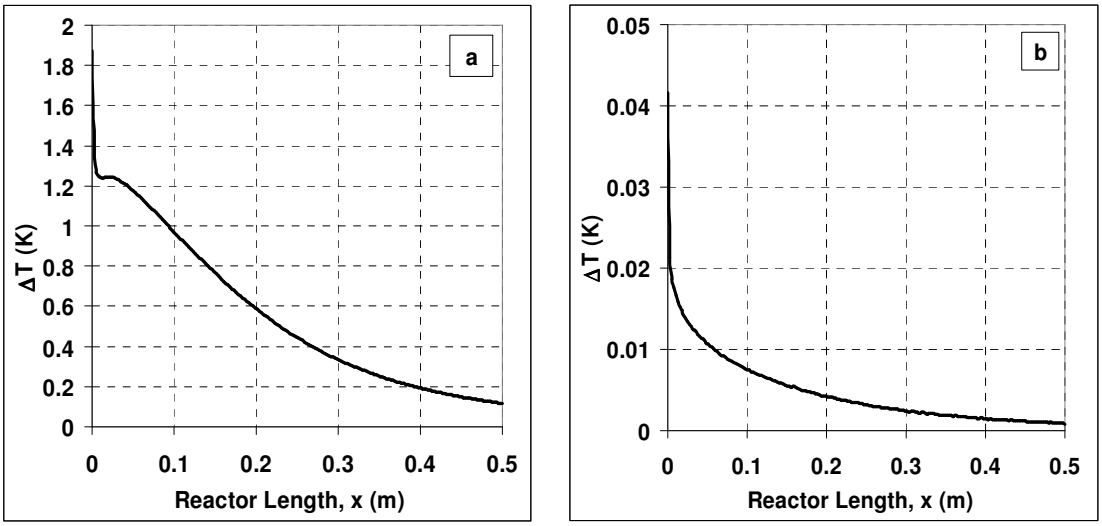

Figure 4.15. Axial temperature difference profiles between the combustion and reforming sides of the wall for (a) silica and (b) alloy cases

Temperature differences between the combustion and reforming sides of the wall along the reactor axis for both silica and alloy cases are shown in Figure 4.15. It is important to note that the solid wall is investigated in such a way as to isolate it from the rest of the system. The channels and their transverse and axial temperature gradients do not have an effect on the transverse temperature of the solid wall because the thickness is very small and the wall has no direct contact with the flowing gas mixture. It is covered with catalyst layers on both sides, and therefore, experiences only the major changes that affect the temperature trends of the system directly. In Figure 4.15(a), silica has higher transverse gradients than the alloy, resulting from pure resistance due to the decreased thermal conductivity. A larger temperature difference between the two sides of the wall is observed in the case of silica, reaching a maximum of 1.9 K. The corresponding maximum for the alloy hardly exceeds 0.04 K (Figure 4.15(b)).

The wall center temperature along the axis of the reactor is plotted for both cases in Figure 4.16. The initial temperature of the wall is observed to be 900 K for silica, as expected, while the wall temperature at $x = 0$ is almost 928 K for the alloy.

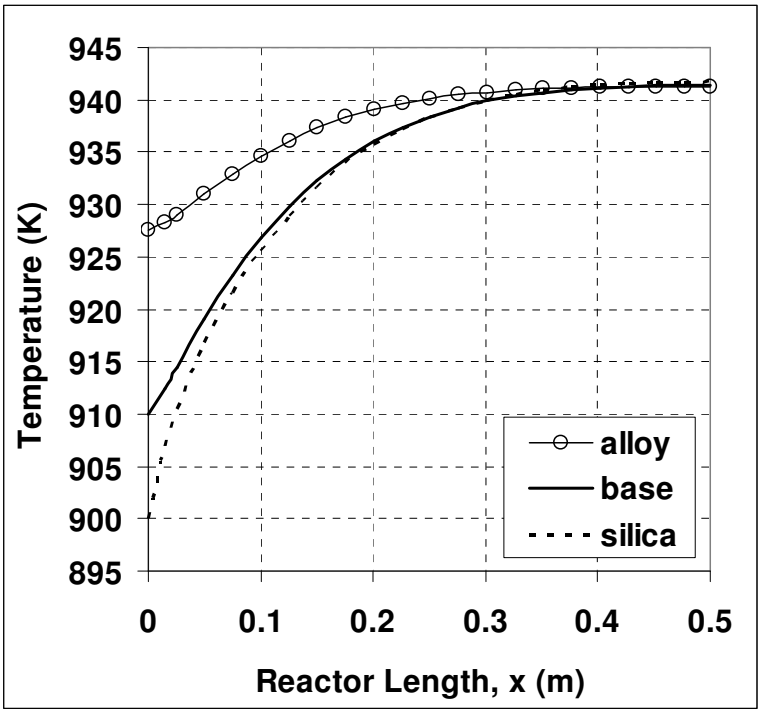

Figure 4.16. Axial profiles of wall center temperatures for the base, silica and alloy cases

In Figure 4.1 it was explained that the wall has much higher temperatures than channels at $x = 0$ because of axial heat conduction from the hotter downstream section of the reactor. Furthermore, in relation to Figure 4.10, it was explained that the initial wall temperature of the thick case is higher than that of the thin case although its resistance to both axial and transverse heat conduction is greater.

The situation regarding the effect of wall material is not so complicated. The material with the highest conductivity has the highest temperature at the reactor entrance. It is easier to transport the heat from downstream sections of the reactor with copper than silica. The transport mechanism is axial heat conduction through the solid wall, in a direction opposite to gas flow. It is as if the system is constantly promoting itself, the wall has high temperatures at the entrance so the exothermic reaction is faster, generating more heat and causing the downstream sections to have even higher temperatures. The driving force formed between the exit and the entrance of the reactor allows heat to be conducted to the upstream sections through the wall, increasing the wall temperatures at the entrance. This is continued until a balance is reached between heat generation and consumption.

The temperature difference between the channel center and the wall side of reforming and combustion channels for both cases is plotted in Figure 4.17(a); here it can be observed that initially the wall side of the reforming channel is 1 K colder that the channel center. This is the endothermic reaction consuming the sensible heat in the reaction mixture, and then the wall side heats up through the entrance region. After that, the channel center starts to gain in, and the difference approaches to zero towards the end of the reactor. Similar behavior cannot be observed when alloy is used as wall material (Figure 4.17(b)); because of its higher conductivity, the wall side immediately starts at a 27.5 K higher temperature.

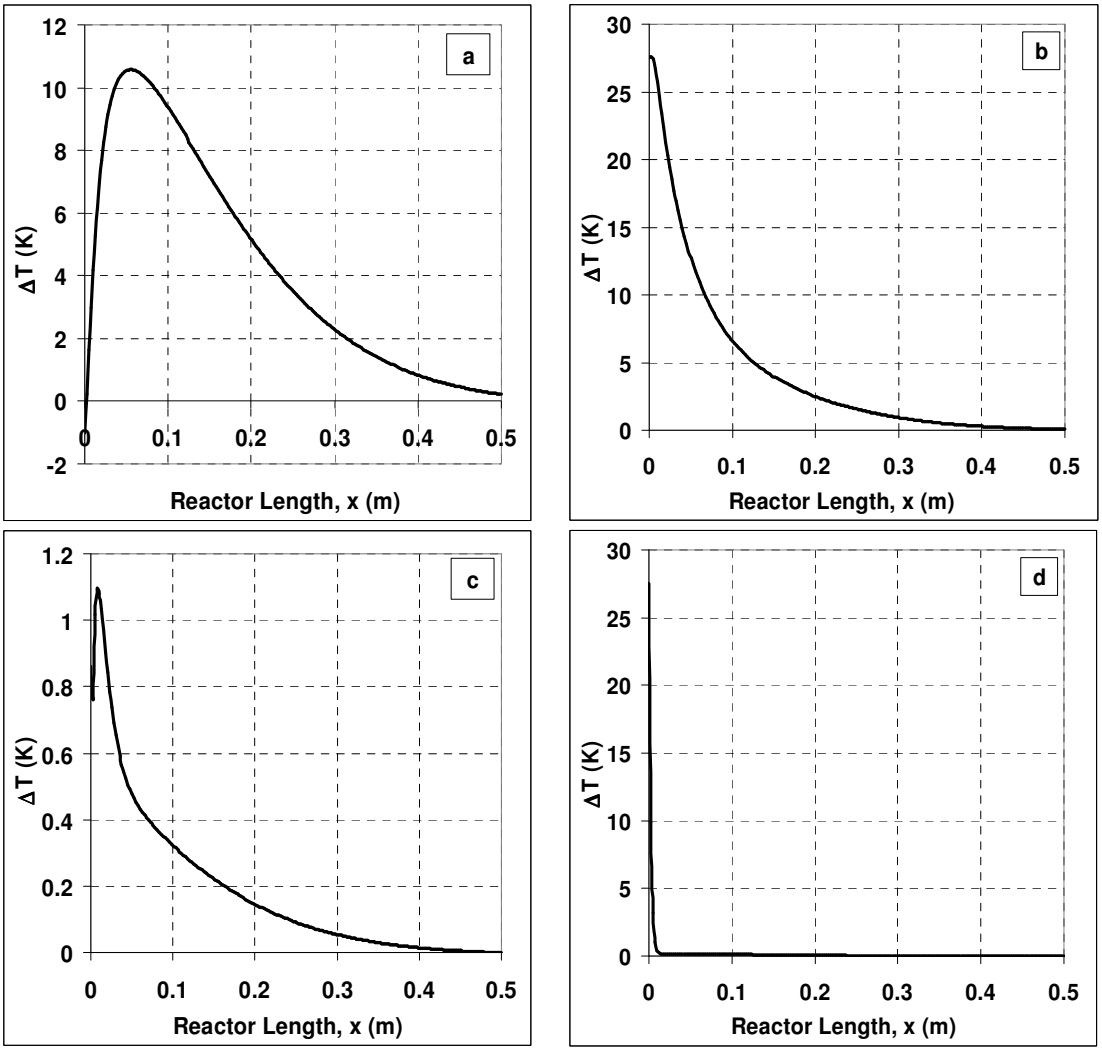

Figure 4.17. Axial temperature difference profiles between channel centerlines and the wall sides of channels for both material cases; (a) channel 1-silica, (b) channel 1-alloy,(c) channel 2-silica, (d) channel 2-alloy

Considering the combustion side for the two cases in Figures 4.17(c) and (d), analogous behavior is observed but, since this is the heat generation side, the decrease in temperature differences is steeper.

Disregarding the first 0.1 m of the reactor, i.e. the entrance region, it can be seen from Figures 4.14, 4.15 and 4.17 that the most significant temperature difference observed in the silica case (10 K) is between channel centerlines (Figure 4.14) and between gas phase channel centerline and wall side of the channel of reforming side (Figure 4.17(a)). Situation is similar in alloy case also, with a maximum difference of 6 K. The value of the difference being higher in silica was expected. But it was expected to have the most significant temperature difference between channel centerlines in low conductivity case and between gas phase and channel wall of the reforming side in the other.

Figure 4.18 presents transverse temperature profiles along the reactor for both wall materials; Figures 4.18(a1) to (a3) display the silica case and Figures 4.18(b1) to (b3) the alloy case. The transverse temperature discrepancies, which are 2 K for silica and 28 K for alloy walls, disappear near the reactor exit and the transverse temperature profile becomes uniform. Furthermore, the silica plots in Figure 4.18 show that the temperature drops by almost 4 K from the hot side to the cold side due to wall resistance, but this difference is merely 0.1 K at reactor exit.

When silica is used as wall material, ethanol reaches 76.6% conversion and methane 86.7% conversion, which are the same as the base case values. When the alloy wall is used, ethanol and methane reach 76.7% and 87.4% conversion values, respectively. The slight increases in the conversion values are probably due to efficient heat transfer provided by the high thermal conductivity of the alloy with respect to silica.

Although the highest temperature is 941 K in both cases, same as in the base case, the lowest temperatures in silica case and alloy cases are 878 K and 890 K, respectively. These values place 882.5 K of the base case in between, as expected. In all three cases, the location of the lowest temperature recorded is the same, the beginning of the reforming catalyst layer.

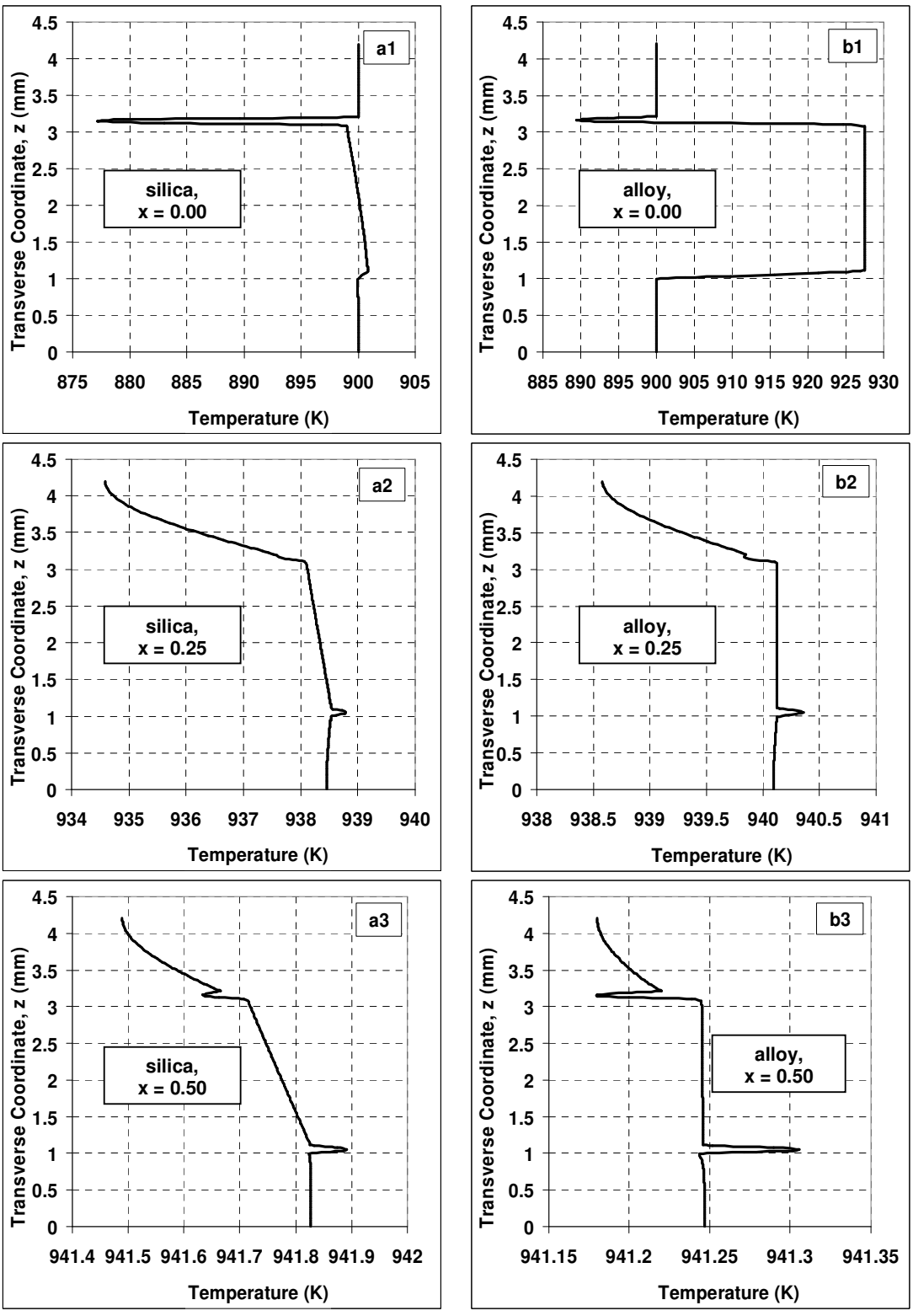

Figure 4.18. Transverse temperature profiles for wall material at various axial locations

4.1.4. Influence of Water-to-Ethanol Ratio

The relation between heat generation and heat consumption is important for efficient performance of the CPR. The water-to-ethanol ratio is related to ethanol steam reforming reaction rate, which in turn affects the rate of heat consumption and thus the temperature distributions throughout the whole system. In order to gain further insight into reactor behavior, the water-to-ethanol ratio has been varied one at a time, keeping all the other parameters constant at their base case values. Two different cases are analyzed in this section, one with excess amount of water and the other with deficient amount of water. The water-to-ethanol ratio for the base case is the stoichiometric amount, i.e. 3.0.

Firstly, a case in which the water-to-ethanol ratio is taken as 6 is studied, every other parameter being kept constant; this case will be referred to as the "excess case". The second case investigated is a water deficient case with a water-to-ethanol ratio of 2, which will be termed as the "deficient case". The axial temperature profiles along the channel centerlines for both cases are plotted in Figure 4.19.

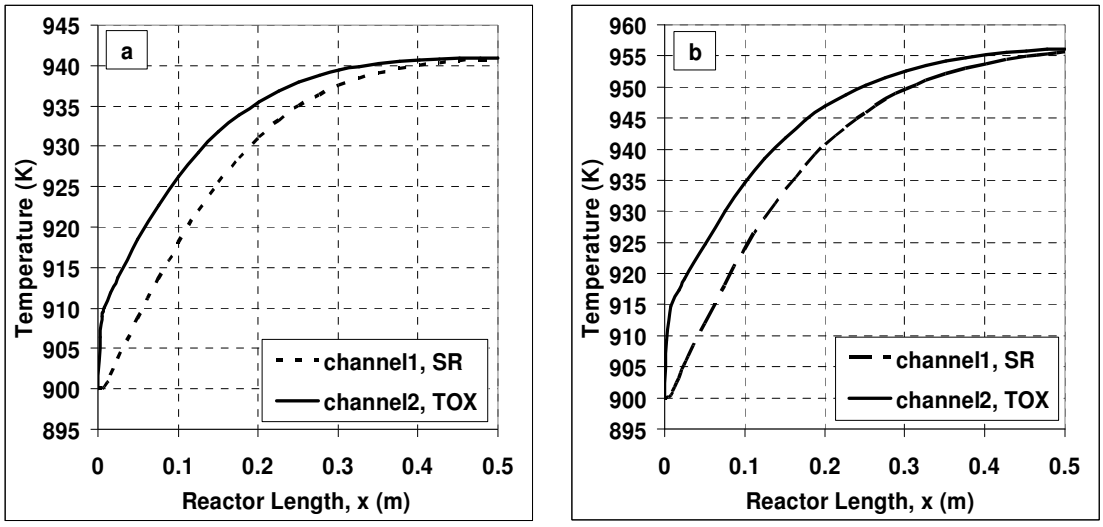

Figure 4.19. Axial temperature profiles of channel centerlines for (a) excess water and (b) deficient water cases

When the plot of the excess water case, Figure 4.19(a), is compared with the same type of graph for the base case, Figure 4.5, it is seen that the two figures are almost the same which means that there is no significant change in heat consumption or generation.

Ethanol conversion is calculated as 77.3% and methane conversion as 86.6%. These values are not very different from the base case (76.6% and 86.7% respectively). Therefore, excess water in the reaction mixture does not seem to have a substantial effect on the rate of the reforming reaction and hence on the rate of combustion.

There may be a few reasons for this behavior. Firstly, the flow in the reforming channel is very fast, and the corresponding residence time may not be sufficient for observing any appreciable effect of excess water. Secondly, the concentration of ethanol in the feed stream is small, and the slight increase in conversion from 76.6% to 77.3% may in fact be a contribution of excess water in shifting the reaction toward the product side, against the well-known mildly inhibitory effect of water on steam reforming kinetics of hydrocarbons (Önsan, 2007; Örücü *et al.*, 2008; Soyal-Baltacıoğlu *et al.*, 2008).

The temperature differences between reforming channels and the differences between combustion channels of the base and excess water cases are plotted in Figure 4.20, in order to find out if there is any difference at all.

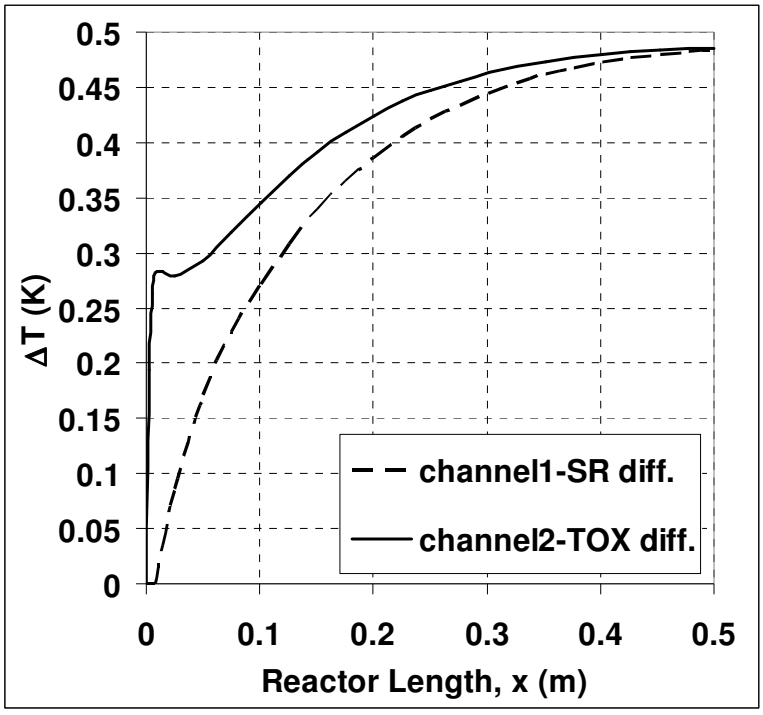

Figure 4.20. Axial temperature difference profiles of the centerlines of reforming channel and centerlines of combustion channel between base case and excess water case

It is apparent from the plots that, either of the base case channel centerline temperature values is always higher than the corresponding channels of the excess case. This discrepancy is caused by the excess water in the reforming channel; the surplus water flowing in the reactor acts as a part of the heat sink with its relatively larger heat capacity, and, unfortunately, all the heat absorbed by the excess water leaves the reactor with it. It actually sweeps away heat which would otherwise be used to heat the reactants and increase the steam reforming rate. At the reactor exit, the temperature difference reaches a maximum of 0.48 K for both channels. The peak at the entrance of the combustion channel temperature difference plot is the same peak that carries the centerline temperatures of the combustion side of the base case (Figure 4.5) and the excess water case (Figure 4.19(a)) sharply from the inlet temperature up to 910 K, and its existence in the difference plot means that the temperature peak in the base case is more effective than that in the excess water case.

Figure 4.21 demonstrates that the temperature differences between the combustion side of the wall and the reforming side of the wall for the base and excess water cases are almost the same, except for the slight difference at the entrance, meaning that there is no significant difference in the driving force of the transverse conductive heat transfer.

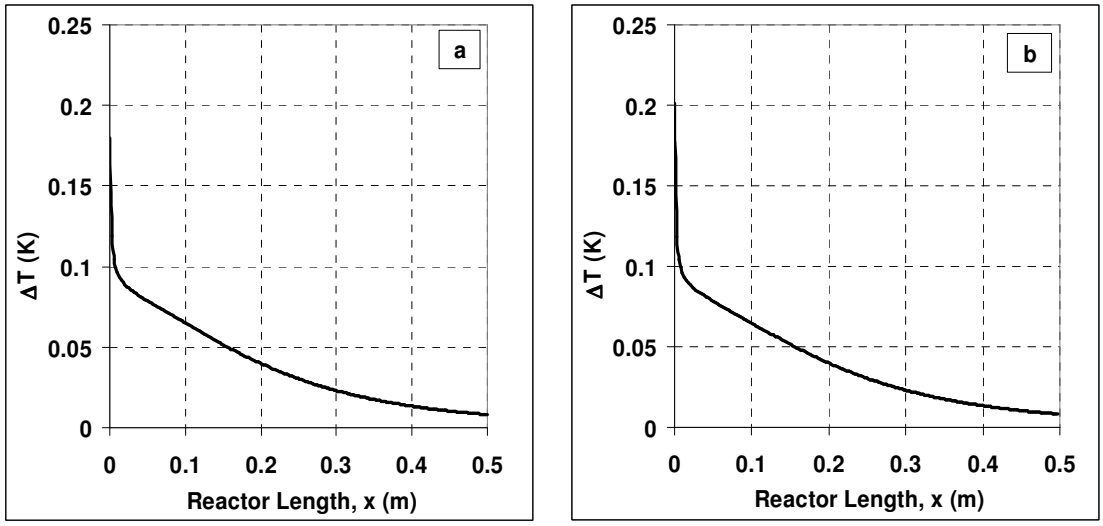

Figure 4.21. Axial temperature difference profiles between the combustion and reforming sides of wall for (a) base case and (b) excess water case

Therefore one can deduce that the rates of heat generation and heat consumption have not changed much, as also seen from the conversion values. Again, the discrepancies in channel centerline temperatures of the two cases arise from excess water sweeping away the sensible heat. At reactor entrance, it is observed that the hot side of the wall in the excess water case is 0.02 K hotter than that of base case, which is probably due to the increased transfer resistance in the reforming channel with the increased amount of water.

Further investigation of the effects of water-to-ethanol ratio involves performing a run with an amount of water less than that required for the reforming reaction. Keeping everything else constant, the water-to-ethanol ratio is now adjusted to 2.0, lower than the stoichiometric value of 3.0 in the base case.

The conversion values calculated for deficient water case are quite different from those of the base case. Ethanol conversion is now much lower, 49.9 % as compared to 76.7%, but methane conversion is somewhat higher, 88.6 % as compared to 86.7%. This is in accordance with expectations, as the rate of the reforming reaction decreases due to insufficient amount of one reactant which becomes rate-limiting; consequently, the heat consumption of reforming channel also decreases. The excess heat generated by methane oxidation is now utilized for heating up the contents of the combustion channel, thus enhancing the exothermic reaction and increasing methane conversion.

The axial temperature profiles of the two channels for deficient case are plotted in Figure 4.19(b). It can easily be noted that the exit temperature of the reactor is now 955 K, higher than both the base case and the excess water case. The centerline of the combustion channel makes a peak up to 915 K at the entrance region, as opposed to the base case, where this value is 910 K, as expected, as the reforming reaction proceeds slowly now and the generated excess heat is utilized to heat up the flowing gas mixtures in the channels.

It is apparent from Figure 4.22 that the base case channel centerline temperatures are always lower than those of the water deficient case, and at reactor exit, this difference reaches a maximum of 15 K for both channels. 15 K is quite large, considering the 0.46 K difference between the excess water and base cases.

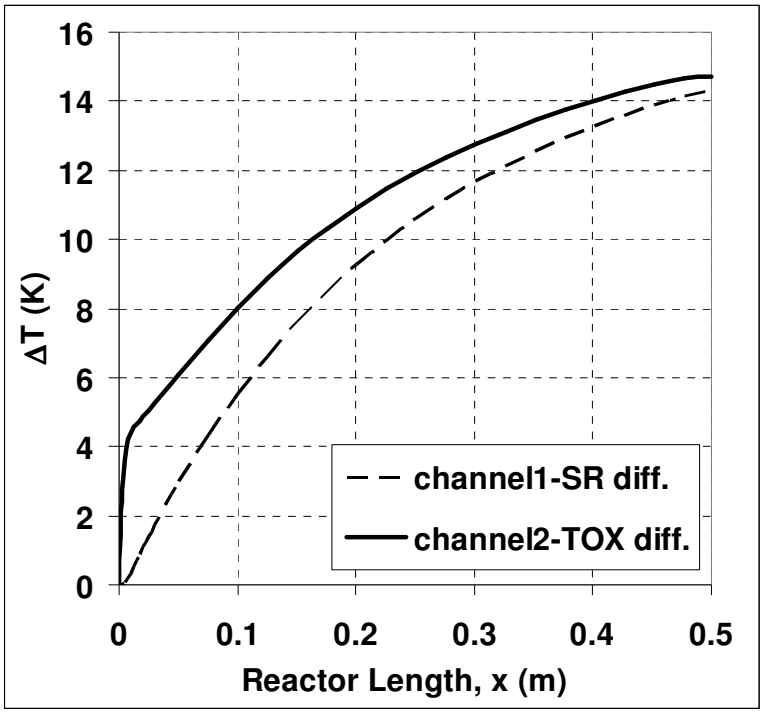

Figure 4.22. Axial temperature difference profiles of the channel centerlines between the base case and water deficient case

Figure 4.23 shows the temperature distributions of wall centers of the three cases. It is observable from the plots that base case and excess case behave almost same, as they do not have differences in terms of reaction rates. Even though the wall material and any other parameter related to the wall are the same for all three cases, the initial wall temperature in the deficient case is higher than the others. This is due to the fact that the temperatures of the deficient case are again higher than the other cases at downstream sections of the reactor. Therefore, the driving force for axial heat conduction is stronger in deficient case, so heat is conducted axially through the metal wall from downstream sections of the reactor to the beginning of the wall, increasing its entrance temperature.

In the excess case, the highest temperature is 941 K and is at the same location as the base case. However, the lowest temperature is 876 K, lower than the inlet temperatures and the lowest value of the base case, 882.5 K. This value and the channel centerline temperatures (Figure 4.20) being lower than the other two cases is due to the increased amount of water in the flowing gas mixture carrying away more sensible heat, as the flow rate of the reforming channel is already very high; but the endothermic reforming reaction

starts consuming sensible heat even at $x = 0$. The combined effects of these two incidents cause the minimum of the excess case to be lower than that of the deficient and even the base case.

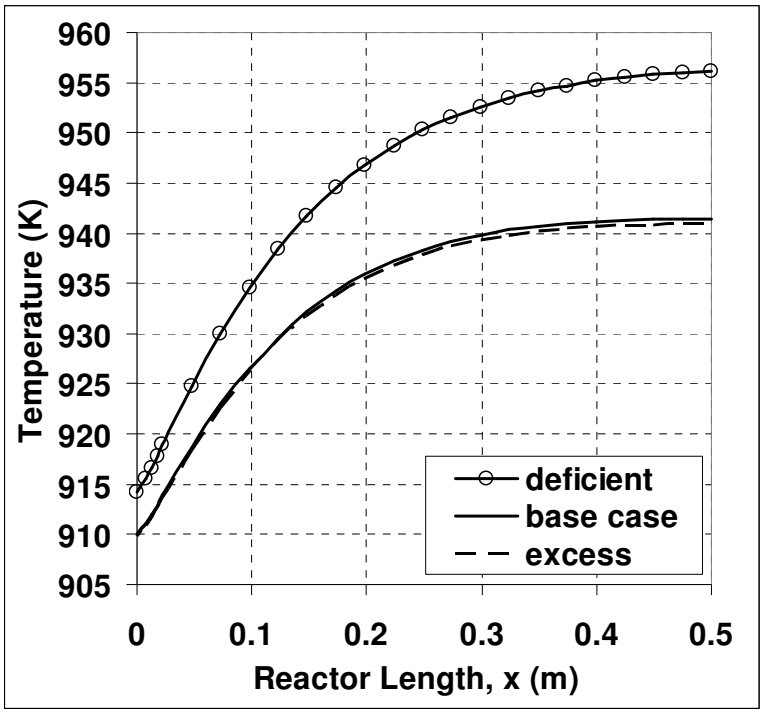

Figure 4.23. Axial temperature profiles of wall center temperatures for base case, excess water and deficient water ratio cases

The temperature minimum and maximum of the deficient case are 886 and 956 K, respectively, which are the highest among the three cases. Due to lack of enough water as a reactant, the rate of steam reforming is slow in the deficient case, so temperatures can not get as low as the other cases, although the maximum and minimum positions are the same.

Figure 4.24 presents transverse temperature profiles along the reactor for both water cases. Figures 4.24(a1) to (a3) display the deficient case and Figures 4.18(b1) to (b3) the excess case. At reactor exit, the transverse temperature discrepancies, which are 15 K and 10 K respectively, disappear and the transverse temperature profile becomes uniform. The reason for the transverse gradients being larger in the deficient case is that there is not enough heat consumption to counter catalytic combustion, so the generated heat increases the temperatures in the combustion side more than it does in the excess case.

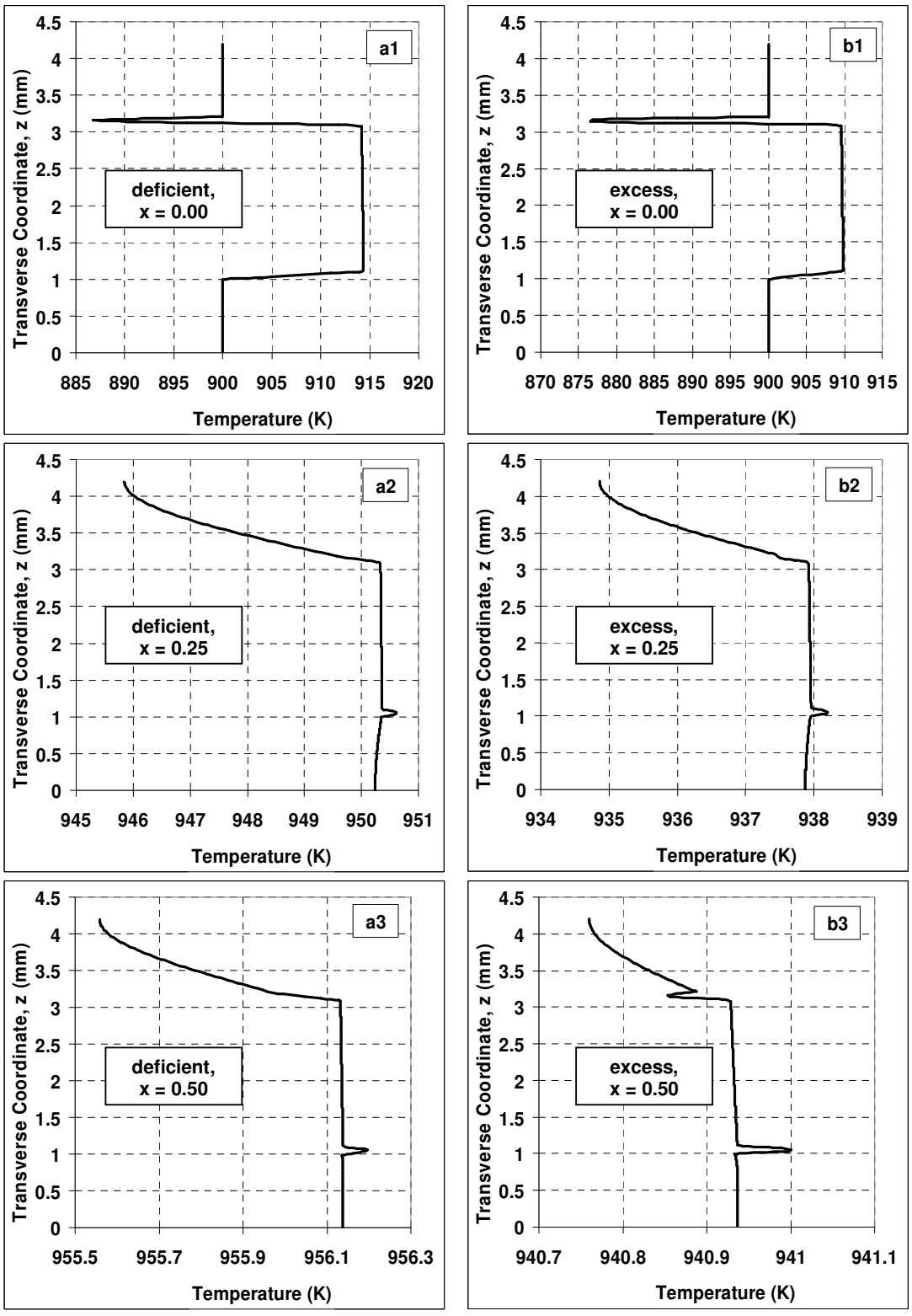

Figure 4.24. Transverse temperature profiles for two water ratios at various axial locations

4.1.5. Influence of Oxygen-to-Methane Ratio

The effect of the oxygen-to-methane ratio is studied by comparing three cases. The first case is one with an oxygen-to-methane ratio of 1.0 and is referred to as the "poor case". The base case has an oxygen-to-methane ratio equaling the stoichiometric amount, i.e. 2.0 (Equation 4.3). The third case is one with an excess amount of oxygen, an oxygen-to-methane ratio twice the stoichiometric amount, and is referred to as the "rich case".

$$CH_4 + 2\ O_2 \rightarrow CO_2 + 2\ H_2O \qquad \Delta H = -802\ \text{kJ/mol} \quad (2.4)$$

Figures 4.25(a) and (b) show the changes in reactor behavior in terms of axial channel centerline temperature profiles when the oxygen-to-methane ratio in the combustion channel is varied. Figure 4.26 presents both cases for easier comparison, while plots of the base case are given in Figure 4.5.

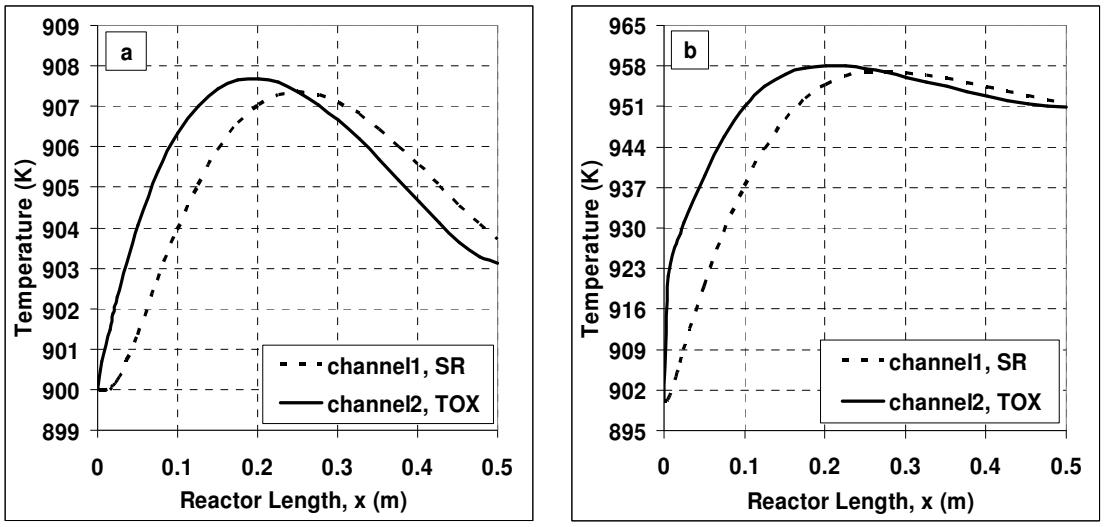

Figure 4.25. Axial temperature profiles of channel centerlines for (a) oxygen-poor and (b) rich case

The axial temperature profile of the wall center is given in Figure 4.27. As the oxygen ratio increases from poor to rich, so does the initial temperature of the wall. It is at the specified inlet temperature only in the poor case. The entire reactor has higher temperatures in richer cases, therefore axial conduction through the wall from hot sections to $x = 0$, which is at 900 K, is easier, resulting in higher wall temperatures.

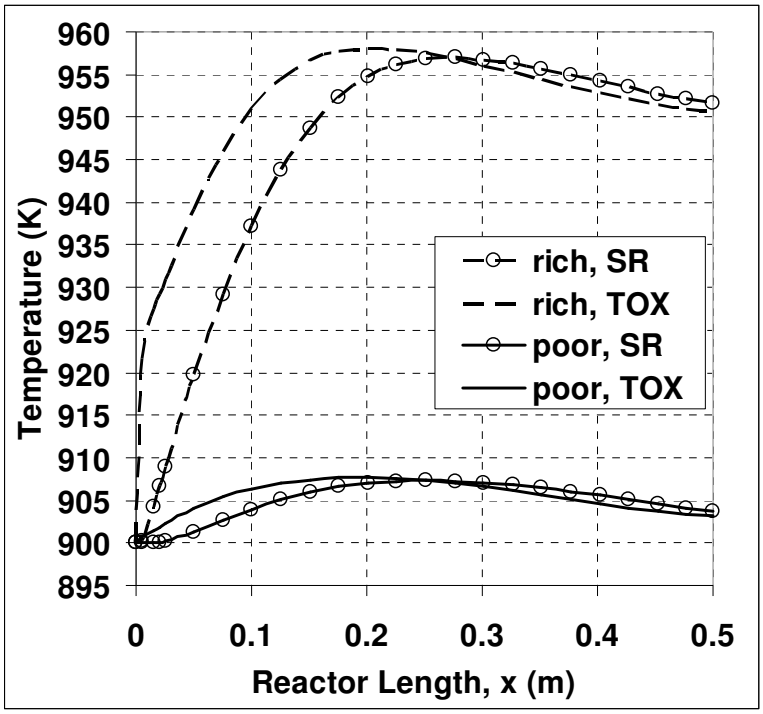

Figure 4.26. Axial temperature profiles of channel centerlines for both oxygen ratio cases

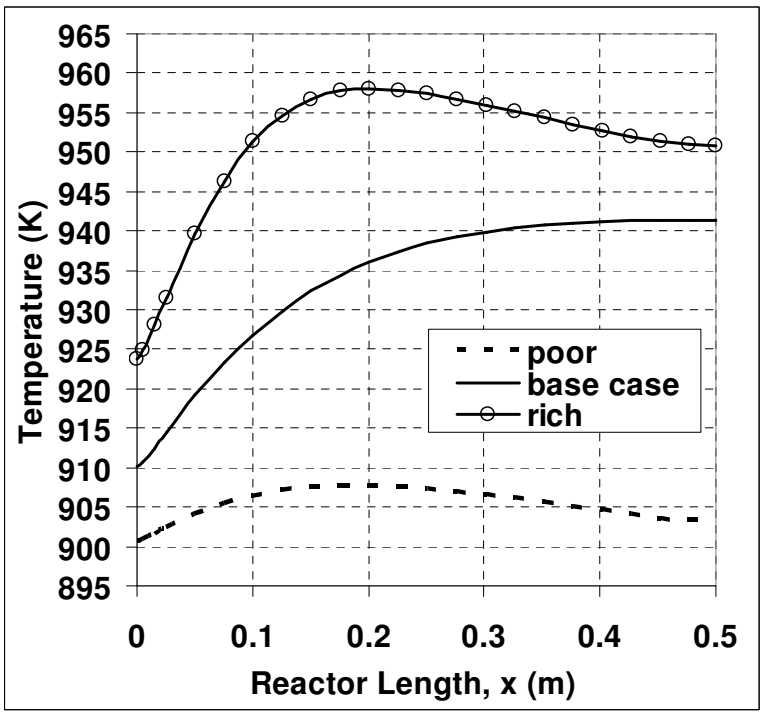

Figure 4.27. Axial temperature profiles of wall centers for base and both oxygen ratio cases

As the oxygen-to-methane ratio decreases from the base case to a lower value, catalytic combustion slows down and a lower methane conversion, 40.44%, is attained as compared to the 86.7% methane conversion in the base case. Consequently, the amount of heat generated is smaller and the temperature at every point along the reactor axis drops compared with the base case (Figures 4.25(a) and 4.27). Ethanol steam reforming rate decreases, and as a result, a slightly lower outlet ethanol conversion of 75% (as compared to 76.6%) is obtained.

The combustion channel starts to cool down after x = 0.18 (Figure 4.25(a)) and, accordingly, a maximum occurs in the temperature profile, i.e. a hot spot develops. Hot spots do not necessarily reach very high temperatures, e.g. here it is only 8 K higher than the inlet temperature; they are only the maximum points on positive temperature gradients. The reforming channel also starts to cool down after x = 0.28 (Figure 4.25(a)) and after this point along the reactor, the temperature of the reforming channel is always higher than that of the combustion channel.

The reason for this unexpected temperature difference is that the heat consumption rate is higher than heat generation rate in this case, especially after x = 0.28. Up to this point, the amount of oxygen flowing in the combustion channel is sufficient enough to keep the exothermic rate up in pace with the endothermic rate with the aid of the slow flowrate in the combustion channel and fast flowrate in the reforming channel. After this point, the heat consumption is larger than heat generation; the system starts to cool down due to fuel depletion in combustion channel resulting in low temperature, which in turn decreases both reaction rates; however, the decrease in the endothermic rate is drastic since it depends more on heat supply. As a result, the decrease rate in the temperature of the gas mixture in the reforming channel (Figures 4.25(a) and 4.26) is not as fast as it would be expected from an ongoing endothermic reaction mixture.

There is a delay between the start of the temperature decrease of the reforming channel and that of combustion channel mainly due to the transverse and axial heat transfer through the wall and channels, i.e. the endothermic reaction makes use of the heat residing in these for a short while. Because of this delay, the temperatures of the reforming channel are higher than those of the combustion channel after x = 0.28 until the reactor exit.

If the reactor were to be longer in the axial direction, an increase in the temperatures would possibly be observed. Such an increase would be caused by the fact that the rate of the endothermic reaction would have slowed down to such little values that the heat produced by combustion could heat up the channels and increase the temperatures and conversion values.

When the oxygen-to-methane ratio increases, the amount of heat generated is higher and exit conversions increase in both channels; ethanol conversion is somewhat higher at 77 % (as compared to 76.6% in the base case) and methane conversion is much higher at 99.6% (as compared to 86.7%). Consequently, the temperature at every point along the reactor increases (Figures 4.25(b) and 4.27). At the same time, a hot spot develops because combustion is faster than the endothermic reaction, heat generation overcomes heat consumption and both streams are heated up. The rise in temperature accelerates the endothermic reaction, which in turn results in an increase in heat consumption so that the temperature drops after $x = 0.18$ for combustion and after $x = 0.28$ for reforming channels. A further result is that after $x = 0.28$ point along the reactor, the temperature of the reforming channel is always higher than that of the combustion channel, but the difference between the profiles is smaller than the difference in Figure 4.25(a).

There is also an initial steep increase from the inlet temperature of 900 K to 923 K in the combustion channel centerline temperature profile of the rich case. This is due to the heat produced by catalytic combustion which heats up the gas mixture before the temperature is high enough to overcome transverse resistances and allow heat utilization by reforming. The jump is greater than that in the base case (Figure 4.5) because of the faster reaction rate caused by rich oxygen concentration.

The reason for the small difference in ethanol conversion is that the flowrate of the reforming channel is very high, resulting in low residence times for ethanol, i.e. the reactant does not spend enough time in the reactor to be affected significantly from these temperature changes. Moreover, the concentration of ethanol as reactant in the gas stream of the reforming channel is very low, so ethanol reaches a relatively high conversion even at low temperatures.

The effects of increasing the oxygen-to-methane ratio on the temperatures of the combustion side of the wall are presented in Figure 4.28. The trend is as expected, increasing the ratio starting from 1, then to 2 in the base case and finally to 4 increases the maximum of the axial temperature profile from 908 K to 941 K and then to 958 K, respectively.

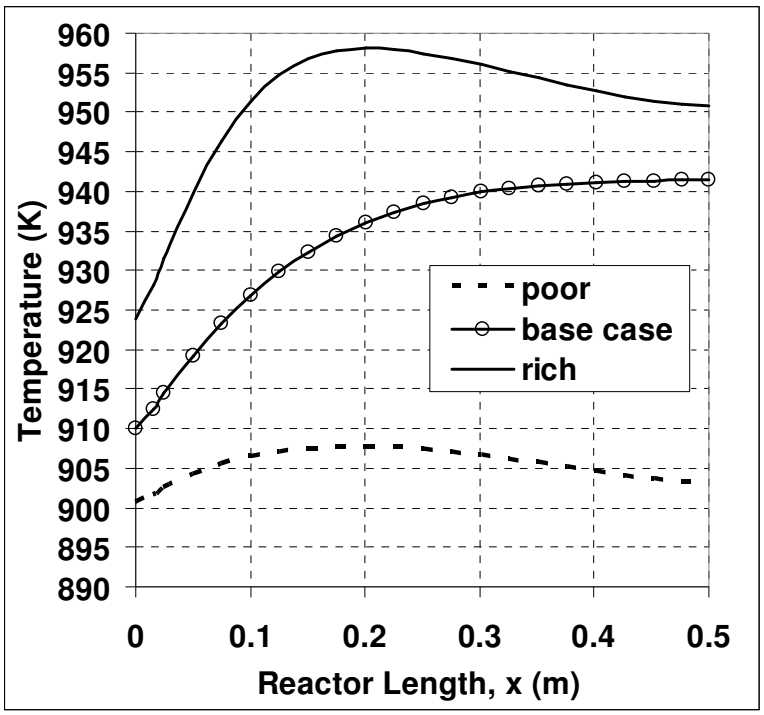

Figure 4.28. Axial temperature profiles on the combustion side of the wall for base case and both oxygen ratio cases

As a result, the temperature difference between the combustion and reforming sides of the wall for the three cases follows the same trend (Figure 4.29). The greatest driving force is in the rich case with an oxygen-to-methane ratio of 4.0, followed by the base case with a stoichiometric ratio of 2.0 and, finally, the poor case with a ratio of 1.0. The values of the maximum temperature differences are 0.25 K, 0.18 K and 0.13 K, respectively.

Figure 4.29 shows that the temperature difference of the rich case becomes lower than that of base case after x = 0.18 and drops to the minimum of all three cases at the reactor exit. This point is also the location where the axial temperature profiles of wall center and channel centerlines reach a maximum before starting to cool down; after this

point, the combustion rate is unable to keep up with the increased rate of reforming into which it has been feeding more heat than in the base case, resulting in a temperature decrease everywhere along the reactor, including the wall.

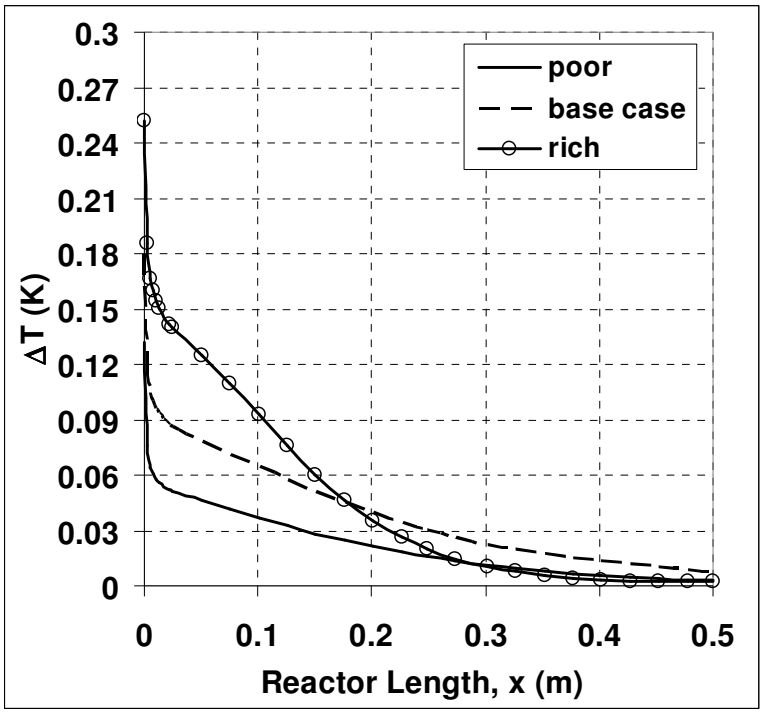

Figure 4.29. Axial temperature difference profiles between combustion and reforming sides of the wall for base case and both oxygen ratio cases

4.1.6. Comparison of Exit Compositions

The exit conversions of endothermic steam reforming and exothermic total oxidation channels for all the cases analyzed and their parameters are summarized in Table 4.2.

It can be seen that altering the reactor configuration in terms of wall thickness and wall material in the ranges listed in the Table does not lead to any significant effect over the outlet conversions of reactants. However, changing the reactant ratios of the inlet gas streams, especially decreasing water-to-ethanol ratio in steam reforming and oxygen-to-methane ratio in total oxidation, affects dramatically the ethanol and methane conversions in these two cases, respectively. Therefore, focusing on these two cases and comparing them with base case is more appropriate and important from an operational point of view.

Table 4.2. Exit conversions in ethanol steam reforming-methane total oxidation

Case	Ethanol Conversion (%)	Methane Conversion (%)
base case *(δ_s = 2 mm) (k_s = 38 W/m.K) (water-to-ethanol = 3) (oxygen-to-methane = 2)*	76.6	86.7
Thickness Cases		
thin *(δ_s = 1 mm)*	76.6	86.6
thick *(δ_s = 4 mm)*	76.6	86.9
Material Cases		
alloy *(k_s = 317 W/m.K)*	76.6	87.4
silica *(k_s = 2.62 W/m.K)*	76.6	86.7
Water Ratio Cases		
deficient *(water-to-ethanol = 2)*	49.9	88.6
excess *(water-to-ethanol = 6)*	77.3	86.6
Oxygen Ratio Cases		
poor *(oxygen-to-methane = 1)*	75	40.44
rich *(oxygen-to-methane = 4)*	77	99.6

Axial concentration at the centerlines of ethanol steam reforming and methane total oxidation channels for the base case are plotted in Figures 4.30 and 4.31, respectively. In order to see the changes in the concentration profiles arising from changing feed composition, the concentration profiles along the channel centerlines of the negatively affected reforming channel in the “water-deficient case” and those of the combustion channel of “oxygen-poor case” are also presented in Figures 4.32 and 4.33, respectively.

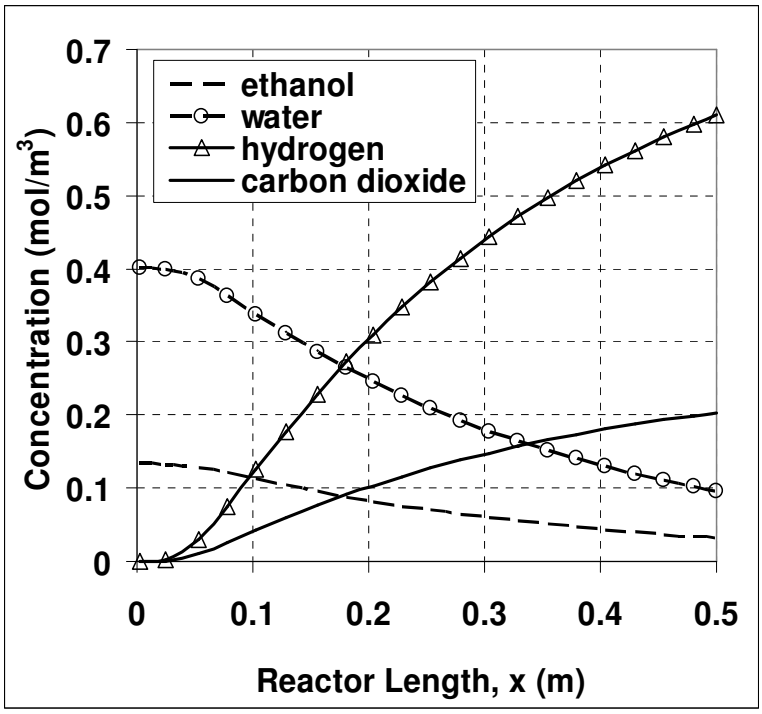

Figure 4.30. Axial concentration profiles for ethanol steam reforming of the base case at the channel centerline

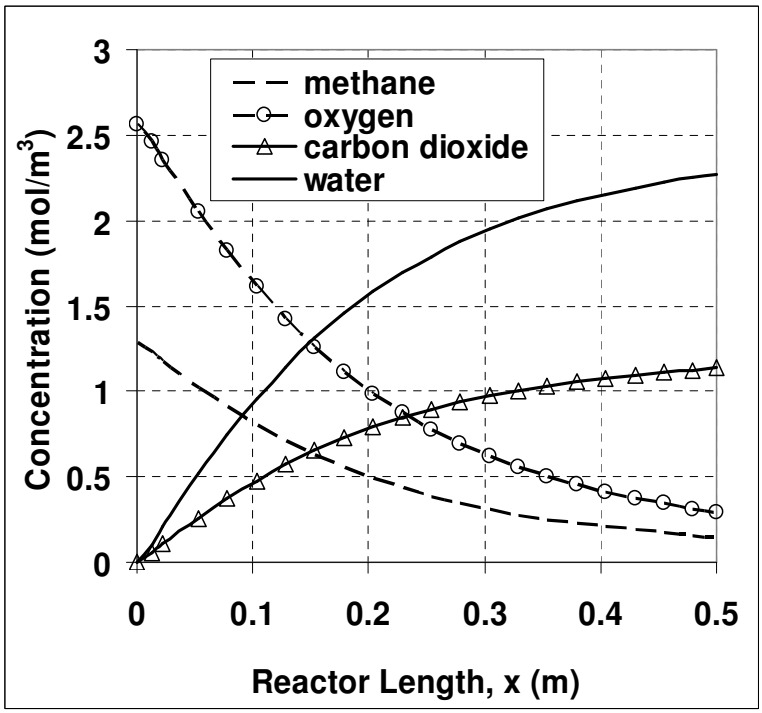

Figure 4.31. Axial concentration profiles for methane total oxidation of base case at the channel centerline

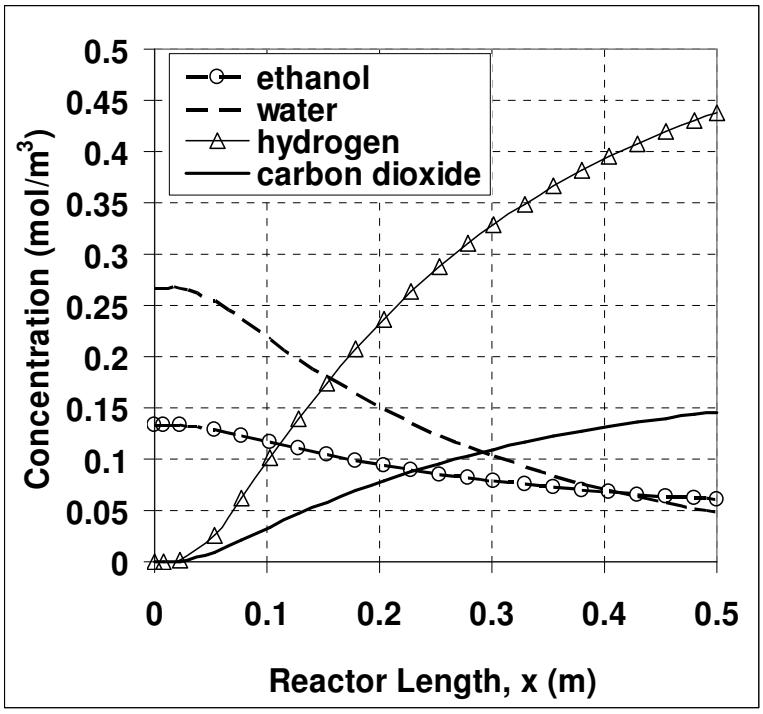

Figure 4.32. Axial concentration profiles for ethanol steam reforming at the channel centerline in the water-deficient case

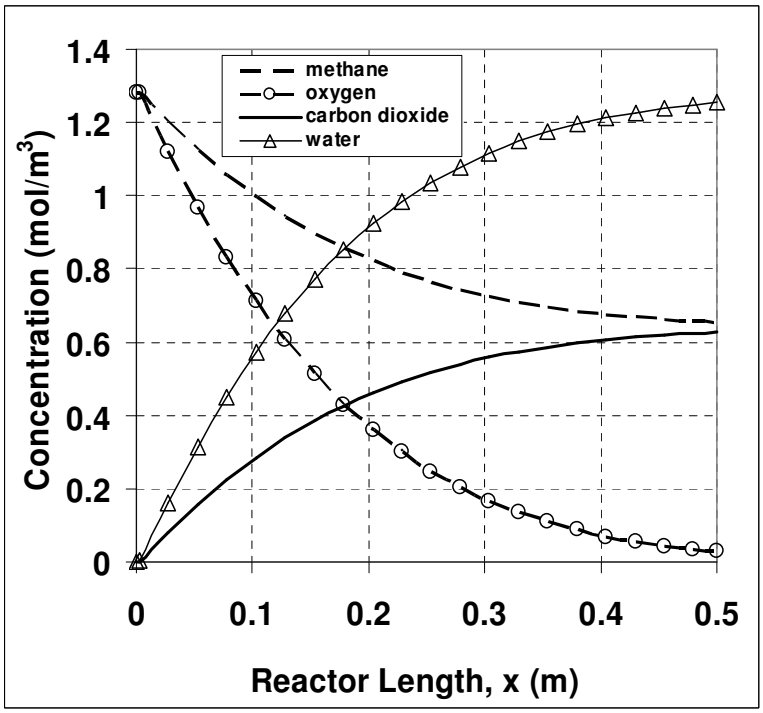

Figure 4.33. Axial concentration profiles for methane total oxidation at the channel centerline in the oxygen-poor case

A comparison of Figures 4.30 and 4.32 indicates that in Figure 4.32 the initial ethanol concentrations of both cases are almost the same, while the H_2 concentrations in the exit streams differ greatly, since the water-deficient case has lower product concentrations due to low conversion of ethanol resulting from unavailability of enough water (Figure 4.34). Figures 4.31 and 4.33 reveal that although the initial concentration of methane is almost same in both the base case and the oxygen-poor case, the exit conversions of the base case are higher. Figure 4.35 shows the disparity in the methane conversions.

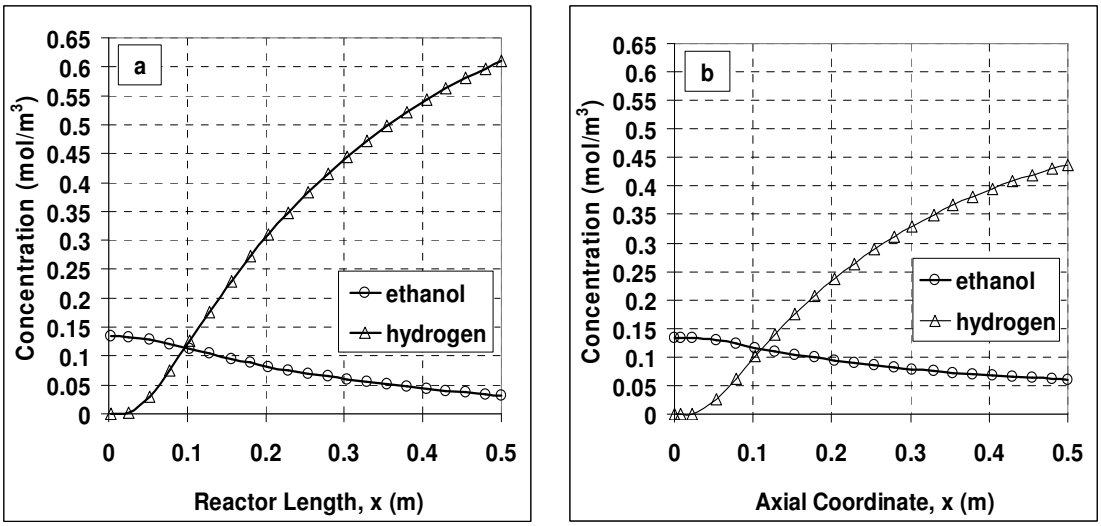

Figure 4.34. Comparison of ethanol and hydrogen concentrations along the channel centerlines of (a) base case (b) water-deficient case

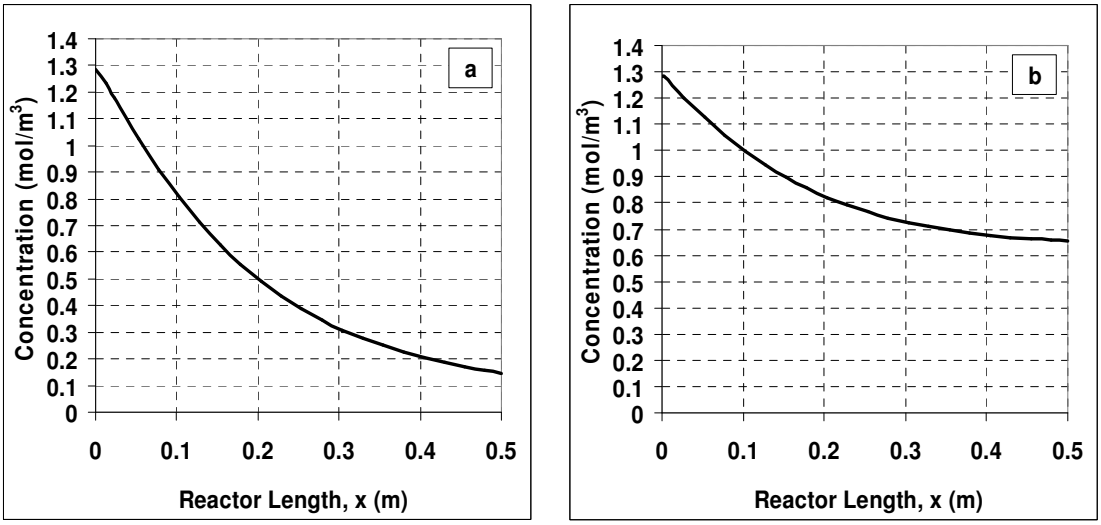

Figure 4.35. Comparison of methane concentrations along the channel centerlines of (a) base case (b) oxygen poor case

In the light of the Figures 4.30-4.35 and Table 4.2, it can be deduced that changing the reactor configuration parameters like wall thickness or wall material did not affect the overall performance significantly because, even though the thickness of the wall was quadrupled in the study, a wall of 4 mm thickness is still considerably thin. Adding the positive effects of small channel height to small wall thicknesses, the employment of wall materials with really low thermal conductivity values did not change the performance in a positive or negative way. The exit compositions of both the endothermic steam reforming and exothermic methane oxidation streams for the two cases mentioned and the base case are summarized in Table 4.3.

Table 4.3. Inlet and outlet compositions of reforming and oxidation streams for the base, water-deficient and oxygen-poor cases

Channel	Chemical Species	Base Case [mol/sec]		Deficient Case [mol/sec]		Poor Case [mol/sec]	
		in$\times10^{-4}$	out$\times10^{-4}$	in$\times10^{-4}$	out$\times10^{-4}$	in$\times10^{-4}$	out$\times10^{-4}$
Ethanol steam reforming; Endothermic, channel 2	C_2H_5OH	12.030 1.004%	2.818 0.225%	12.030 0.997%	6.028 0.485%	12.030 1.004%	2.946 0.236%
	H_2O	36.080 3.011%	8.454 0.676%	24.100 1.998%	4.112 0.331%	36.080 3.011%	8.837 0.707%
	CO_2	0	22.306 1.784%	0	15.886 1.277%	0	22.050 1.764%
	H_2	0	66.918 5.351%	0	47.659 3.832%	0	66.151 5.292%
	N_2	1150 95.985%	1150 91.964%	1170 97.004%	1170 94.075%	1150 95.985%	1150 92.001%
Methane total oxidation; Exothermic, channel 1	CH_4	5.132 9.601%	0.682 1.217%	5.132 9.601%	0.583 1.041%	5.132 9.601%	3.057 5.541%
	O_2	10.260 19.195%	1.364 2.435%	10.260 19.195%	1.166 2.081%	5.132 9.601%	0.128 0.231%
	CO_2	0	5.304 9.468%	0	5.403 9.645%	0	2.929 5.310%
	H_2O	0	10.607 18.936%	0	10.805 19.289%	0	5.858 10.620%
	N_2	38.060 71.204%	38.060 67.944%	38.060 71.204%	38.060 67.944%	43.190 80.798%	43.190 78.298%

4.2. Dynamic Modeling of the CPR

The steady-state CPR model developed in Section 4.1 was extended to investigate the time-dependent behavior of the reactor. The results of the transient solution of the system are presented in Figures 4.36 - 4.38.

Figure 4.36 shows the axial temperature profiles of the channel centerline of the combustion channel at various times. The plots start with the profiles obtained at t = 50 sec, proceed with plots at three other time values and are finally completed with the temperature profile at t = 3000 sec, which is the time when the system is very close to steady state conditions.

The simulation was actually terminated at t = 3800 sec, which gave a difference of only 1.0 K with the steady state exit temperature. The plots of transient solutions obtained at t = 3000 are shown in the present section for the sake of a clearer illustration since the plot of t = 3800 sec and the steady state plot almost coincide with each other on every point along the axis except the exit.

In Figure 4.30, it can bee seen that plots at increasing time intervals follow a regular trend starting from t = 50 sec up to steady state operation. A hot spot is noticeable in the centerline of each solution before the t = 3000 sec profile is reached. This hot spot moves axially downstream the reactor with increasing time and disappears at t = 3000 seconds and x = 0.35 m. It shows the axial advancement of the reaction frontier on the catalyst layer. The rate of the reaction, therefore the heat generation, increases axially along the reactor with increasing time.

The reason of this considerably long time of steady-state achievement is the small temperature gradients inside the reactor caused by small wall thickness and channel heights.

Figures 4.37 and 4.38 show the temperature profiles of the channel centerlines of the reforming channel and of the wall, respectively. The same trend is observable for the channel centerline temperature profile of reforming channel and the wall center profile.

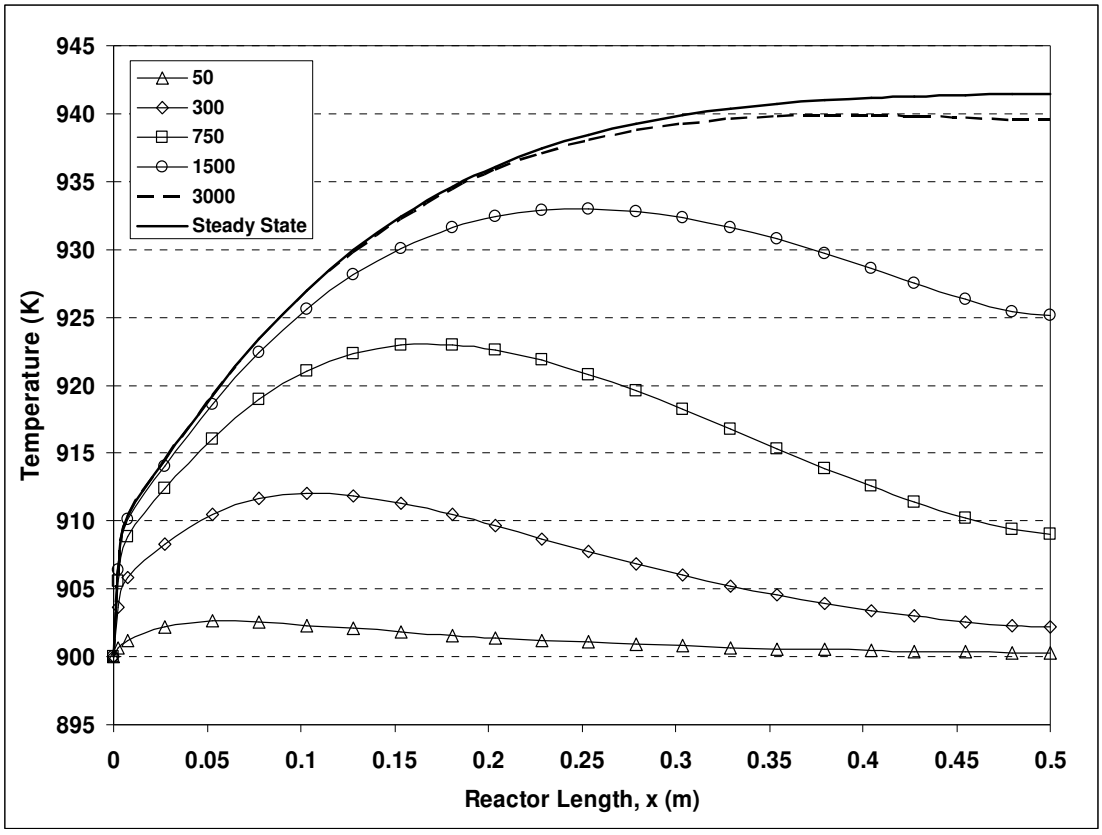

Figure 4.36. Axial temperature distribution of TOX channel centerline at various times

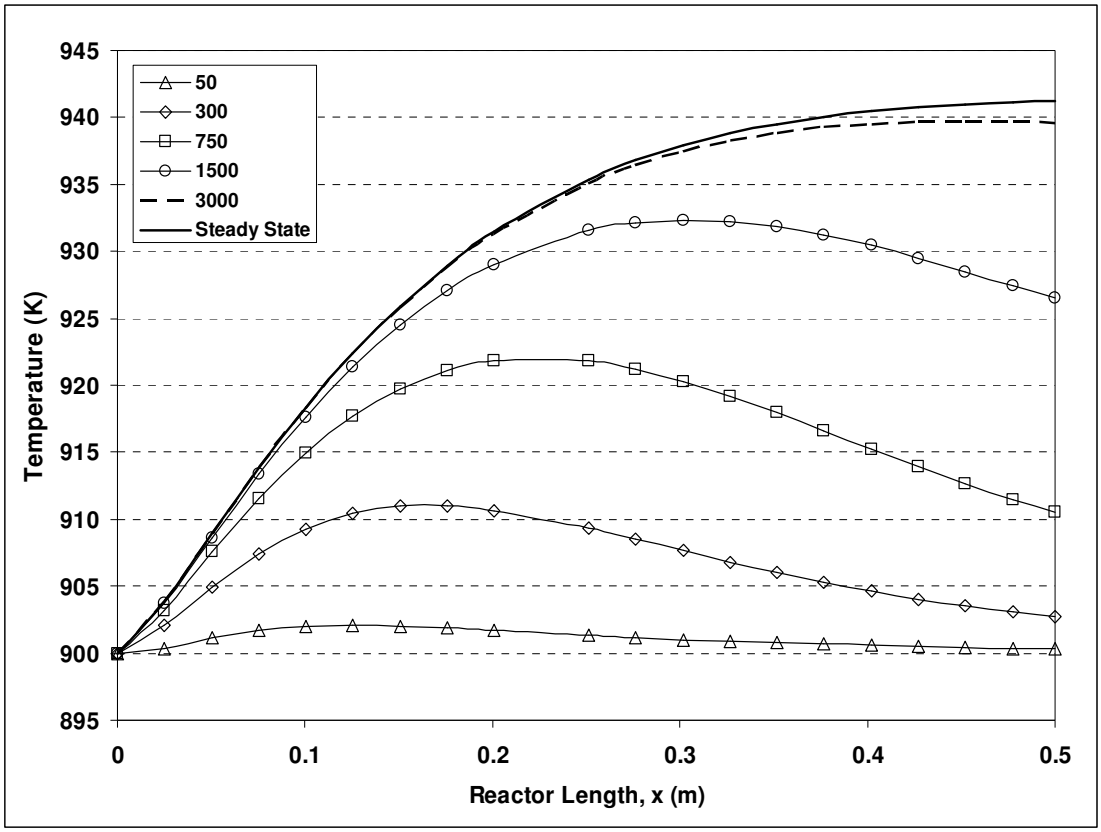

Figure 4.37. Axial temperature distribution of SR channel centerline at various times

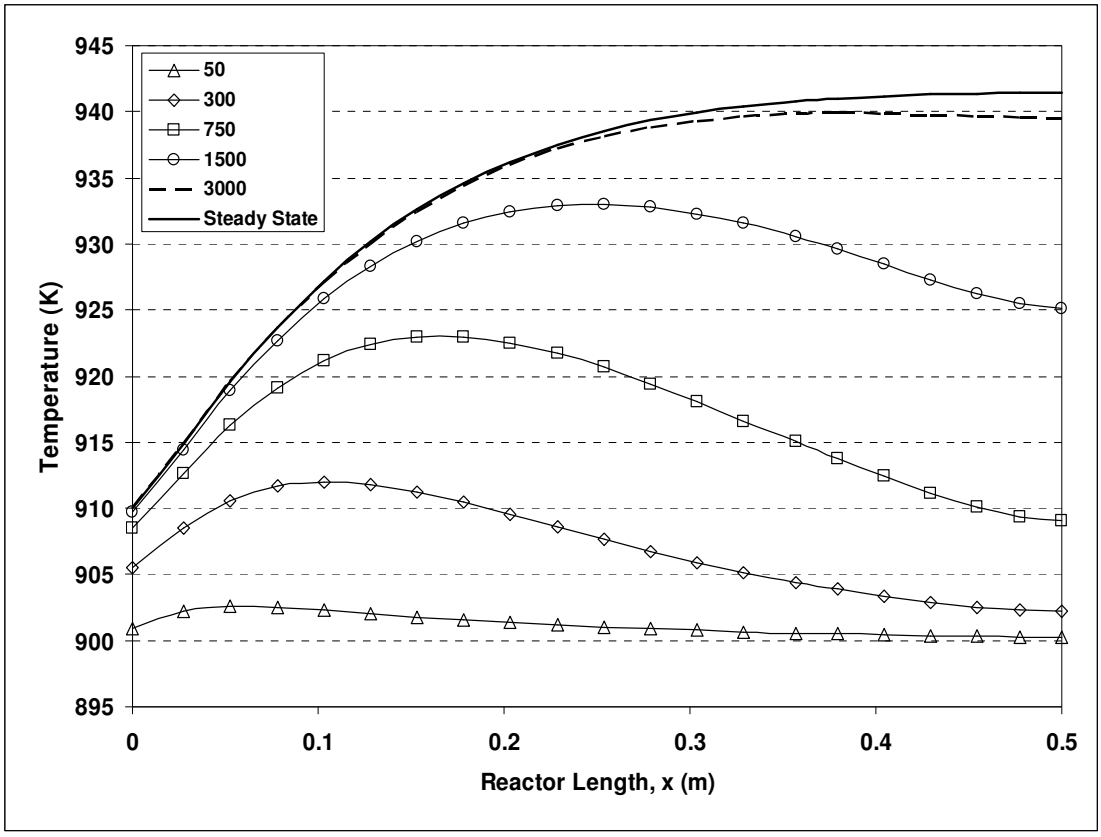

Figure 4.38. Axial temperature distribution of wall center at various times

5. ETHANE DEHYDROGENATION - METHANE TOTAL OXIDATION

5.1. Steady-State Two-Dimensional Modeling of the CPR

5.1.1. The Base Case

The dehydrogenation of ethane coupled with methane total oxidation in a CPR for hydrogen production has been studied by Zanfir *et al.* (2001). A two-dimensional model was used to analyze the reactor behavior under different configurations and operating conditions. The same reaction couple is simulated by the reactor model developed within the context of this work utilizing different kinetic expressions than those of the stated authors. A parametric study is conducted to investigate the influences of the parameters discussed in Chapter 4; the results are then compared with the results of Zanfir *et al.* (2001).

The reactor configuration and operating conditions for the base case of ethane dehydrogenation coupled with methane total oxidation are given in Table 5.1.

Table 5.1. Data used for base case ethane dehydrogenation calculations

Operating Conditions		
Channel	Ethane dehydrogenation	Methane TOX side
Inlet temperature (K)	923	923
Pressure (Pa)	10^5	10^5
Inlet composition (vol. %)	C_2H_6-N_2 mixture	CH_4-air mixture
	10% C_2H_6	9.6% CH_4
	90% N_2	19.2% O_2
		71.2% N_2
Inlet average velocities (m/s)	4.36	1.1
Reactor Geometry		
Catalyst layer thickness	0.1 mm	
Distance between plates	2 mm	
Plate Dimensions (L x w x δ_s)	0.5 m ×1 m × 2 mm	
Plate material	UNS G10060 (6% Carbon Steel)	
Channel cross sectional area	0.001 m^2	

The calculations for base case are carried out with these values and the obtained results are analyzed by interpreting the axial and transverse temperature distributions of the channels and the wall. Figure 5.1 shows the axial temperature profiles of channels centerlines while transverse temperature profiles are displayed in Figure 5.2.

The temperatures in the centerline of the combustion channel are always higher than those of the dehydrogenation channel due to higher flowrate of the latter as compared to the former (Table 5.1), and in addition to that the combustion is the exothermic side. Except for a small portion of the entrance section of the combustion channel, temperature increases smoothly throughout the reactor axis, no hot spots develop as demonstrated in the figure. Axial temperatures of the two channel centerlines are close to each other, and they are the same at the reactor exit. This is a result of the efficient thermal communication between channels provided by the high wall conductivity and small channel height. At the entrance of the reactor, the temperature distribution of the combustion channel shows the same trends of the previously discussed cases and rises from 923 K to 963 K steeply. The explanation of this behavior is presented in section 4.1.1 with Figure 4.5.

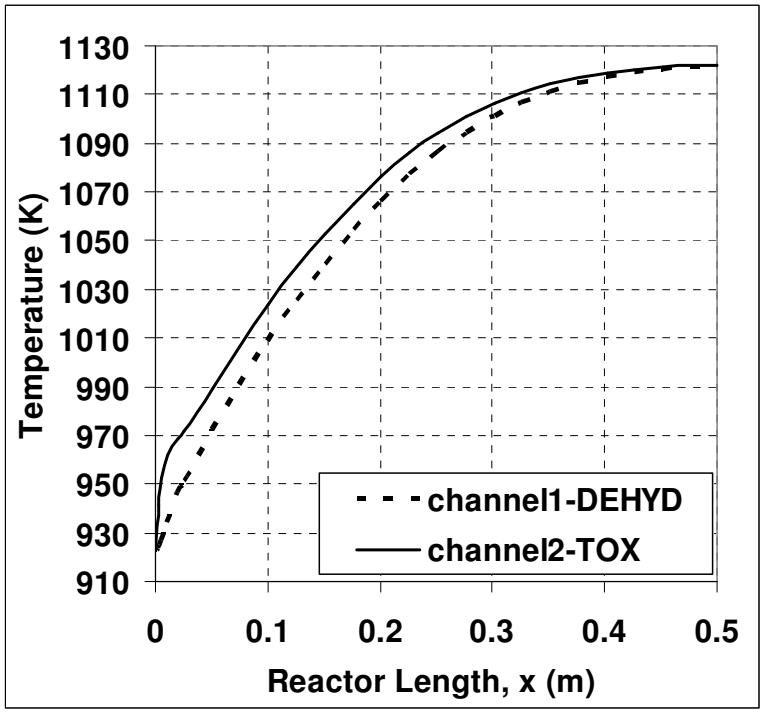

Figure 5.1. Axial temperature profiles of channel centerlines for base case

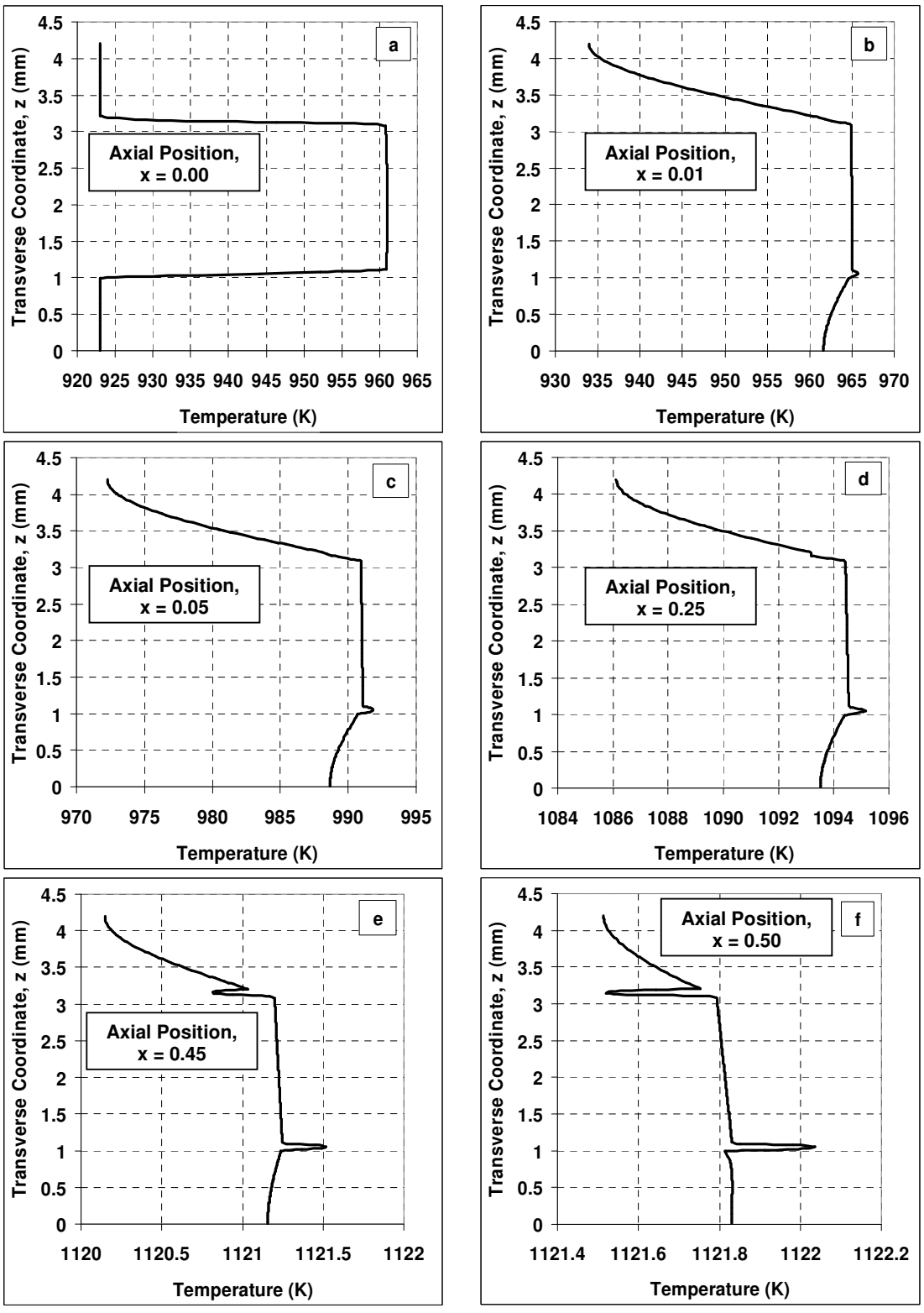

Figure 5.2. Transverse temperature profiles for base case at various axial locations

Plots in Figure 5.2 are the transverse temperature profiles between the two channel centerlines at various axial locations along the reactor, namely at x = 0.0, the entrance; x = 0.01, the first 1/50th section; x = 0.05, the first 1/10th section; x = 0.25 the half; x = 0.45, the last 1/10th and x = 0.50, the exit of the reactor. A temperature difference of 38 K is observed at the channel entrance, between the gas phase and the wall. The gas is at the inlet temperature assigned, 923 K, while the wall is hotter due to heat conducted axially from downstream through the wall.

Further along the reactor the transverse profiles become less symmetrical and no sharp gradients exist as demonstrated in Figure 5.3 for easier comparison. For example at the exit, x = 0.5, the difference between the maximum and the minimum is only 0.53 K (Figure 5.2(f)). In addition, the highest temperature observed is at the combustion channel catalyst layer, since this is where heat is generated.

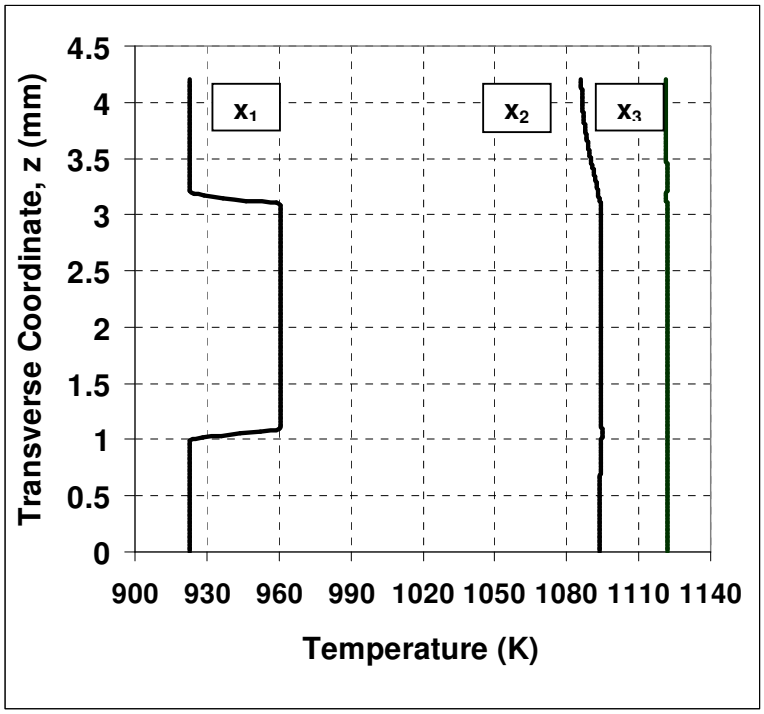

Figure 5.3. Transverse temperature profiles along the reactor for base case at various axial locations; x_1 = 0.0, x_2 = 0.25, x_3 = 0.5

The temperature distributions of both catalyst layers are more noticeable in Figures 5.2(e) and (f), because the abscissas of these graphs represent narrower temperature ranges

than the others. The temperatures in the center of the combustion catalyst layer are the maximum of all everywhere along the reactor as expected. The wall sides of both catalyst layers have higher temperatures than the channel sides. This is because that the interface of the catalyst layer-metal wall is easier to heat than the interface of catalyst layer-gas mixture, due to the high thermal conductivity of the metal wall.

The decrease in the temperature of the wall as one travels from $z = 1.01$ to $z = 3.01$ is visible in Figure 5.2. The temperature profile trend of the catalyst layer of the dehydrogenation channel is the opposite of that of the combustion catalyst layer as expected since dehydrogenation layer is endothermic whereas the combustion layer is exothermic. The temperature decreases faster starting transversely from the dehydrogenation catalyst layer then to the centerline of the dehydrogenation channel than it does in the oxidation side because most of the heat transferred across the wall is consumed in the dehydrogenation catalyst layer. It is harder to heat the gas mixture in the dehydrogenation channel because the flowrate and the linear velocity of the gas mixture are higher.

The highest temperature, 1122 K, is observed at the end of combustion channel catalyst layer; $x = 0.5$, $z = 1.05$, as expected, since this is where heat is generated and at the reactor exit the combustion reaction has the highest conversion value. The lowest temperature is 922.75 K, very close to the initial temperature because the ethane dehydrogenation is less endothermic than ethanol steam reforming and the initial temperature is higher in this system.

From Figures 5.1 and 5.3, it can be seen that towards the end of the reactor, transverse temperature differences disappear and both the channels reach the same temperature, indicating that a balance has been reached between the rates of the exothermic and endothermic reactions and a thermo-neutral state has formed. This is beneficial since it shows that the system can sustain itself and attain steady state operation with the given operating conditions.

The dehydrogenation channel gives an equilibrium conversion of ethane of 64%, which is close to the equilibrium value, $X_e = 74.8\%$. Ethane and methane conversions

reported in literature are 62.2% and 89.5%, respectively (Zanfir *et al.,* 2001). A methane conversion level of 83.8% has been reached with the model employed in this work.

The overall temperature increase along the reactor is 199 K, which is only 41 K in ethanol steam reforming and 130 K in the findings of Zanfir *et al.* (2001). Transverse temperature discrepancies drop from 38 K down to zero, resulting in smooth temperature profiles without any hot or cold spots axially and transversely anywhere along the reactor. Zanfir *et al*. (2001) report a maximum value of 5 K of transverse temperature gradient.

Considering that the reactor models, operating conditions and kinetic expressions are different, it is notable that the results obtained in this study do not contradict those of Zanfir *et al.* (2001) but rather show some differences.

5.1.2. Influence of Wall Thickness

In order to study the effects of wall thickness on the ethane dehydrogenation-methane total oxidation coupled system, the wall thickness is varied as described in section 4.1.2 of the previous chapter. A thin wall case in which δ_s is taken as 1 mm and a thick wall case with δ_s = 4 mm are run and the results are compared.

In Figures 5.4 and 5.5, the thin wall causes a smoother temperature profile compared to the thick case and base case, except a minor jump at the entrance. The steep rise of the temperature of the oxidation channel centerline from 923 K to 986 K in the thick wall and to 963 K in base case disturb the smoothness of the profile plots (Figure 5.1).

After this initial disturbance, the temperature profiles follow a steady rising trend till the exit of the reactor. This disturbance, which is also observed in ethanol steam reforming, is caused by the increased heat resistance introduced by the increased thickness of the wall. As explained in ethanol steam reforming regarding Figure 4.7, the resistance to axial and transverse heat transport is higher in thicker walls; therefore the heat generated by catalytic combustion is not transferred efficiently to the endothermic channel, resulting in an increase in the combustion rate and gas temperatures.

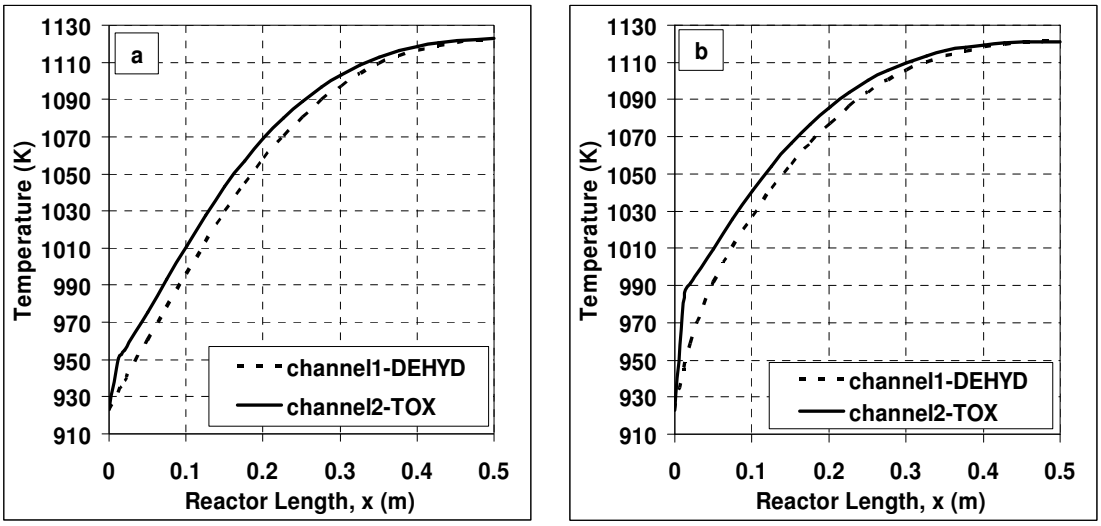

Figure 5.4. Axial temperature profiles of channel centerlines for (a) thin and (b) thick case

In accordance with the expectations, temperatures of thick case are always higher than those of thinner walls as can be seen from Figure 5.5. Just like the base case and the corresponding cases investigated in ethanol SR, the centerline temperatures of the TOX channel for both thickness values are higher than SR channel everywhere along the reactor.

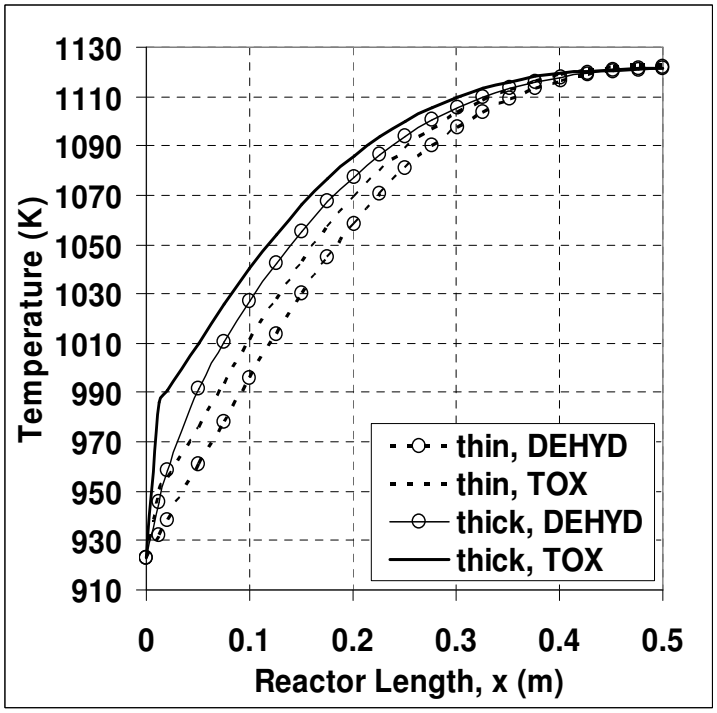

Figure 5.5. Axial temperature profiles of channel centerlines for both thickness cases

In Figure 5.6 the temperature difference between channel centerlines for thick wall has a maximum of 45 K; base case and thin wall have 28 K and 18 K, respectively. In all the three cases these maximum points are located at the same axial position, x = 0.01 m. These peaks are also observable in Figures 5.1, 5.4(a) and (b).

The thick wall has higher differences only up to x = 0.08 m. The base case shows a trend that is in between the plots of the thick and thin cases. This situation was expected, as it was encountered before, necessary explanation is given with Figure 4.8.

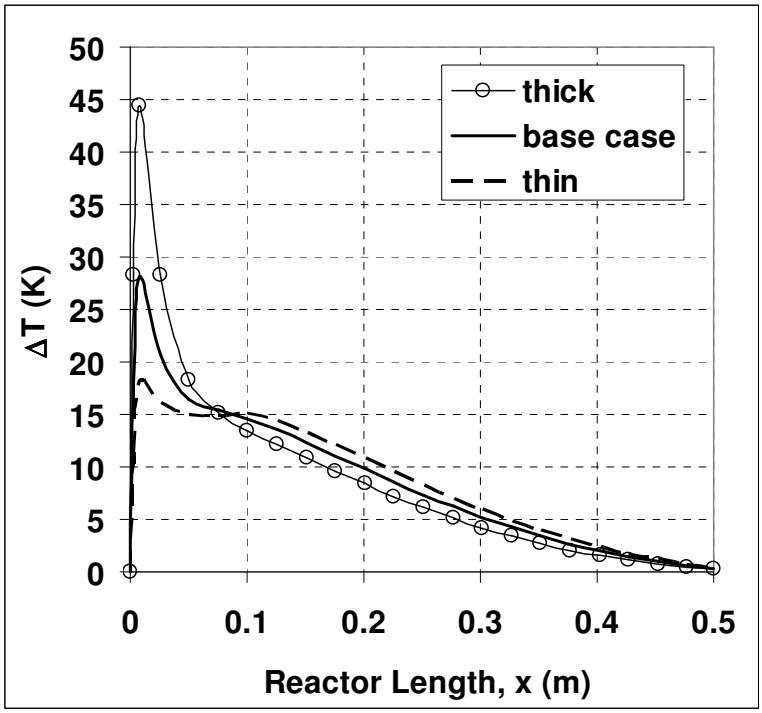

Figure 5.6. Axial temperature difference profiles between centerlines of combustion and dehydrogenation channels for base case and both thickness cases

In thick case, the temperature difference between two sides of the wall is greater than that of thin case as can be seen from Figures 5.7(a) and (b). The differences reach a maximum of 0.4 K for thick wall, whereas this value is only 0.065 K for the thin case. These results are in accordance with the increased resistance across the wall. As thickness increases, so does the resistance to heat transfer across the material.

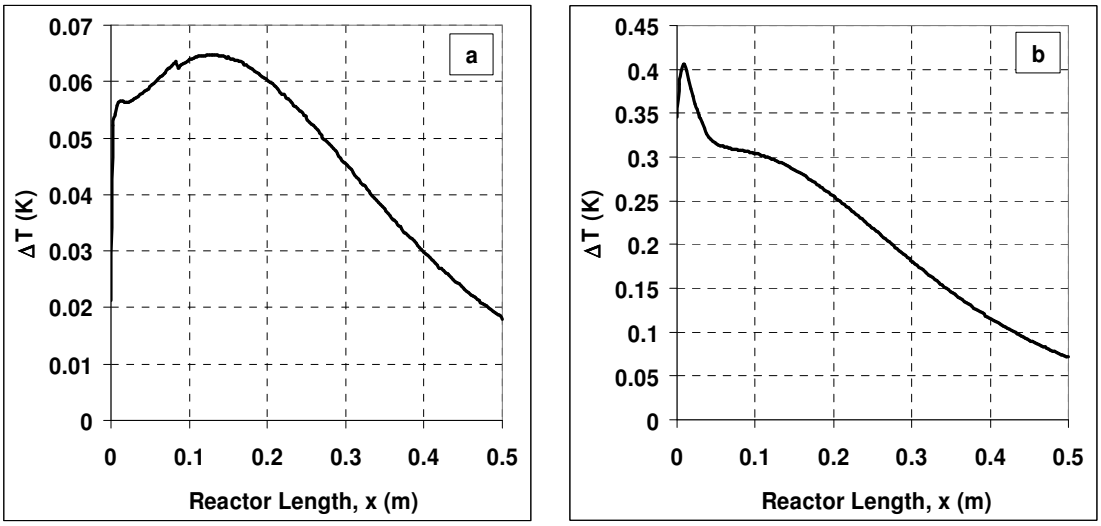

Figure 5.7. Axial temperature difference profiles between the combustion and dehydrogenation sides of the wall for (a) thin and (b) thick cases

Wall center temperature profiles along the axis of the reactor for base case and the two thickness cases are shown in Figure 5.8. The exit temperatures of the three cases are the same, and the base case, shows a trend that is in between the plots of thickness cases.

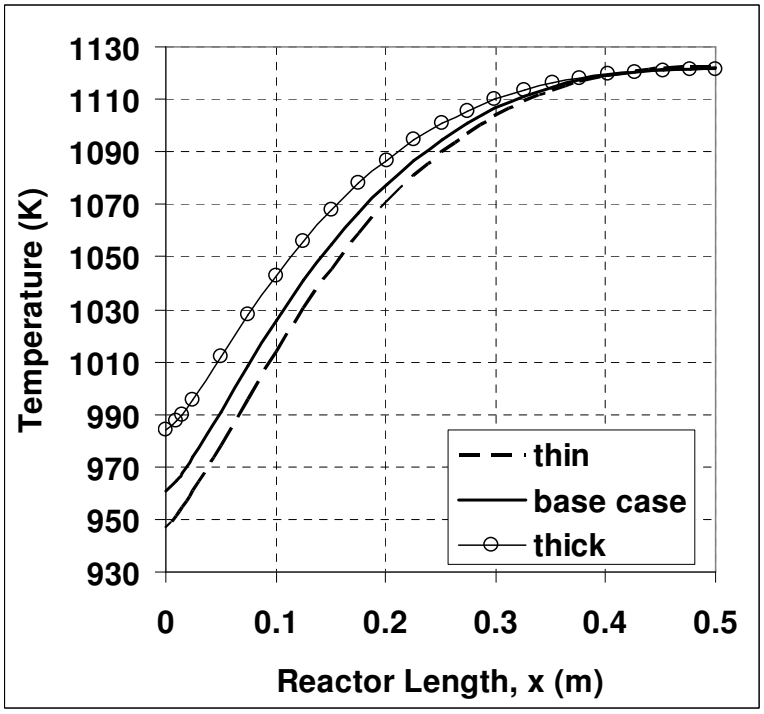

Figure 5.8. Axial temperature profiles of wall centers of base case and both thickness cases

Like what is observed in the ethanol steam reforming chapter, the thickest wall has the highest initial wall temperature, as expected. The reason for this is the greater driving force caused by the higher temperatures of the channels with thicker walls. This phenomenon is also present in the ethanol steam reforming system and more detailed explanations are given in Figure 4.10. Wall temperatures at the initial axial position for thin and thick cases are 947 K and 984 K, respectively.

The transverse temperature profiles across channel centerlines at various axial positions for both thin and thick cases are given in Figure 5.9.

The highest and the lowest temperatures of the channels are the same as in the base case, 1122 K and 923 K. The locations of these maximum-minimum temperature values are also same except for the minimum of the thin wall case. As opposed to the other two, thin case has its temperature minimum in the dehydrogenation catalyst layer, like the case in ethanol steam reforming system. However, the exact value, 923.67 K, is not significantly different than the initially assigned value.

When the trends of the plots in the subdomains of the rector (endothermic channel, endothermic catalyst layer, metal wall, exothermic catalyst layer and exothermic channel) are investigated, it can be seen that they behave like their counterparts in ethanol steam reforming system.

Although with only slight differences, the effects of wall thickness on the conversion values of the reactants are also observable. The conversions of ethane and methane in thin case are 63.3% and 84.5%, respectively. For the thick case, these conversion values rise up to 66.2% and 84.5%. As one can see, the increased thickness of the wall also increases the conversion values in endothermic channel. Because thicker wall brings more solid phase resistance to the system, posing a detrimental effect on transverse and axial heat conduction. Heat trapped in the exothermic channel causes the temperature rise everywhere in the reactor, increasing both the exothermic and endothermic reaction rates.

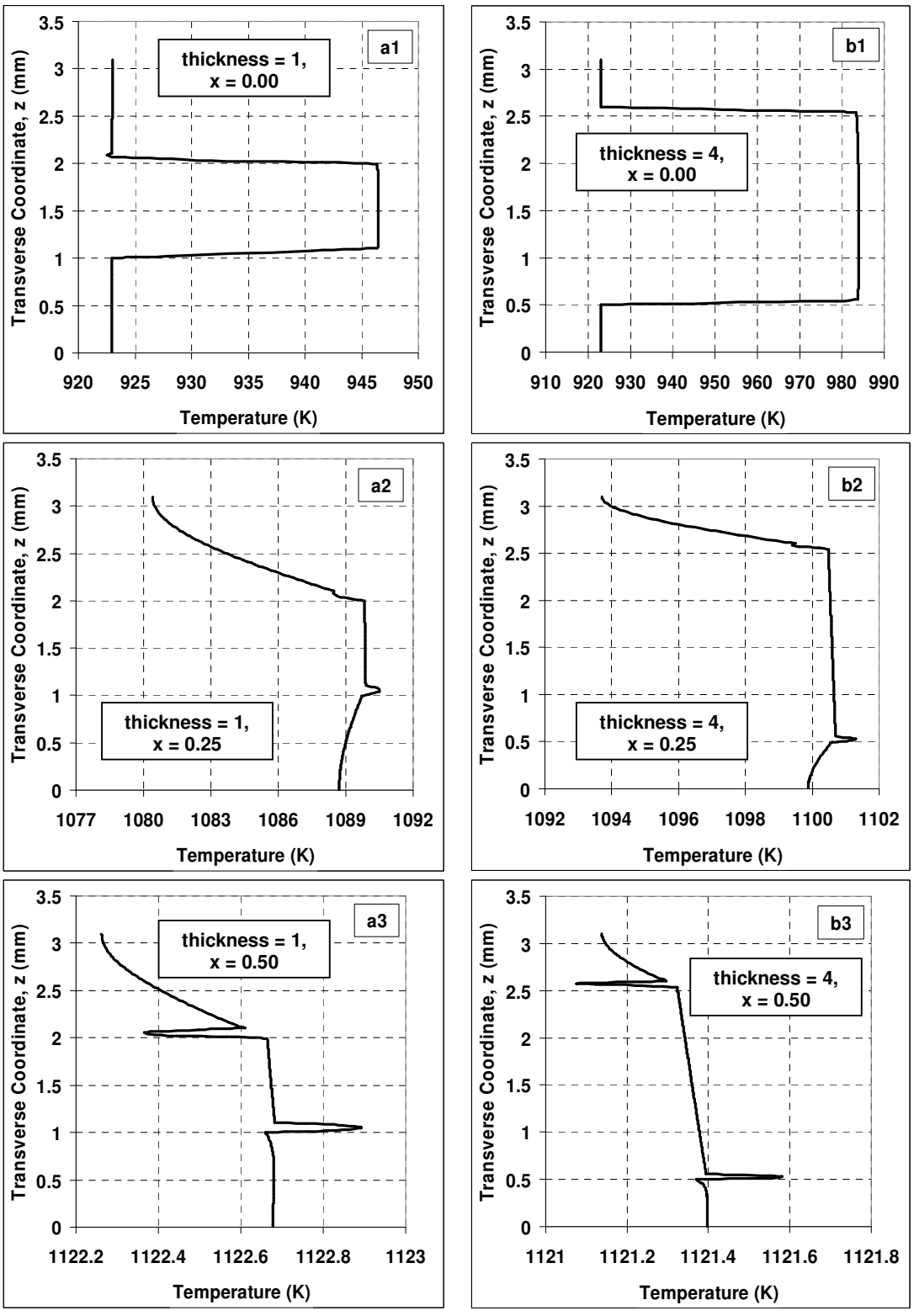

Figure 5.9. Transverse temperature profiles for thickness cases at various axial locations

For the thin case, the maximum transverse and axial temperature discrepancies across and along the reactor are 23.5 K and 199 K, respectively. These values are 61 K and 199 K for the thick case (Figures 5.5, 5.9(a1) and (b1)). But at the end of the reactor no transverse differences occur and a thermo-neutral state is reached in terms of axial temperatures for both thickness cases. The reason for the transverse discrepancy maximum of the thick case being greater than that of thin case is the increased resistance across the wall.

5.1.3. Influence of Wall Material

Base case calculations presented for ethane dehydrogenation are performed with the same wall material of the ethanol steam reforming model. The average thermal conductivity of carbon steel in the operating temperature range of 923 K-1122 K is 35.5 W/m.K.

For different wall materials, Corning 7940 and pure nickel are used and their thermal conductivities are 3 W/m.K and 72.25 W/m.K, respectively.

Channel centerline temperature profiles of the two investigated materials are given in Figures 5.10 and 5.11. In Figure 5.10(a) no significant transverse temperature differences appear. The same type of phenomenon is studied in ethanol steam reforming-methane combustion coupled system. The effects of the thermal conductivity of the material and axial heat conduction are known; therefore what is presented in this figure is in accordance with the expectations. Another expectation met is that the temperature in the centerline of the endothermic channel is always lower than that of the combustion channel for both material cases.

In the base case and nickel case plots, some of the features of the axial temperature distribution of the combustion channel of the silica case, like being smoother, are not present (Figures 5.10(b) and 5.11). The initial rise in the temperatures of the total oxidation channel of the nickel wall is caused by its better thermal conductivity.

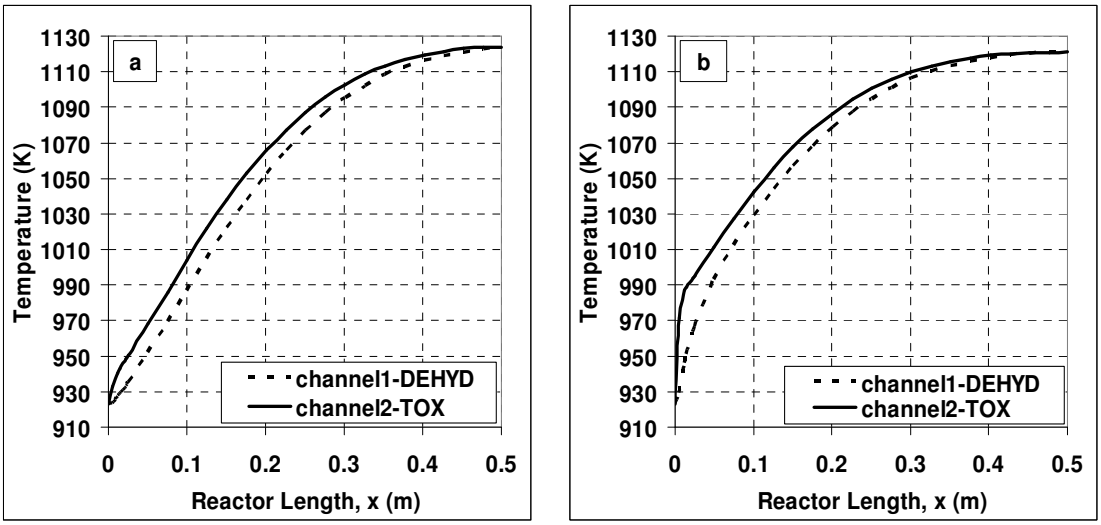

Figure 5.10. Axial temperature profiles of channel centerlines for (a) silica and (b) nickel

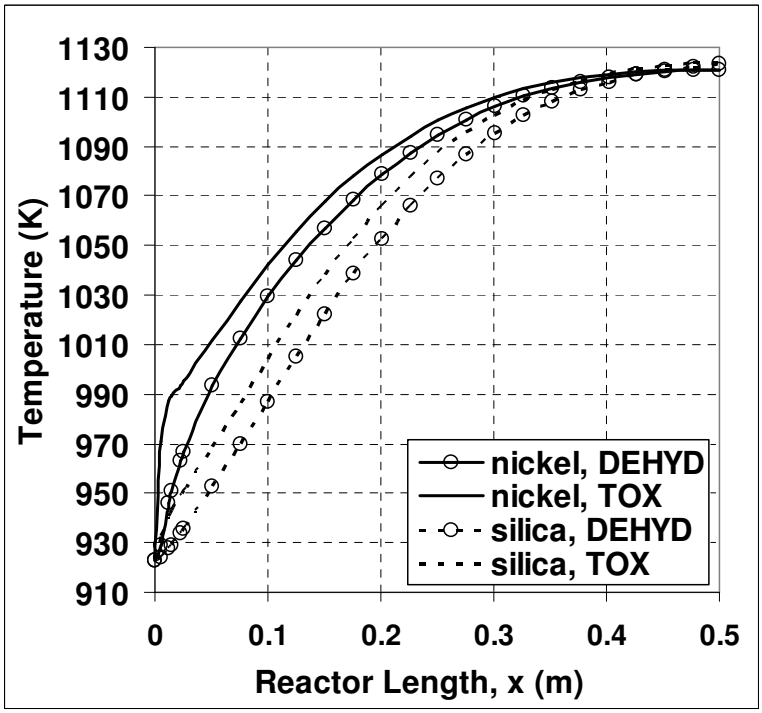

Figure 5.11. Axial temperature profiles of channel centerlines for both material cases

When temperature differences between channel centerlines along the reactor axis for both silica and nickel cases are considered in Figure 5.12, it can be seen that only after the entrance region of the reactor are the differences of the nickel case smaller. It was expected to be so throughout the entire reactor axis. Therefore it can be said that the low resistance

material wall behaves like the thicker wall which is investigated in the previous section. The same situation is explained in Chapter 4 of ethanol steam reforming-methane combustion coupled system, regarding Figures 4.12 and 13.

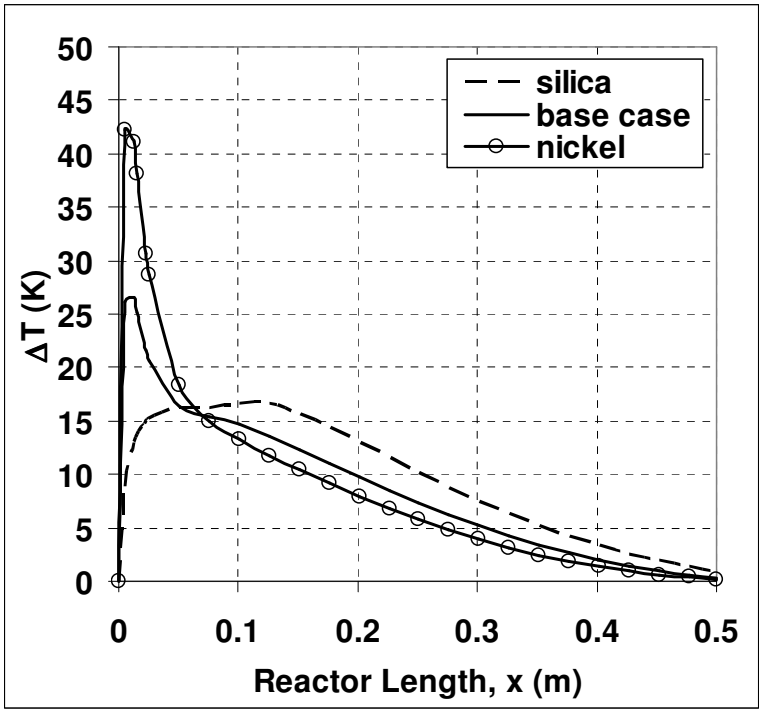

Figure 5.12. Axial temperature difference profiles between channel centerlines for base case and both material cases

The temperature difference between the total oxidation and dehydrogenation sides of the wall are plotted along the reactor axis in Figure 5.13. The resistance to heat transfer being higher, the temperature difference for the silica case is also higher than nickel case; the maximum value is approximately 17 times larger.

In Figure 5.14 it can be seen that the temperature of the wall at the entrance is the set initial temperature in silica case, but the nickel wall starts at 986 K, 63 K higher than the initial condition and the exit temperature of silica is slightly higher than that of nickel. These findings were expected and are in accordance with nickel being the high conductivity material and silica the high resistance material.

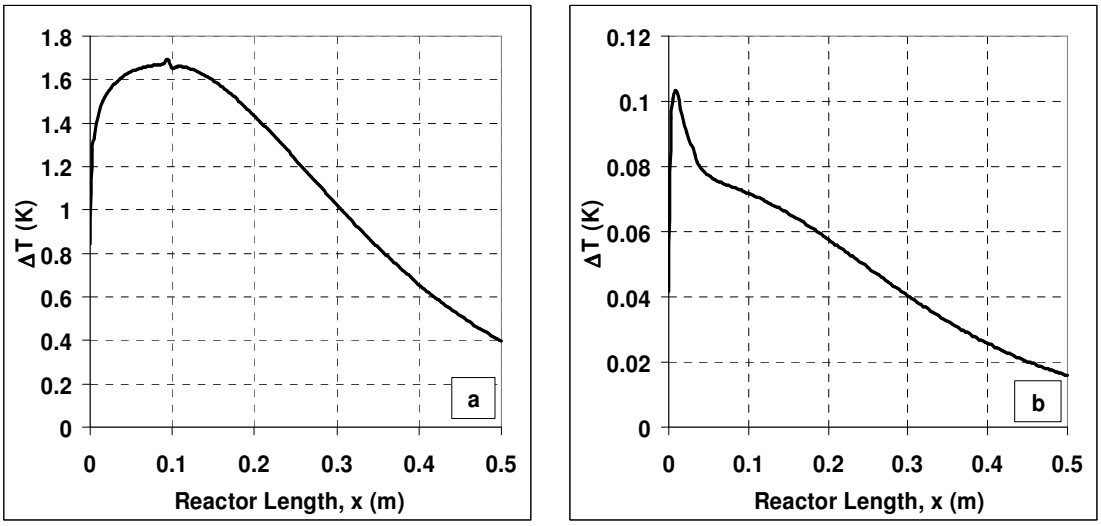

Figure 5.13. Axial temperature difference profiles between the combustion and reforming sides of the wall for (a) silica case and (b) nickel case

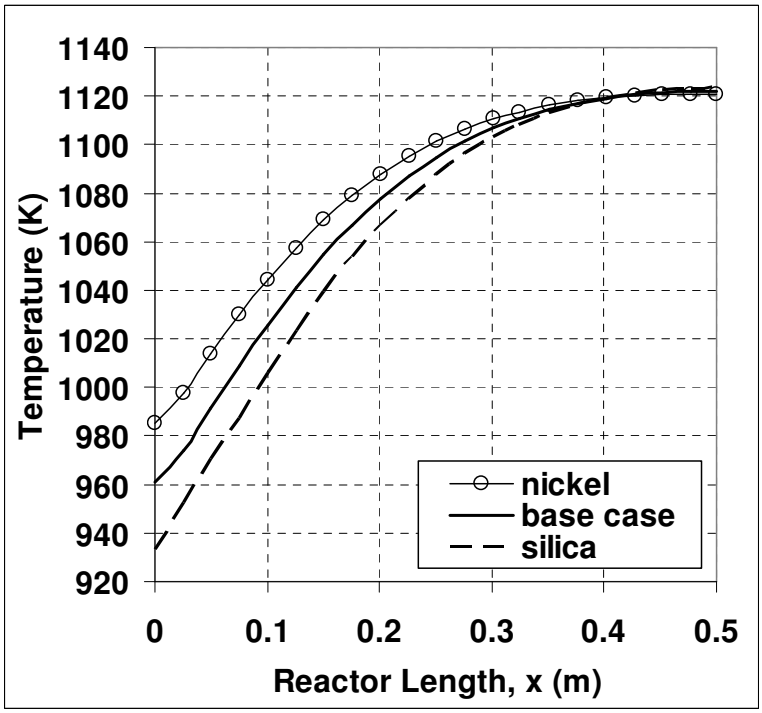

Figure 5.14. Axial temperature profiles for wall centers of base case and both materials

Figure 5.15(a) shows that in silica case, the wall side of dehydrogenation channel heats up and increases the difference along the entrance region, up to x = 0.1 m. The centerline temperatures of the dehydrogenation channel then start to increase faster than

the wall side does, so the difference drops down to zero at the exit. Considering the nickel wall, one can see that the wall sides of both channels start 63 K higher than the channel centerlines (Figures 5.15(b) and (d)), which is a result of the high thermal conductivity.

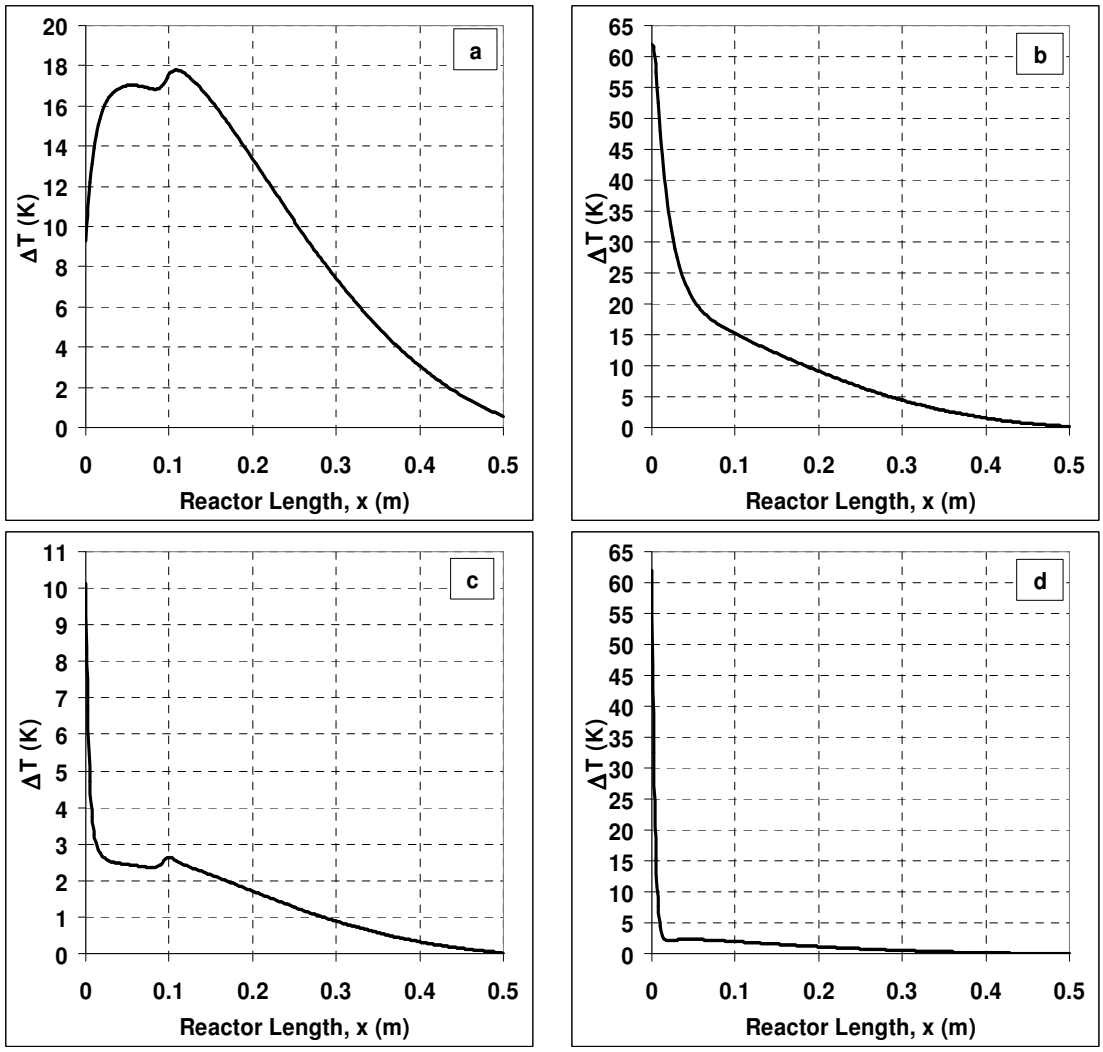

Figure 5.15. Axial temperature difference profiles between channel centers and the wall sides of channels for both material cases; (a) channel 1-silica, (b) channel 1-nickel (c) channel 2-silica, (d) channel 2-nickel

The plots showing defined temperature differences along the axis in the reactor for dehydrogenation-combustion coupled system are Figures 5.12, 5.13 and 5.15. In these figures the system behaves as expected except the entrance region of the reactor. After about 0.1 m axially downstream, it can be seen that the silica case has higher temperature

gradients (Figures 5.12, 5.13(a) and 5.15(a)). The most significant differences are between channel centerline and the wall side of the dehydrogenation channel and the centerlines of both channels with values of 17 K and 18 K, respectively. When nickel is used as wall material, the corresponding temperature differences are 13 K and 15 K. As expected, the differences are higher in silica case.

The conversion values of methane and ethane in silica case are the same as the base case values, 83.9% and 62.5%, respectively. However, when nickel is used as wall material, ethane reaches 66.4% and methane reaches 84.7% conversion due to the more efficient heat transfer it provides throughout the entire reactor.

The highest temperature is very close to 1122 K in both cases, the value for the base case, the lowest temperature in silica case, 920 K, is observed at the entrance of the reactor, and in the middle of the dehydrogenation catalyst layer. This resemblance to the reforming-combustion coupled system is due to the hindered heat transfer. The endothermic reaction makes use of the sensible heat in the gas mixture because the heat generated in the combustion channel is not available yet. Base case and nickel wall case have the same location and value of temperature minimum of 920 K. This is probably because that the dehydrogenation reaction is less heat dependent than the steam reforming and the thermal properties of carbon steel and nickel are closer to each other than copper alloy.

Figures 5.16(a) and (b) give transverse temperature profiles at various axial locations along the reactor for silica and nickel cases, respectively. At the entrance, the maximum of transverse temperature gradients between wall and channel centers are observed, the values being 10 K for silica and 63 K for nickel. Nickel case has higher gradients as opposed to what was expected because it transfers heat more easily. At the exit these gradients become zero. In Figures 5.16(a3) and (b3) the steep decrease of temperature across the more resistant silica is observable.

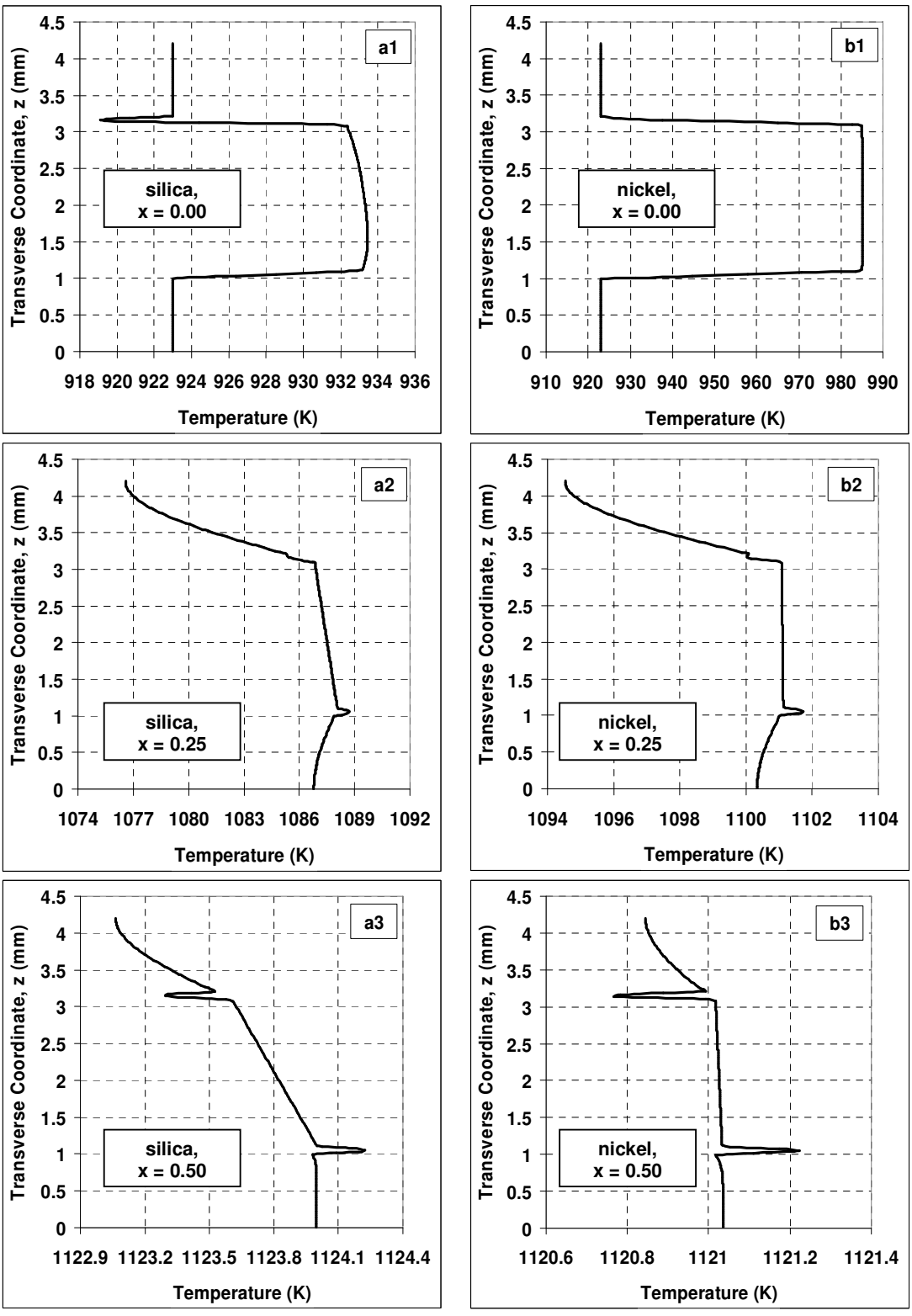

Figure 5.16. Transverse temperature profiles for material cases at various axial locations

5.1.4. Influence of Oxygen-to-Methane Ratio

The effects of varying the oxygen-to-methane ratio on the ethane dehydrogenation-methane total oxidation coupling system are investigated in this section. Two different simulations were run; one with an oxygen "poor" feed stream and the other with a feed stream that is "rich" in oxygen, by varying the volumetric percentages of the inlet mixtures into the combustion channel. The oxygen poor case has an oxygen-to-methane ratio of one, while that of rich case is 2.9. These two cases and the base case are compared among each other to observe the changes in reactor thermal behavior and reactant conversions.

The channel centerline temperature profiles along the reactor axis for the two oxygen-to-methane ratio cases are given in Figures 5.17(a) and (b), same type of plot for the base case with oxygen-to-methane ratio of two, i.e. base case, is provided in Figure 5.1. For easier comparison, the two cases are presented together in Figure 5.18.

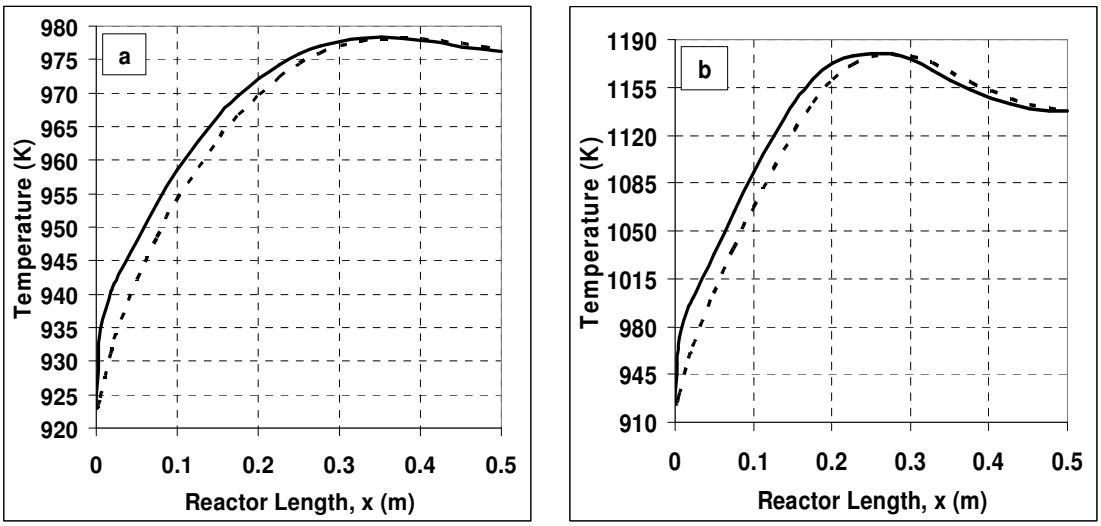

Figure 5.17. Axial temperature profiles of channel centerlines for (a) oxygen poor and (b) oxygen rich case

It is observed from Figures 5.17(a) that poor case has a slower combustion rate, and a lower conversion of 31.7%. Compared with the base case, the temperatures everywhere along the reactor are lower as the heat generation rate has decreased. As expected, ethane dehydrogenation rate and conversion also decrease to 30.8%. Both channels start to cool down after x = 0.36 and the temperatures of dehydrogenation channel are slightly higher

than oxidation. The exit temperature is 976.5 K, lower than that of the base case as expected.

In the oxygen poor case, the heat consumption rate is greater than the heat generation rate. As can be seen from the figure, after $x = 0.38$ the shortage of the fuel starts to become effective, the exothermic reaction rate slows down, resulting to low temperatures everywhere along the rest of the reactor. Consequently, the rate of the endothermic reaction slows down too.

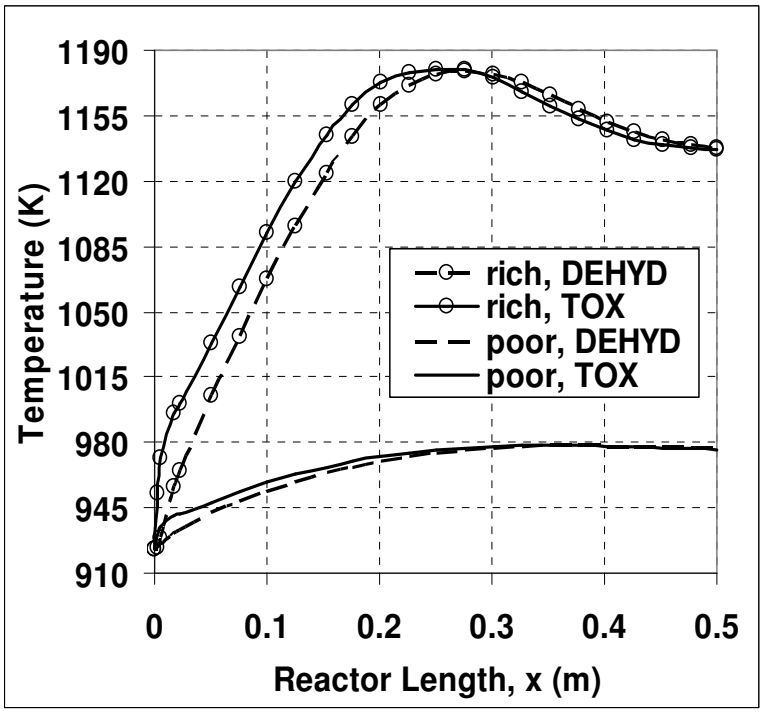

Figure 5.18. Axial temperature profiles of channel centerlines for both oxygen ratio cases

In the oxygen rich case, the amount of heat generated is greater so the temperature at every point along the reactor is higher than the base case and poor case values as expected (Figures 5.17(b), 5.18, 5.19 and 5.20). Another outcome is that the exit conversions of the channels have also increased to 94.5% and 80% in methane and ethane, respectively. Similarly to the reforming-combustion coupled system, hot spots form at $x = 0.24$ in wall center temperature profile and at $x = 0.26$ and $x = 0.28$ in combustion and dehydrogenation channel centerlines, respectively. After these maximum points, the temperatures start to decrease due to the fact that the rise in temperature had accelerated the endothermic

reaction, which in turn results to an increase in heat consumption. The temperature decrease is greater in the combustion channel than it is in the endothermic channel as expected.

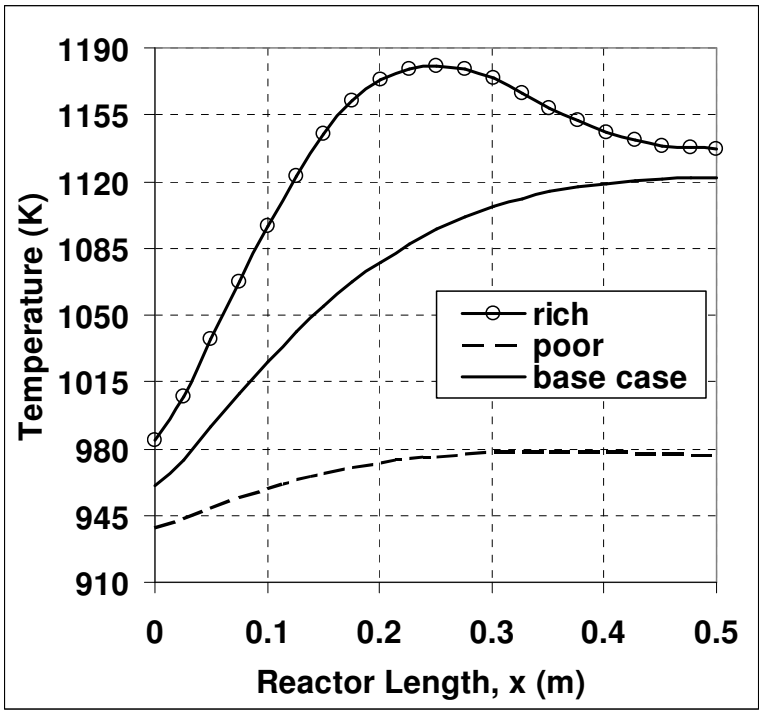

Figure 5.19. Axial temperature profiles on the combustion channel side of the wall for base case and both oxygen ratio cases

The resulting trends in the axial temperature profiles of the combustion side of the metal wall for the three cases are as expected. The maximum point of the profile increases with increasing oxygen-to-methane ratio from 978 K to 1122 K for the base case and then to 1180 K as can be seen in Figure 5.19. The hot spot generated on $x = 0.24$ in the oxygen rich case is also visible.

The axial temperature profile of the wall center is given in Figure 5.20 for the three cases. The initial temperature of the wall increases from oxygen poor case to rich case. The reactor has higher temperatures in richer cases, therefore axial heat conduction through the wall from hotter sections to $x = 0$ is easier, resulting in higher wall temperatures.

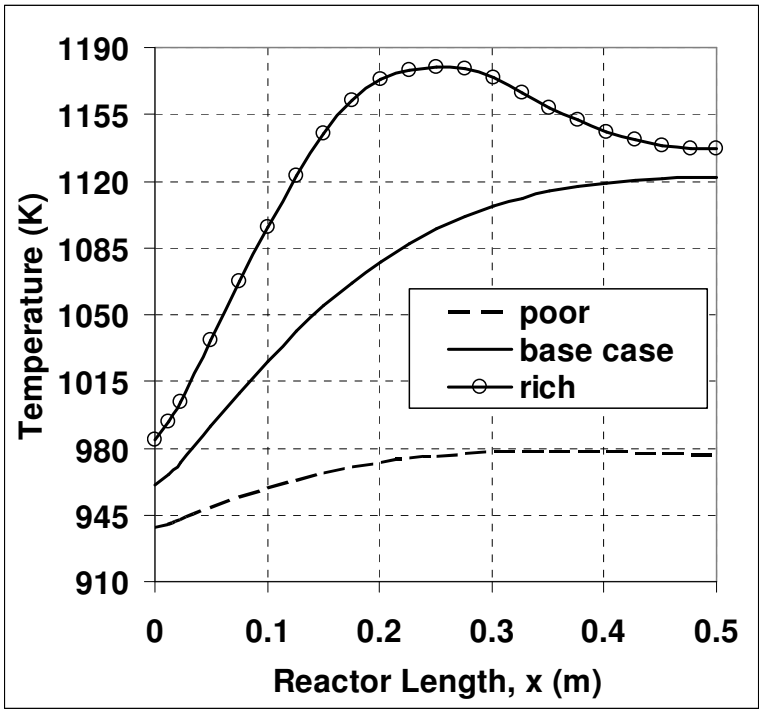

Figure 5.20. Axial temperature profiles of wall centers for base and both oxygen ratio cases

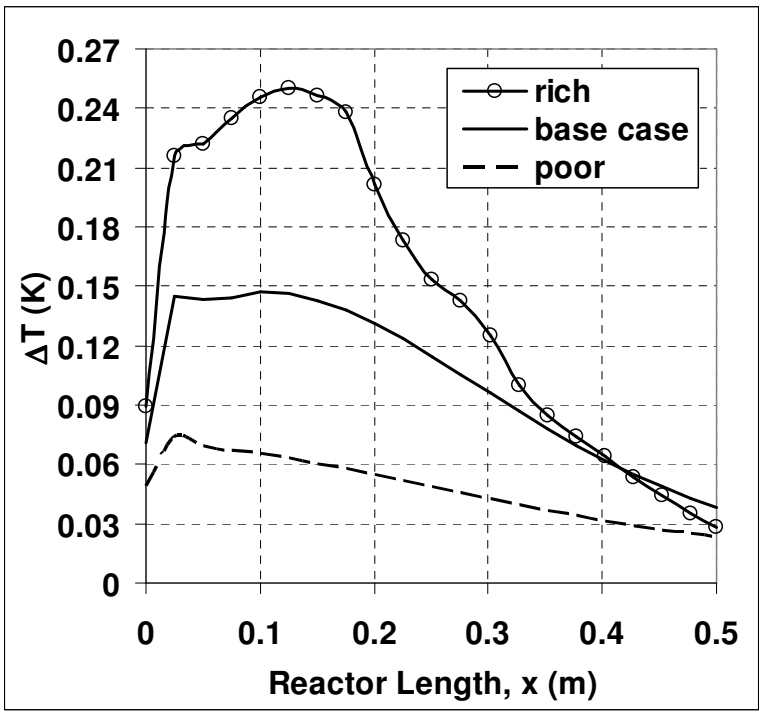

Figure 5.21. Axial temperature difference profiles between combustion and dehydrogenation sides of the wall for base case and both oxygen ratio cases

Figure 5.21 presents the temperature differences between the combustion and dehydrogenation sides of the metal wall. As can be seen from the figure, the greatest difference occurs in the oxygen rich case. This was expected since the heat generation rate is higher; therefore the combustion side of the wall heats up more than the other two cases. The lowest and the smoothest temperature difference profile is observed in the poor case, and the base case following the same trend has a plot between the plots of the oxygen ratio cases. The maximum values of the differences are 0.25 K for rich case, 0.15 K for the base case and 0.07 K for the poor case. Such little values prove the efficiency of a metallic thin wall in conductive heat transfer across the two channels. If compared with the same type of difference of the ethanol steam reforming reaction system, it can be seen that the difference values are higher in the reforming-combustion coupling. This may be because that either the exothermic or the endothermic reaction rate is higher in reforming-combustion coupled system. But since the initial temperatures, the flowrates of the channels, and the heat demand of the two endothermic reactions are different for the two systems, additional work would be required for an accurate reasoning.

From Figure 5.21 it can also be observed that after x = 0.42, the temperature difference of the rich case becomes lower than that of base case, and drops to the same value as the oxygen poor case at the end of the reactor. In the steam reforming-combustion coupled system, it hits down to a value lower than the other two plots because the oxygen-to-methane ratio is four, higher than ethane dehydrogenation system. Axial temperature profiles of wall center and channel centerlines drop down to a minimum at this point and after that remain constant till the exit of the reactor (Figures 5.19 and 5.21). This is probably because that up to this point, the combustion rate has heated up the dehydrogenation channel so much that the temperature difference, i.e. the driving force, between the two has decreased down to levels lower than in steam reforming-total oxidation coupled system.

5.1.5. Comparison of Exit Compositions

The conversion values obtained from the cases studied under catalytic ethane dehydrogenation and methane total oxidation coupling are summarized in Table 5.2. As in the case of ethanol steam reforming combined with methane total oxidation, changes in the

reactor configuration do not affect reactor performance significantly, despite the four-fold increase thickness or the wall ten-fold decrease in thermal conductivity.

Table 5.2. Exit conversions in ethane dehydrogenation-methane total oxidation

Case	Ethane Conversion (%)	Methane Conversion (%)
base case (δ_s = 2 mm) (k_s = 35.5 W/m.K) (oxygen-to-methane = 2)	64	84.5
Thickness Cases		
thin (δ_s = 1 mm)	63.3	84.5
thick (δ_s = 4 mm)	66.2	84.5
Material Cases		
nickel (k_s = 72.25 W/m.K)	66.4	84.7
silica (k_s = 3 W/m.K)	62.5	86.7
Oxygen Ratio Cases		
poor (oxygen-to-methane = 1)	30.8	31.7
rich (oxygen-to-methane = 2.9)	72.5	94.5

The axial concentration profiles at the centerlines of the ethane dehydrogenation and methane oxidation channels for the base case are plotted in Figures 5.22 and 5.23, respectively.

As observed in Table 5.2, the most notable effect in parameter variation is in the oxygen- poor case, where the oxygen-to-methane ratio of 1.0, instead of the stoichiometric ratio of 2.0. The concentration profiles of this case are plotted in Figure 5.24, in order to display the effects of oxygen on ethane depletion more clearly. Ethane conversion declines from 64% to 30% which affects the methane conversion adversely. The methane concentration profiles of the oxygen-poor case are plotted in Figure 5.25.

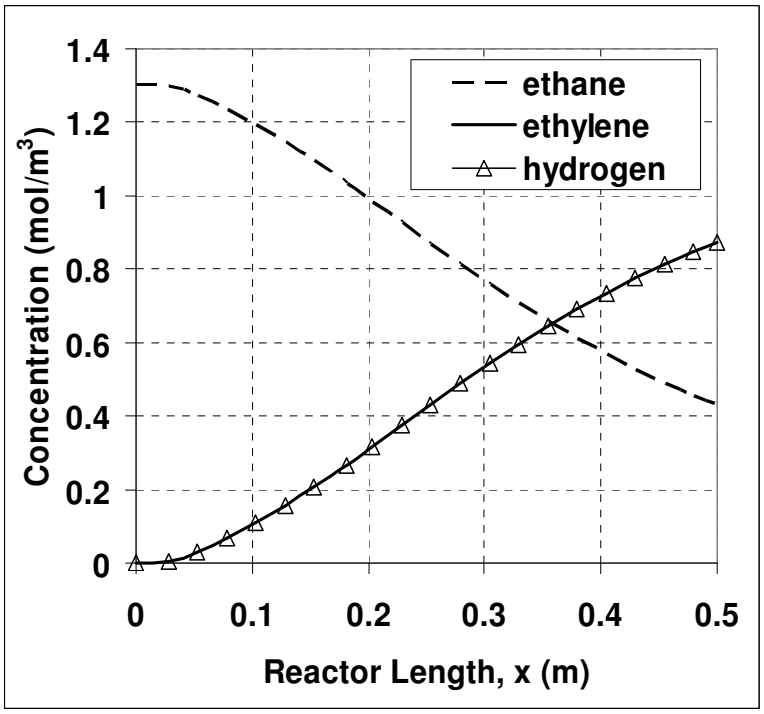

Figure 5.22. Axial concentration profiles for ethane dehydrogenation at the channel centerline in the base case

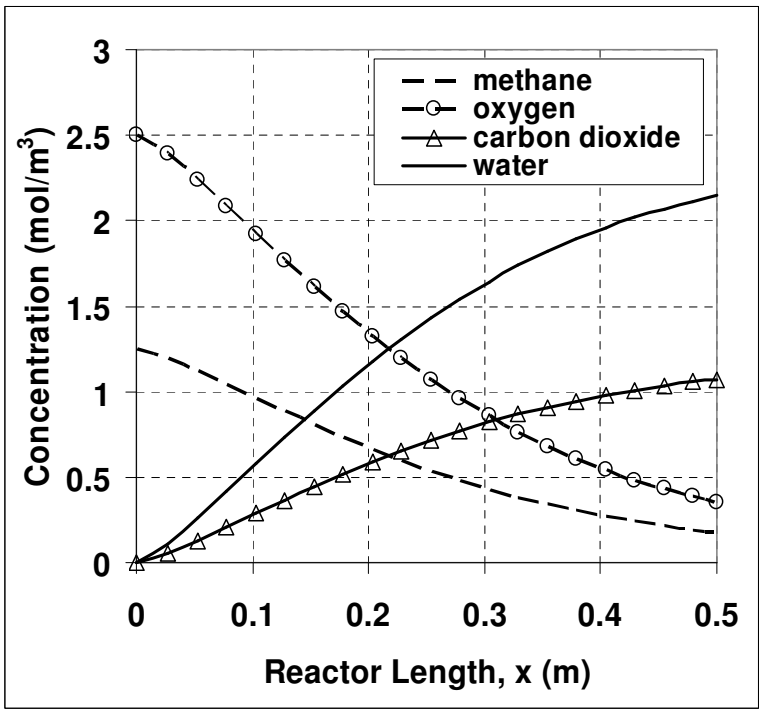

Figure 5.23. Axial concentration profiles for methane oxidation at the channel centerline in the base case

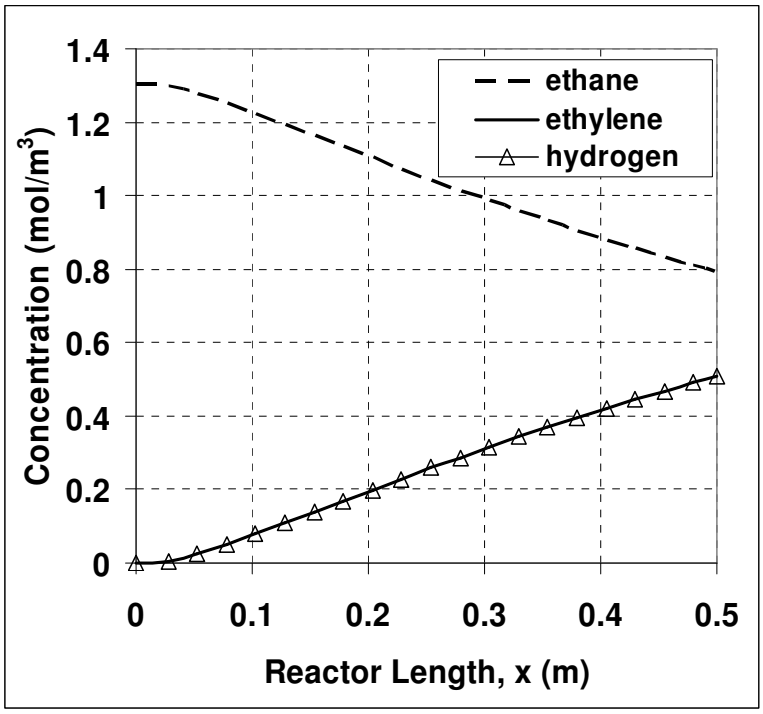

Figure 5.24. Axial concentration profiles for ethane dehydrogenation at the channel centerline of the oxygen-poor case

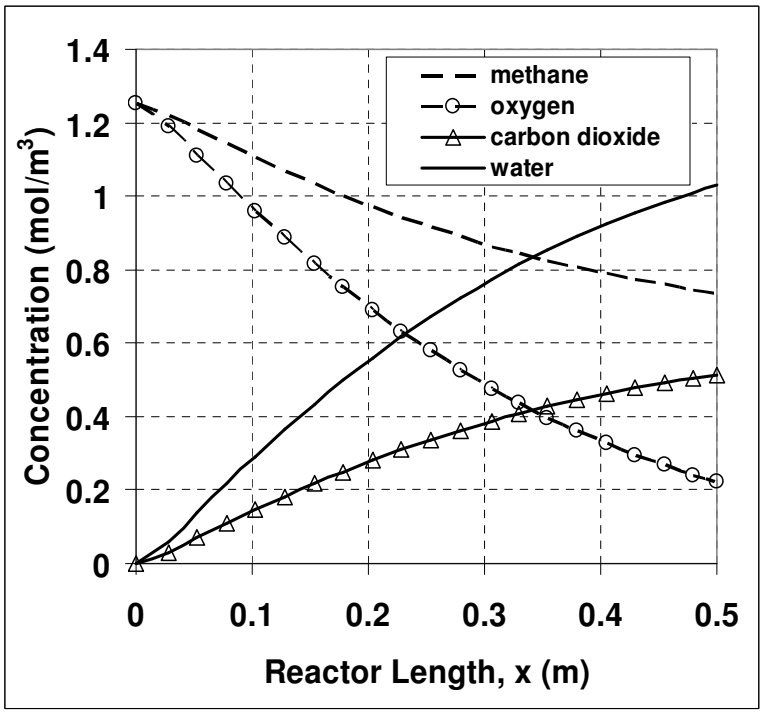

Figure 5.25. Axial concentration profiles for methane total oxidation at the channel centerline of the oxygen-poor case

The methane concentration profiles of the oxygen-poor case plotted in Figure 5.25 and those of the base case in Figure 5.23 are compared in Figure 5.26 where it can be seen that although the initial concentration of methane is almost same in both cases, the base case has higher exit conversions. Figure 5.27 compares the ethanol and hydrogen concentrations between base case and oxygen-poor case.

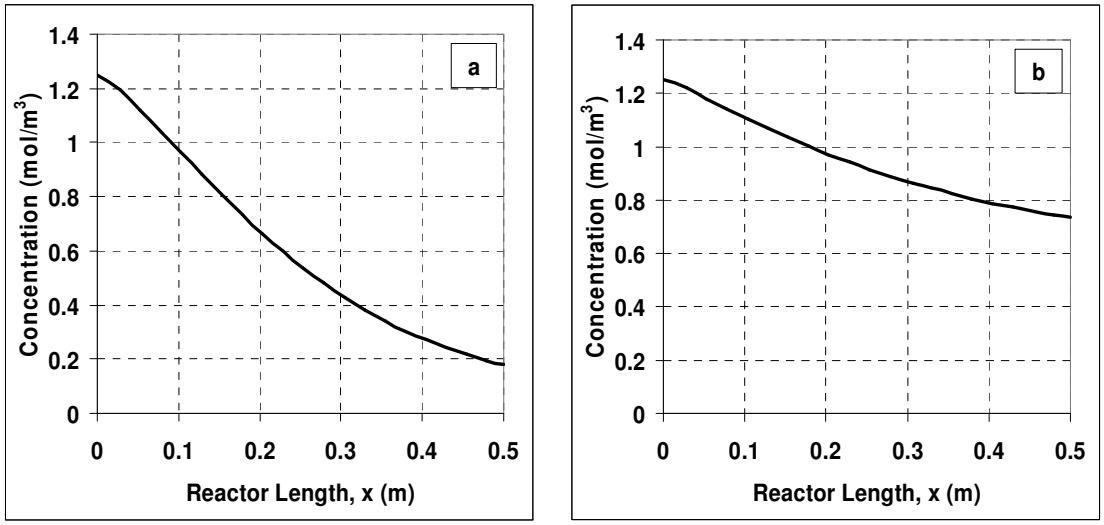

Figure 5.26. Comparison of methane concentrations along the channel centerlines of (a) base case (b) oxygen-poor case

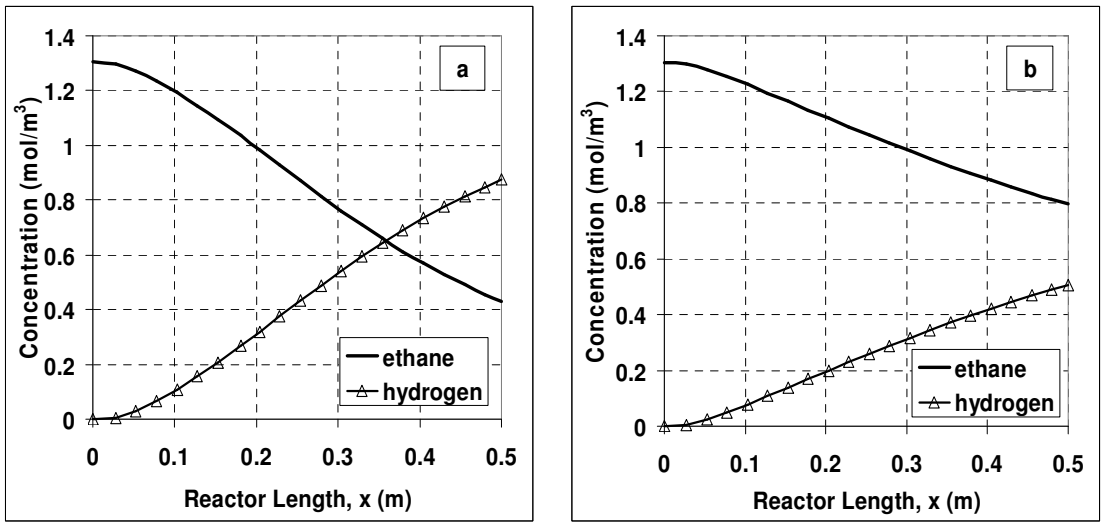

Figure 5.27. Comparison of ethane and hydrogen concentrations along the channel centerlines of (a) base case (b) oxygen-poor case

Methane is consumed less in the oxygen poor case due to the lack of enough oxygen, thus generating less heat. As a result, the rate of the endothermic ethane dehydrogenation reaction is slower than the base case too; consequently a smaller amount of ethane is consumed and less hydrogen is produced, as shown in Figure 5.27. The inlet and outlet compositions of both endothermic dehydrogenation and TOX streams for the base case and the oxygen poor case are recapitulated in Table 5.3.

Table 5.3. Inlet and outlet compositions of dehydrogenation and oxidation streams for the base and oxygen-poor cases

		Base Case		Poor Case	
		in×10^{-4}	out×10^{-4}	in×10^{-4}	out×10^{-4}
Ethane dehydrogenation; Exothermic, channel 1	C2H6	56.820 10.007%	20.181 3.239%	56.820 10.007%	39.330 6.513%
	C2H4	0	45.904 7.368%	0	26.755 4.431%
	H2	0	45.904 7.368%	0	26.755 4.431%
	N2	511 89.993%	511 82.024%	511 89.993%	511 84.625%
Methane total oxidation; Exothermic, channel 2	CH4	13.760 9.604%	2.227 1.484%	13.760 9.588%	93.999 40.404%
	O2	27.520 19.207%	4.454 2.968%	13.760 9.588%	2.775 1.193%
	CO2	0	13.798 9.194%	0	6.625 2.848%
	H2O	0	27.596 18.388%	0	13.249 5.695%
	N2	102 71.189%	102 67.967%	116 80.825%	116 49.861%

Considering the analysis of the two coupled endothermic-exothermic reactions in a CPR, it can be said that the system performance is not sensitive to variations in reactor configuration parameters but operational parameters such as feed composition lead to effects that are useful for analyzing the responses of the system.

4.2. Dynamic Modeling of the CPR

The following figures are the results of the transient solution of the model and display the change of the axial temperature distribution of the channel centerlines and wall center for the ethane dehydrogenation-methane total oxidation coupling system.

The transient simulation of the reactor model was run starting from t = 5 sec and ending in t = 5700 sec, with a step size of 5 seconds. 5700 seconds were enough to reach to steady state, in the final state of the simulation, i.e. at t = 5700, the max temperature is only 2 K lower than that of steady state and is located at the same position. For the sake of clarity in the figures, t = 5700 was not included, because its plot coincides with that of steady state for a great portion of the axis.

Since ethane dehydrogenation is a strongly equilibrium limited reaction, the time required to reach steady-state operation is very long, in addition to the effects of small temperature gradients, which have proven to delay steady-state in ethanol SR simulations studied in section 4.2 of the previous chapter.

It can be said that the results follow a regular trend, both axially and transversely. Because the displayed results are the profiles of the centerlines which lie on three different transverse positions; the combustion channel centerline is on z = 0, the solid wall centerline is on z = 2.1 and dehydrogenation channel centerline is on z = 4.2. The hot spot mentioned in the presentation of dynamic solutions of ethanol steam reforming coupled with methane combustion system is present in here, too.

The temperature profiles of the channel centerlines of the combustion channel and dehydrogenation channel are given in Figures 5.28 and 5.29, respectively. Figure 5.30 displays the change in the centerline temperature profile of the wall with respect to time.

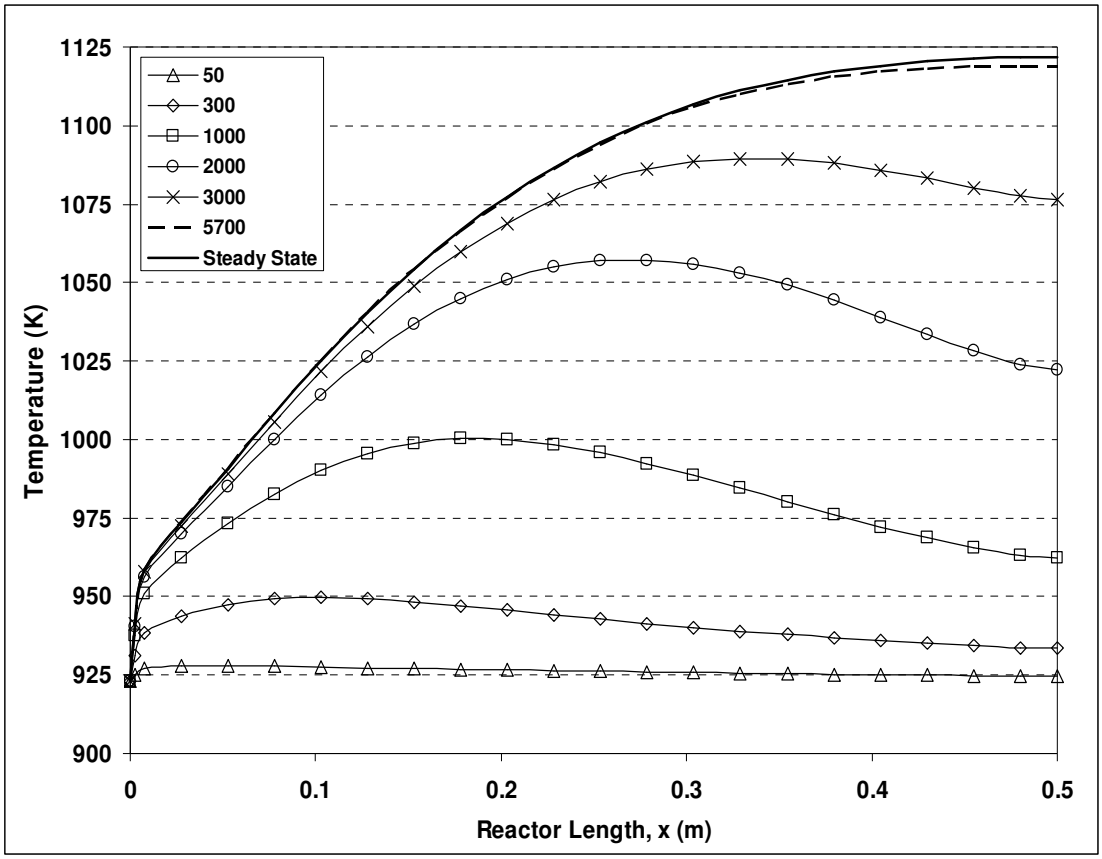

Figure 5.28. Axial temperature distribution of TOX channel centerline at various times

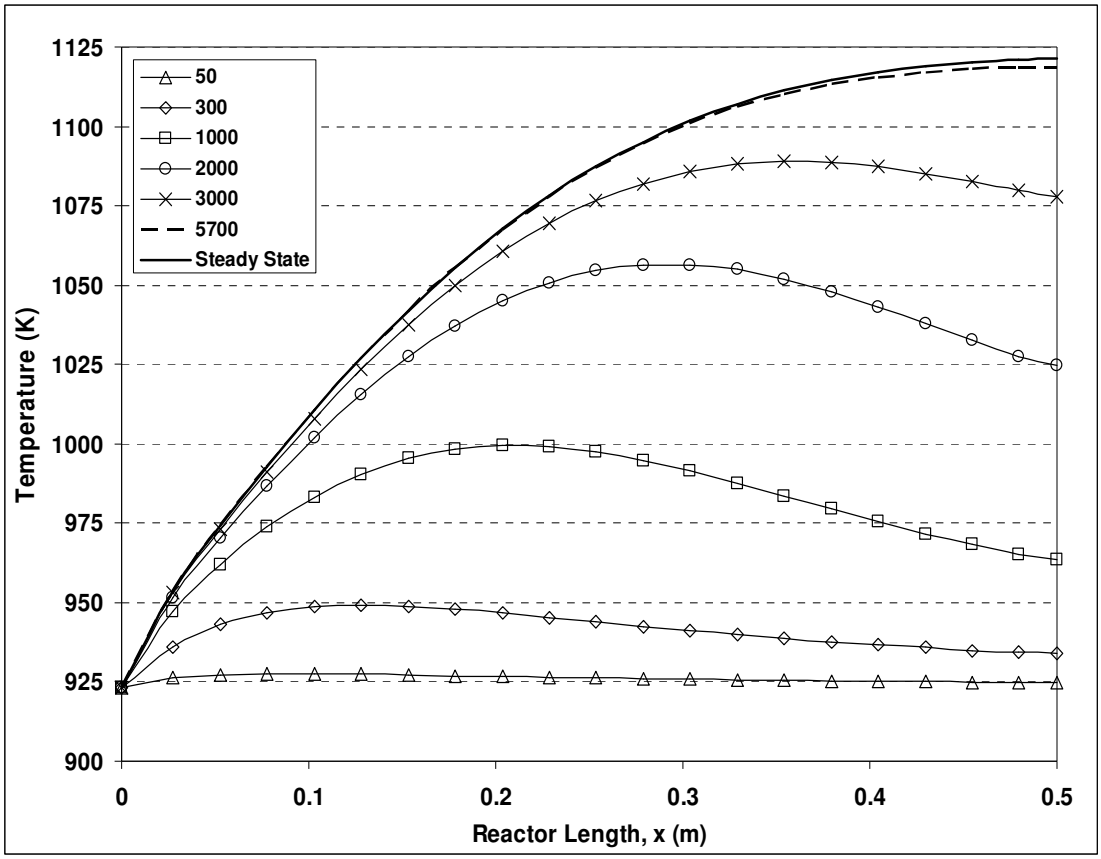

Figure 5.29. Axial temperature distribution of dehydrogenation channel centerline at various times

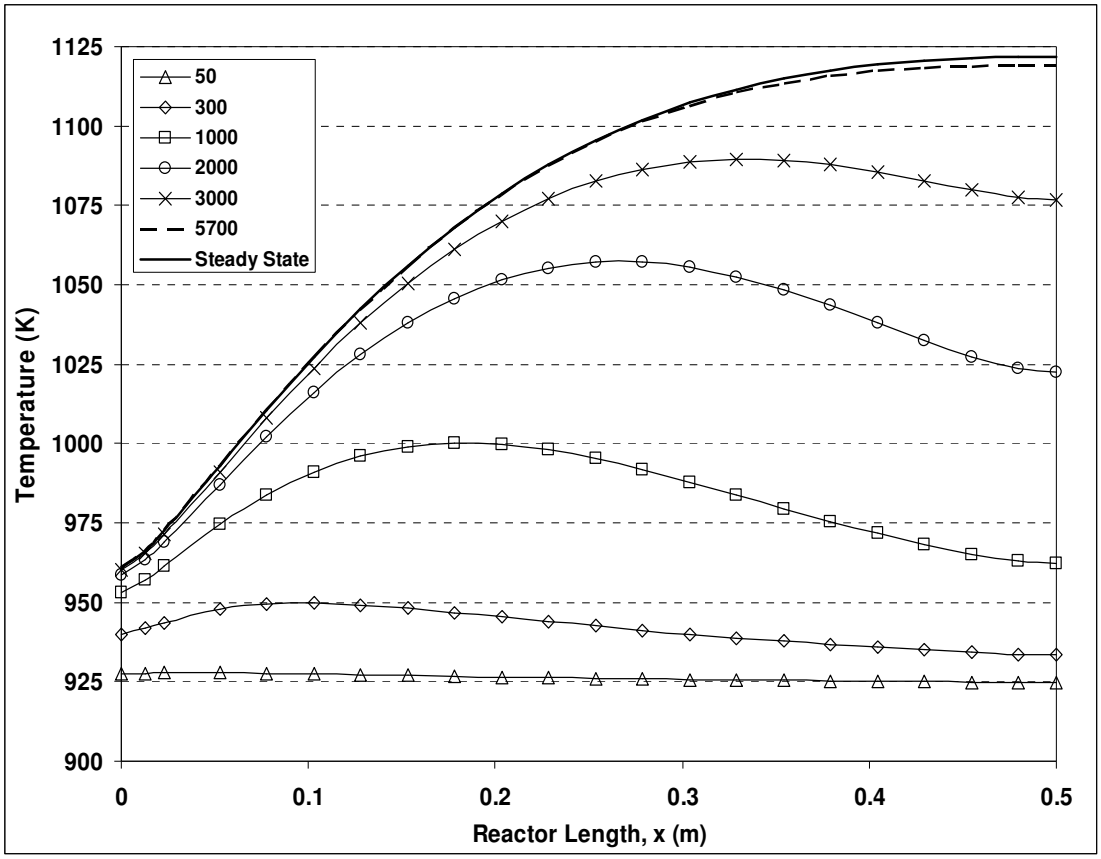

Figure 5.30. Axial temperature distribution of wall center at various times

6. CONCLUSIONS AND RECOMMENDATIONS

6.1. Conclusions

The objective of this study was to develop a mathematical model for simulating the steady and dynamic behavior of a catalytic plate reactor (CPR). After model construction, reactor performance was investigated for two different combinations of endothermic-exothermic reactions as a function of various operational and dimensional parameters such as feed composition on different sides of the plate including steam/hydrocarbon and oxygen/hydrocarbon ratios, plate material and wall thickness. The following major conclusions can be drawn from this study.

Catalytic conversions of ethane and ethanol to hydrogen by dehydrogenation and steam reforming, respectively, coupled with catalytic methane total oxidation, can successfully be described using a two-dimensional heterogeneous CPR model including conservation of momentum, mass and energy.

The base cases constructed for the two endothermic-exothermic reaction pairs using stoichiometric ratios of reactants and standard materials of construction ensure reasonable reactor performance in terms of reactant conversions. For steady state operation, the transverse and axial temperature gradients for both reaction pairs are small, the temperature profiles are smooth, and no hot spot formation is observed.

The metallic wall, due to its high thermal conductivity, makes heat transfer possible between endothermic and exothermic catalyst locations for small temperature differences. Another issue related to the reactor wall is that the effects of axial heat conduction on the temperature profiles have been observed clearly. The heat conducted axially from downstream sections to the entrance section of the reactor through the solid wall causes wall temperatures to be higher than the channel temperatures along the reactor, especially at reactor entrance, where there is almost no heat production.

Analysis of temperature profiles and reactant conversions indicate no significant effect of wall thickness on reactor performance in terms of reactant conversions, but temperature profiles at various locations in the reactor showed increased/decreased resistance to conductive heat transfer through the solid phase with increasing/decreasing wall thickness. Especially the axial temperature profile along the centerline of the exothermic channel displays increasing disturbance at reactor entrance with increasing wall thickness due to the restriction of heat utilization by the endothermic channel.

Changing the wall material as a part of the parametric investigations showed that wall material with lower/higher conductivity does not display the expected thermal patterns similar to those of a thicker/thinner wall with increased/decreased heat transfer resistance. The reason for this behavior is the enhanced/hindered axial heat conduction due to higher/lower thermal conductivity.

In summary, dimensional or structural changes in the reactor do not affect reactor performance in terms of reactant conversions. Although the thermal behaviors change, the gradients are too small to have any detrimental or beneficial effect.

However, variations in the water/hydrocarbon or oxygen/hydrocarbon ratio in any of the two reaction pairs result in notable changes in the reactor output. In ethanol steam reforming, water-deficient feed in the reforming channel reduces ethanol conversion and hydrogen production dramatically. In both ethanol SR and ethane dehydrogenation, reduction in the oxygen content of the TOX channel causes the methane conversion values to be significantly lower, leading to lower heat production/consumption rates, and because of the low residence time and low concentrations of the reactants in the endothermic channel, most of the heat produced is used to heat the gas streams.

As for the dynamic solutions for both reaction pairs, the temporal evolutions of transient solutions converge to steady state and the evolution in spatial direction is consistent with the final steady state solution. Small temperature gradients and equilibrium constraints delay the achievement of steady-sate.

6.2. Recommendations

Various improvements can be implemented in related future works and would be beneficial in order to obtain more realistic results from the simulations.

For example, possible side reactions on the catalysts selected, e.g. water-gas shift reaction in reforming, can be included in the reaction engineering setup of the model.

Several constraints regarding actual catalyst beds, like increasing steam/hydrocarbon ratio to prevent coke formation, can be imposed on reactor operation simulations.

The assumptions made for the physical properties of the chemical species can be replaced with appropriate correlations, for example temperature dependent functions of thermal conductivity and diffusion coefficients of the species can be embedded in the model for the sake of obtaining a more realistic model.

The momentum balance can be solved without the assumption of being independent of compositional and thermal changes.

In addition to the single CPR unit, a reactor configuration consisting of a certain number of basic units stacked up in an orderly fashion can be modeled to simulate and observe the operation and responses of a complete CPR and a system that distributes streams to the channels in this complete system can also be designed and modeled, in order to see its effects on the flow at the channel entrances.

APPENDIX A: PHYSICAL PROPERTIES OF GAS MIXTURES

The density, thermal conductivity, viscosity and heat capacity of nitrogen are used for the corresponding parameters of all gas mixtures. The values used are calculated at the average operating temperature of the systems.

For ethanol steam reforming-methane total oxidation coupled system, the average operating temperature is calculated as;

$$T_{avg} = \frac{T_{min} + T_{max}}{2} = \frac{900\,K + 941\,K}{2} = 920.5\,K \qquad (A.1)$$

For ethane dehydrogenation-methane total oxidation system, average temperature is;

$$T_{avg} = \frac{923K + 1120\,K}{2} = 1021.5\,K \qquad (A.2)$$

The minimum temperatures recorded at the endothermic catalyst layer centers at the entrance section of the reactor were not taken into account since they are very small, local incidents.

Table A.1. Physical properties of N_2 for ethane dehydrogenation and ethanol steam reforming coupled with methane total oxidation

	Ethanol Steam Reforming, @ 920.5 K	Ethane Dehydrogenation, @ 1021.5 K
density, ρ (kg/m^3)	0.366	0.330
heat capacity, C_p (J/kg.K)	1151.36	1170.84
viscosity, η (Pa.s)	3.94×10^{-5}	4.21×10^{-5}
thermal conductivity, k (W/m.K)	0.0615	0.0664

APPENDIX B: CALCULATION OF PHYSICAL PROPERTIES

B.1. Calculation of Density, (ρ)

The densities of the gas mixtures in both channels are assumed to be equal to that of N_2. The values are calculated based on the ideal gas equation of state according to the following formulae;

$$PM = \rho RT \tag{B.1}$$

$$\rho = \frac{PM}{RT} \tag{B.2}$$

$R = 8.314 \left(\frac{\text{m}^3\text{Pa}}{\text{K.mol}} \right)$ is the universal gas constant,

$M = 28 \times 10^{-3}$ (kg/mol), is the molecular weight of N_2, and

$T = T_{\text{avg}}$ (K), is the average operating temperature of the system.

B.2. Calculation of Heat Capacity at constant pressure, (C_p)

Heat capacities of the gas mixtures are taken to be equal to that of N_2. C_{pN_2} is calculated as a function of temperature via Equation B.35 and data in Table B.1 for the average operating temperatures of the reaction systems.

$$C_{pj}[\text{J/K.gr - mol}] = \alpha_j + \beta_j T + \gamma_j T^2 + \delta_j T^3 \tag{B.3}$$

B.3. Calculation of Viscosity, (η)

The viscosity of nitrogen is expressed using the equation;

$$\eta = \eta^0(T) + \eta^r(\tau, \delta) \tag{B.4}$$

where; η (mPa.s) is viscosity,
η^0 is dilute gas viscosity,
η^r is residual fluid viscosity,
$\tau = T_c / T$, and $\delta = \rho / \rho_c$.

The critical parameters T_c and ρ_c are given in Table B.1.

Table B.1. Constants of the heat capacity equation (Sinnot, 2000) and critical parameters (Lemmon and Jacobsen, 2004) for N_2

C_p constants	α_j	β_j ($\times 10^2$)	γ_j ($\times 10^5$)	δ_j ($\times 10^9$)
	31.15	–1.357	2.6796	–11.68
Critical parameters	T_c (K)		ρ_c (mol / dm^3)	
	126.192		11.1839	

The dilute gas contribution is given by;

$$\eta^0(T) = \frac{0.0266958\sqrt{MT}}{\sigma^2 \Omega(T^*)} \tag{B.5}$$

where; σ is the Lennard-Jones size parameter and
Ω is the collision integral given by;

$$\Omega(T^*) = \exp\left(\sum_{i=0}^{4} b_i \left[\ln(T^*)\right]^i \right) \tag{B.6}$$

where; $T^* = T / (\varepsilon/k)$ and
ε/k is the Lennard-Jones energy parameter.

The Lennard-Jones parameters and the coefficients b_i are given in Table B.2.

The residual fluid contribution to the viscosity is given by;

$$\eta^r(\tau,\delta) = \sum_{i=1}^{n} N_i \tau^{ti} \delta^{di} \exp(-\gamma_i \delta^{li}) \tag{B.7}$$

where γ_i is zero when l_i is zero and one when l_i is not zero. The coefficients and exponents of this equation are given in Table B.3.

Table B.2. Coefficients and exponents of dilute gas contribution equation for N_2 (Lemmon and Jacobsen, 2004)

Lennard-Jones parameters	size parameter σ (nm)	energy parameter ε/k (K)
	0.3656	98.94
Coefficients of the Collision Integral Equation	i	b_i
	0	0.431
	1	-0.4623
	2	0.08406
	3	0.005341
	4	-0.00331

Table B.3. Coefficients and exponents of the residual fluid viscosity equation for N_2 (Lemmon and Jacobsen, 2004)

i	N_i	t_i	d_i	l_i
1	10.72	0.1	2	0
2	0.03989	0.25	10	1
3	0.001208	3.2	12	1
4	-7.402	0.9	2	2
5	4.620	0.3	1	3

B.4. Calculation of Thermal Conductivity, (*k*)

Similar to the model for viscosity, the thermal conductivity of N_2 is expressed as a function of temperature and density;

$$k = k^0(T) + k^r(\tau,\delta) + k^c(\tau,\delta) \tag{B.8}$$

where; k (mW/m.K) is thermal conductivity,
k^0 is dilute gas thermal conductivity,
k^r is residual fluid thermal conductivity,
k^c is thermal conductivity critical enhancement,
$\tau = T_c / T$, and $\delta = \rho / \rho_c$.

The critical enhancement contribution, $k^c(\tau, \delta)$, which accounts for fluid properties in the critical region is neglected in the calculations.

The dilute gas contribution is given by;

$$k^0 = N_1\left[\frac{\eta^0(T)}{1\,\mu\text{Pa.s}}\right] + N_2\tau^{t2} + N_3\tau^{t3} \tag{B.9}$$

where η^0 is the dilute gas viscosity described previously. The coefficients and exponents are given in Table B.4.

The residual contribution to the thermal conductivity is;

$$k^r = \sum_{i=4}^{n} N_i \tau^{ti} \delta^{di} \exp(-\gamma_i \delta^{li}) \tag{B.10}$$

where γ_i is zero when l_i is zero and one when l_i is not zero. The coefficients and exponents of this equation are given in Table B.4.

Table B.4. Coefficients and exponents of the residual fluid thermal conductivity equations for N_2, (Lemmon and Jacobsen, 2004)

i	1	2	3	4	5	6	7	8	9
N_i	1.511	2.117	-3.332	8.862	31.11	-73.13	20.03	-0.7096	0.2672
t_i		-1.0	-0.7	0.0	0.03	0.2	0.8	0.6	1.9
d_i				1	2	3	4	8	10
l_i				0	0	1	2	2	2

REFERENCES

Akdim, O., W. J. Cai, V. Fierro, H. Provendier, A. van Veen, W. J. Shen and C. Mirodatos, 2008, "Oxidative steam reforming of ethanol over Ni-Cu/SiO_2, Rh/Al_2O_3, Ir/CeO_2 catalysts: Effect of metal and support on reaction mechanism", *Topics in Catalysis,* Vol. 51, pp. 22-38.

Akpan, E., A. Akande, A. Aboudheir, H. Ibrahim and R. Idem, 2007, "Experimental, kinetic and 2-D reactor modeling for simulation of the production of hydrogen by the catalytic reforming of concentrated crude ethanol (CRCCE) over a Ni-based commercial catalyst in a packed-bed tubular reactor", *Chemical Engineering Science*, Vol. 62, No. 12, pp. 3112-3126, June.

Anxionnaz, Z., M. Cabassud, C. Gourdon and P. Tochon, 2008, "Heat exchanger/reactors (HEX reactors): Concepts, technologies: State-of-the-art", *Chemical Engineering and Processing: Process Intensification*, Vol. 47, No. 12, pp. 2029-2050, November.

Aupretre, F., C. Descorme and D. Duprez, 2002, "Bio-ethanol catalytic steam reforming over supported metal catalysts", *Catalysis Communications,* Vol. 3, pp. 263-267.

Avcı, A. K., D. L. Trimm and M. Karakaya, 2009, In Press; Corrected Proof, "Microreactor catalytic combustion for chemicals processing", *Catalysis Today*, Available online 4 March 2009.

Avcı, A. K., D. L. Trimm and Z. İ. Önsan, 2001, "Heterogeneous reactor modeling for the simulation of catalytic oxidation and steam reforming of methane", *Chemical Engineering Science,* Vol. 56, pp. 641-649.

Barber, M. S., J. Eagleton and E. Hofmann, 2009, "HiGee Technology", *UCSD HiGee Development Team*, http://chemelab.ucsd.edu/higee/technology.html

Barbir, F., 2005, *PEM Fuel Cells: Theory and Practice*, Elsevier.

Barroso, M. N., M. F. Gomez, L. A. Arrua, M. C. Abello, 2006, "Hydrogen production by ethanol reforming over Ni-Zn-Al catalysts", *Applied Catalysis A: General*, Vol. 304, pp. 116–123.

Bayer, T., J. Jenck and M. Matlosz, 2005, "IMPULSE – A New Approach to Process Design", *Chemical Engineering & Technology*, Vol. 28, No. 4, pp. 431-438.

Bird, R. B., W. E. Stewart and E. N. Lightfoot, 2002, *Transport Phenomena*, John Wiley & Sons, New York.

Biswas, P. and D. Kunzru, 2007, "Steam reforming of ethanol on Ni-CeO_2-ZrO_2 catalysts: Effect of doping with copper, cobalt and calcium", *Catalysis Letters*, Vol. 118, pp. 36-49.

Branch, C. A. and D. Tomlinson, 1995, "A stability study of the catalytic plate reactor when reforming an endothermic reaction", *Proceedings of the first international conference on science, engineering and technology of intensive processing*, pp. 31, Nottingham.

Cai, W., B. Zhang, Y. Li, Y. Xu and W. Shen, 2007, "Hydrogen production by oxidative steam reforming of ethanol over an Ir/CeO_2 catalyst", *Catalysis Communications*, Vol.8, pp. 1588–1594.

Cao, C., Y. Wang and R.T. Rozmiarek, 2005, "Heterogeneous reactor model for steam reforming of methane in a microchannel reactor with microstructured catalysts", *Catalysis Today*, Vol. 110, pp. 92.

Charlesworth, R., A. Gough and C. Ramshaw, 1995, "Combustion and steam reforming of methane on thin layer catalysts for use in catalytic plate reactors", *Proceedings of the Fourth UK/National Conference on Heat Transfer*, 26-27 September 1991, C510/099/95, pp. 85-89, Institution of Mechanical Engineers, London.

Comas, J., F. Marino, M. Laborde and N. Amadeo, 2004, "Bio-ethanol reforming on a Ni/Al_2O_3 catalyst", *Chemical Engineering Journal,* Vol. 98, pp. 61-68.

COMSOL AB., 2007, "Understanding the Finite Element Method", in *COMSOL™ Multiphysics v.3.4 Documentation*.

Dautzenberg, F. M. and M. Mukherjee, 2001, "Process intensification using multifunctional reactors", *Chemical Engineering Science*, Vol. 56, No. 2, pp. 251-267, January.

Davis, T., *UMFPACK*, http://www.cise.ufl.edu/research/sparse/umfpack/, 2009

Fierro, V., O. Akdim, H. Provendier and C. Mirodatos, 2005, "Ethanol oxidative steam reforming over Ni-based catalysts", *Journal of Power Sources*, Vol. 145, pp. 659-666.

Freide, J. F., T. Gamlin and M. Ashley, 2003, "The ultimate 'clean' fuel – Gas-to-liquid products", *Hydrocarbon Processing*, Vol. 82, No. 2, pp. 53, February.

Garcia, E.Y. and M.A. Laborde, 1991, "Hydrogen production by the steam reforming of ethanol: Thermodynamic analysis", *International Journal of Hydrogen Energy*, Vol. 16, pp. 307-312.

Gobina, E., K. Hou and R. Hughes, 1995, "Ethane dehydrogenation in a catalytic membrane reactor coupled with a reactive sweep gas", *Chemical Engineering Science,* Vol. 50, pp. 2311-2319.

Gosiewski, K., 2001, "Simulations of non-stationary reactors for the catalytic conversion of methane to synthesis gas", *Chemical Engineering Science*, Vol. 56, pp. 1501-1510.

Grasselli, R. K., D. L. Stern and J. G. Tsikoyiannis, 1999a, " Catalytic dehydrogenation (DH) of light paraffins combined with selective hydrogen combustion (SHC): I. DH → SHC → DH catalysts in series (co-fed process mode)", *Applied Catalysis A: General*, Vol. 189, No. 1, pp. 1-8, November.

Grasselli, R. K., D. L. Stern and J. G. Tsikoyiannis, 1999b, " Catalytic dehydrogenation (DH) of light paraffins combined with selective hydrogen combustion (SHC): I. DH → SHC → DH catalysts in series (co-fed process mode)", *Applied Catalysis A: General*, Vol. 189, No. 1, pp. 9-14, November.

Haryanto, A., S. Fernando, N. Murali and S. Adhikari, 2005, "Current status of hydrogen production techniques by steam reforming of ethanol: A review", *Energy and Fuels***,** Vol. 19, pp. 2098-2106.

Hayes, R. E. and S. T. Kolaczkowski, 1997, *Introduction to catalytic combustion*, Gordon and Breach Science Publisher, Amsterdam.

Henning, D. A. and L. D. Schmidt, 2002, "Oxidative dehydrogenation of ethane at short contact times: species and temperature profiles within and after the catalyst", *Chemical Engineering Science*, Vol. 57, No. 14, pp. 2615-2625, July.

Ismagilov, Z. R., V. V. Pushkarev, O. Y. Podyacheva, N. A. Koryabkina and H. Veringa, 2001, "A catalytic heat-exchanging tubular reactor for combining of high temperature exothermic and endothermic reactions", Chemical Engineering Journal, Vol. 82, No: 1-3 Sp. Iss., pp. 355-360, March.

Karakaya, M. and A. K. Avcı, 2009, "Simulation of On-Board Fuel Conversion in Catalytic Microchannel Reactor-Heat Exchanger Systems", Submitted to: *Topics in Catalysis*, Department of Chemical Engineering, Bogaziçi University. İstanbul.

Kugai, J., V. Subramani, C. S. Song, M. H. Engelhard and Y. H. Chin, 2006, "Effects of nano-crystalline CeO_2 supports on the properties and performance of Ni-Rh bimetallic catalyst for the oxidative steam reforming of ethanol", *Journal of Catalysis*, Vol. 238, pp. 430-440.

Kulkarni, M. S. and M. P. Duduković, 1998, "Periodic operation of asymmetric bidirectional fixed-bed reactors with temperature limitations", *Industrial and Engineering Chemistry Research*, Vol. 37, pp. 770-781.

Kwon, T. H., *Introduction to Finite Element Method-ME583 Course Notes*, http://amp.postech.ac.kr/, 2005

Lattner, J. R. and M. P. Harold, 2007, "Auto-thermal reforming of methanol: Experiments and modeling", *Catalysis Today*, Vol. 120, pp. 78-89.

Lee, A., Y. Tonkovich, S. T. Perry, S. P. Fitzgerald and Y. Wang, 2007, "From seconds to milliseconds to microseconds through tailored microchannel reactor design of a steam methane reformer", *Catalysis Today*, Vol. 120, pp. 21-29, January.

Lemmon, E. W. and R. T. Jacobsen, 2004, "Viscosity and Thermal Conductivity Equations for Nitrogen, Oxygen, Argon, and Air", *International Journal of Thermophysics*, Vol. 25, No. 1, January.

Liguras, D. K., K. Goundani and X. E. Verykios, 2004, "Production of hydrogen for fuel cells by catalytic partial oxidation of ethanol over structured Ni catalysts", *Journal of Power Sources*, Vol. 130, pp. 30-37.

Lopez, E., E. Heracleous, A. A. Lemonidou and D. O. Borio, 2008, "Study of a multi-tubular reactor for ethylene production via ethane oxidative dehydrogenation", *Chemical Engineering Journal,* Vol. 145, pp. 308-315.

Ma, L. and D. L. Trimm, 1996a, "Alternative catalyst bed configurations for the autothermic conversion of methane to hydrogen", *Applied Catalysis A: General*, Vol. 138, No. 2, pp. 265-273, May.

Ma, L., D. L. Trimm and C. Jiang, 1996, "The design and testing of an autothermal reactor for the conversion of light hydrocarbons to hydrogen 1. The kinetics of the catalytic oxidation of light hydrocarbons", *Applied Catalysis A: General*, Vol. 138, pp. 275.

Mas, V., R. Kiproes, N. Amadeo and M. Laborde, 2006, "Thermodynamic analysis of ethanol/water system with the stoichiometric method", *International Journal of Hydrogen Energy*, Vol. 31, pp. 21-28.

NAVFAC (Naval Facilities Engineering Command), *Environmental Restoration and Base Realignment and Closure Program-Remediation (Clean-up) Technologies*, https:// portal. navfac.navy.mil/portal/page/portal/navfac/navfac_ww_pp/navfac_nfesc_pp/environmental/ erb/imageserb

Nilsson, J. and F. Sveider, 2000, "Characterizing Mixing in a HEX Reactor Using a Model Chemical Reaction", *Department of Chemical Engineering II*, Lund, Sweden, http://www.chemeng.lth.se/exjobb/002.pdf

O'Hayre, R., S-W. Cha, W. Colella and F. B. Prinz, 2005, *Fuel Cell Fundamentals*, Wiley.

Önsan, Z. İ., 2007, "Catalytic processes for clean hydrogen production from hydrocarbons", *Turkish Journal of Chemistry*, Vol. 31, pp. 531-550.

Örücü, E., F. Gökaliler, A. E. Aksoylu and Z. İ. Önsan, 2008, "Ethanol steam reforming for hydrogen production over bimetallic Pt-Ni/δ-Al_2O_3", *Catalysis Letters*, Vol. 120, pp. 198-203.

Paglianti, A., 2008, "Recent Innovations in Turbulent Mixing with Static Elements", *Recent Patents on Chemical Engineering*, Vol. 1, pp. 80-87.

Qi, A., B. Peppley and K. Karan, 2007, "Integrated fuel processors for fuel cell application: A review", *Fuel Processing Technol*ogy, Vol. 88, pp. 3-22.

Qi, A., S. Wang, G. Fu and D. Wu, 2006, "Integrated fuel processor built on auto-thermal reforming of gasoline: A proof-of-principle study" *Journal of Power Sources***,** Vol. 162, pp.1254-1264.

Ramaswamy, R. C., P. A. Ramachandran and M. P. Dudukovic, 2006, "Recuperative coupling of exothermic and endothermic reactions", *Chemical Engineering Science*, Vol. 61, pp. 459-472.

Reay, D. A., 1993, "Catalytic combustion: Current status and implications for energy efficiency in the process industries", *Heat Recovery Systems and CHP*, Vol. 13, No. 5, pp. 383–390.

Sahoo, D. R., S. Vajpai, S. Patel and K. K. Pant, 2007, "Kinetic modeling of steam reforming of ethanol for the production of hydrogen over Co/Al_2O_3 catalyst", *Chemical Engineering Journal,* Vol. 125, pp. 139-147.

Salge, J.R., G.A. Deluga and L.D. Schmidt, 2005, "Catalytic partial oxidation of ethanol over noble metal catalysts", *Journal of Catalysis*, Vol. 235, pp. 69–78.

Schenk, O., *Introduction into PARDISO*, http://www.pardisoproject.org/index.html, 2007

Semelsberger, T. A., L. F. Brown, R. L. Borup and M. A. Inbody, 2004, "Equilibrium products from autothermal processes for generating hydrogen-rich fuel-cell feeds", *International Journal of Hydrogen Energy*, Vol. 29, pp. 1047–1064.

Shen, Z., J. Liu, H. Xu, Y. Yue, W. Hua and W. Shen, 2009, "Dehydrogenation of ethane to ethylene over a highly efficient Ga_2O_3/HZSM-5 catalyst in the presence of CO_2" *Applied Catalysis A: General*, Vol. 356, pp. 148-153.

Siirola, J.J., 1996, "Industrial applications of chemical process synthesis", *Advances in Chemical Engineering,* Vol. 23, pp. 1-62.

Sinnot, R. K., 2000, *Coulson & Richardson's Chemical Engineering Vol. 6*, Butterwoth-Heinemann, Boston.

Soyal-Baltacıoğlu, F., A. E. Aksoylu and Z. İ. Önsan, 2008, "Steam reforming of ethanol over Pt-Ni catalysts", *Catalysis Today*, Vol. 138, pp. 183-186.

Sulzer Chemtech, 2009, *Sulzer Compax™ product brochure*, http://www.sulzerchemtech. com/ en/DesktopDefault.aspx/tabid-571/

Sun, J., X-P. Qiu, F. Wu and W-T. Zhu, 2005, "Hydrogen from steam reforming of ethanol at low temperature over Ni/Y_2O_3, Ni/La_2O_3 and Ni/Al_2O_3 catalysts for fuel cell application", *International Journal of Hydrogen Energy*, Vol. 30, pp. 437-445.

Sutherland, W. S., 1874, Patent No. UK206642

Tan, Ö., E. Maşalacı, Z. İ. Önsan and A. K. Avcı, 2008, "Design of a methane processing system producing high purity hydrogen", *International Journal of Hydrogen Energy*, Vol. 33, pp. 5516-5526.

Thakur, R. K., Ch. Vial, K. D. P. Nigam, E. B. Nauman and G. Djelveh, 2003, "Static Mixers in the Process Industries – A Review", *Chemical Engineering Research and Design*, Vol. 81, No. 7, pp. 787-826, August.

Tian, Y. and M. O. Tadé, 2000, "Inference on Conversion and Purity for ETBE Reactive Distillation", Brazilian Journal of Chemical Engineering, Vol. 17, pp. 4-7, December.

Trimm, D. L. and Z. İ. Önsan, 2001, "On board fuel conversion for hydrogen fuel cell driven vehicles", *Catalysis Reviews-Science and Engineering***,** Vol. 43, pp. 31-84.

Tsouris, C. and J. V. Porcelli, 2003, "Process intensification - has its time finally come?", *Chemical Engineering Progress*, Vol. 99, No. 10, pp. 50.

Vaidya, P. D. and A. E. Rodrigues, 2006a, "Insight into steam reforming of ethanol to produce hydrogen for fuel cells", *Chemical Engineering Journal,* Vol. 117, pp. 39-49.

Vaidya, P. D. and A. E. Rodrigues, 2006b, "Kinetics of steam reforming of ethanol over a Ru/Al_2O_3 catalyst", *Industrial and Engineering Chemistry Research*, Vol. 45, pp. 6614-6618.

van Goethem, M. W. M., S. Barendregt, J. Grievink, J. A. Moulijn and P. J. T. Verheijen, 2007, "Ideal chemical conversion concept for the industrial production of ethane from hydrocarbons", *Industrial and Engineering Chemistry Research*, Vol. 46, pp. 4045-4062.

van Sint Annaland, M. and R. C. Nijssen, 2002, "A novel reverse flow reactor coupling endothermic and exothermic reactions: an experimental study", *Chemical Engineering Science*, *Volume*, Vol. 57, No. 22-23, pp. 4967-4985, November-December.

Vincent, R. S., R. P. Linstedt, N. A. Malik, I. A. B. Reid and B. E. Messenger, 2008, "The chemistry of ethane dehydrogenation over supported platinum catalyst", *Journal of Catalysis*, 260, pp. 37-64.

Virnovskaia, A., E. Rytter and U. Olsbye, 2008, "Kinetic and isotopic study of ethane dehydrogenation over a semicommercial Pt-Sn/Mg(Al)O catalyst" *Industrial and Engineering Chemistry Research*, Vol. 47, pp. 7167-7177.

Zalc, J. M. and D. G. Löffler, 2002, "Fuel processing for PEM fuel cells: transport and kinetic issues of system design" *Journal of Power Sources***,** Vol. 111, pp. 58-64.

Zanfir, M. and A. Gavriilidis, 2001, "Modeling of a catalytic plate reactor for dehydrogenation-combustion coupling", *Chemical Engineering Science*, Vol. 56, No. 7, pp. 2671-2683, April.

Zanfir, M. and A. Gavriilidis, 2002a, "An investigation of catalytic plate reactors by means of parametric sensitivity analysis", *Chemical Engineering Science*, Vol. 57, pp. 1653-1659.

Zanfir, M. and A. Gavriilidis, 2002b, "Parametric sensitivity in catalytic plate reactors with first-order endothermic-exothermic reactions", *Chemical Engineering Journal*, Vol. 86, pp. 277-286.

Zanfir, M. and A. Gavriilidis, 2003, "Catalytic combustion assisted methane steam reforming in a catalytic plate reactor", *Chemical Engineering Science*, Vol. 58, pp. 3947-3960.

Zanfir, M. and A. Gavriilidis, 2004, "Influence of flow arrangement in catalytic plate reactors for methane steam reforming", *Chemical Engineering Research and Design*, Vol. 82, No. A2, pp. 252-258, February.